Visual Adaptations to Natural Statistics

by

Divyansh Gupta

November, 2024

A thesis submitted to the
Graduate School
of the
Institute of Science and Technology Austria
in partial fulfillment of the requirements
for the degree of
Doctor of Philosophy

Committee in charge:

Jack Bravo, Chair Maximilian Jösch Gašper Tkačik Tom Baden



The thesis of Div	yansh Gupta, titled \	Visual Adaptations	s to Natural Stat	tistics, is approved by:
Supervisor: Ma	ximilian Jösch, ISTA,	Klosterneuburg,	Austria	
	Signature:			
	Signature:			
Committee Me	e mber : Gašper Tkači	ik, ISTA, Klostern	euburg, Austria	
	Signature:			
Committee Me	ember: Tom Baden,	University of Suss	ex, Brighton, UI	<
		·	-	
	Signature:			
Defense Chair:	Jack Bravo, ISTA, k	(losterneuburg, A	ustria	
	•			
	Signature:			

© by Divyansh Gupta, November, 2024

CC BY-NC-SA 4.0 The copyright of this thesis rests with the author. Unless otherwise indicated, its contents are licensed under a Creative Commons Attribution-NonCommercial-ShareAlike 4.0 International License. Under this license, you may copy and redistribute the material in any medium or format. You may also create and distribute modified versions of the work. This is on the condition that: you credit the author, do not use it for commercial purposes and share any derivative works under the same license.

ISTA Thesis, ISSN: 2663-337X

ISBN: 978-3-99078-050-3

I hereby declare that this thesis is my own work and that it does not contain other people's work without this being so stated; this thesis does not contain my previous work without this being stated, and the bibliography contains all the literature that I used in writing the dissertation.

I declare that this is a true copy of my thesis, including any final revisions, as approved by my thesis committee, and that this thesis has not been submitted for a higher degree to any other university or institution.

I certify that any republication of materials presented in this thesis has been approved by the relevant publishers and co-authors.

Signature: _____

Divyansh Gupta November, 2024

Abstract

Biological vision is unlike a camera; rather than transmitting light information faithfully, early visual circuits process the visual scene to convey only the relevant information in an efficient manner. Consequentially, the nature of this visual processing then depends on what is the relevant information in a scene and on the notion of efficiency. In this work, I study how visual processing is modulated by two different variations in the visual scene. First, I discovered that in the mouse (Mus musculus) retina, Retinal Ganglion Cells in the upper and lower visual field have differences in the center surround structure of their receptive fields. Comparison with models of efficient coding show that this adaptation likely evolved to cope with the brightness gradient from the sky to the ground that is pervasive in natural scenes. In the second project, I study how the downstream neurons in the Superior Colliculus dynamically change their temporal selectivity depending on the ambient luminance and behavioral state. As the scene gets darker or when the animal is is less aroused, the neuronal responses get laggier, while still maintaining their relative timing with respect to the population. Overall, this work emphasises the need to understand visual processing in the context of specific demands of the animal in its the environment. The adaptive changes in the visual system, from the retinal ganglion cells to the superior colliculus, highlight the intricate ways in which biological vision optimizes the processing of visual information.

Acknowledgements

It took a lot of mental gymnastics to push through the tough phases of this PhD, to reassure myself that I was worthy of being in a place filled with such brilliant people, and for not being afraid to ask for help.

That help almost always came from the members of the Jösch lab, past and present, who were always generous with their time and patience. Max has earned my deepest gratitude and respect, for taking me under his wing, for his excellent mentorship and for pushing me to strive for excellence. Over these years, I learnt immensely from Wiktor, Tomas, Anton, and Olga who taught me the many ways of being a Neuroscientist. I spent unforgettable moments discussing science and/or life with my fellow comrades, Roshan, Laura, Florian, Vika, Ece, Eleonora, Tomás, Dafna, Anuj and Rimma, for which I will be forever grateful.

I would also like to thank Gašper Tkačik and Tom Baden for their advise and encouragement throughout this journey.

This work would have been impossible without the Scientific Service Units of IST Austria. The resources and expertise provided by Scientific Computing (especially Alois Schlögl), the MIBA Machine Shop (especially Todor Asenov), the Preclinical Facility (especially Freyja Langer), the Library, the Lab Support Facility and the Imaging and Optics Facility were the essential bedrock I could build upon. I would also like to thank IT support at ISTA for powering through remote work and a cyberattack.

I am grateful for having been funded initially by the European Union Horizon 2020 Marie Skłodowska-Curie grant 665385 and later by Prof. Maximilian Joesch's the European Research Council Starting (756502) and Consolidator (101086580) Grants.

Lastly, the most important thanks goes to my friends and family for their understanding and support. The countless meals and conversations shared with Suyash, Gergely and Sarath always lifted my heart. But most of all, I want to express my deepest gratitude to my parents, my brother Akash, and my Love, Apeksha. Your unwavering love and belief in me have always been my driving force. I can never thank you enough.

About the Author

Divyansh Gupta completed his BTech and MTech in Computer Science and Engineering at the Indian Institute of Technology (IIT) Kharagpur. He joined ISTA in 2018 with the aim of studying how neuroscience and computer science can help each other in studying 'Intelligence'. He joined the lab of Prof. Maximilian Jösch, where he studies the visual system of mice and how it has adapted to encode the natural environment. He developed a method for recording high throughput neuronal signals from the retina and used it to study how the eye encodes information for the brain. He then proceeded to study how the brain itself adapts to the changing visual world. During his studies, he published his findings in Nature Neuroscience in 2023, and presented his work at the Retinal Circuits Symposium, the Austrian Neuroscience Association meeting, the International Winter Neuroscience Conference, Systems Vision Science Symposium, and the Federation of European Neuroscience Societies Forum.

List of Collaborators and Publications

Chapter 2

Gupta, D., Młynarski, W., Sumser, A., Symonova, O., Svatoň, J., & Joesch, M. (2023). Panoramic visual statistics shape retina-wide organization of receptive fields [Number: 4 Publisher: Nature Publishing Group]. *Nature Neuroscience*, *26*(4), 606–614. https://doi.org/10.1038/s41593-023-01280-0

Chapter 3

Divyansh Gupta and Maximilian Joesch

Appendix A

Divyansh Gupta, Yoav Ben-Simon and Maximilian Joesch

List of Figures

1.1	Anatomy of the vertebrate retina	3
1.2	Diagram showing how the STA is calculated	6
2.1	Predictive coding and natural scene statistics	14
2.2	Large-scale retinal receptive field mapping	15
2.3	Retina-wide receptive field architecture	16
2.4	Global adaptation across retinal pathways	17
2.5	Colliculus-wide retinal ganglion cell's receptive field architecture	18
2.6	Predictive coding predictions derived from a previously proposed model	28
2.7	Predictive coding model trained with an alternative set of natural images	29
2.8	Clustering of Ca 2+ signals to "chirp" stimulus shows segregation into functional	
	types	30
2.9	Comparison and parametrizations of RFs	31
2.10	Spatial structure of average RFs across the retina and superior colliculus	32
2.11	Homogeneity of receptive field architecture in the temporal-nasal axis	33
2.12	Surround strength center size and asymmetric streak align in retinas without an	
	S-opsin staining	34
2.13	Proportions of cluster membership	35

2.14 Sampling RGC bouton receptive field architecture across superior colliculus	36				
 3.1 Population spike timing changes with luminance 3.2 Shifts in temporal RFs across luminance 3.3 Changes in RF dynamics with behavioral state 	43 45 46				
A.1 RGCs projecting to vLGN and widefield nuerons in SC	72				
List of Table	es				
2.2 RF properties across retinal halves for different functional types	40				
List of Abbreviation CNN Convolutional Neural Networks. 7	15				
LGN Lateral Geniculate Nucleus. 2, 48					
LN Linear Non-linear (model). 6					
MEA Mulit-Electrode Array. 9					
MID Maximally Informative Dimensions. 7					
OTZ Opsin Transition Zone. 3					
RF Receptive Field. 5					
RGC Retinal Ganglion Cell. 4, 53					
SC Superior Colliculus. 1, 2, 53					
SNR Signal to Noise Ratio. 8, 41, 47					
STA Spike Triggered Average. 6					

Table of Contents

ostrac	t		vii
know	ledgen	nents	viii
oout 1	the Au	thor	ix
st of	Collabo	orators and Publications	x
st of	Figures		x
st of	Tables		xi
st of	Abbrev	riations	xi
ble o	f Cont	ents	xii
			1
1.1	The M	ouse Visual System	2
	1.1.1	The Retina	2
		Anatomy of the Retina	2
		•	5
1.2			5
		•	5
	1.2.2	·	7
		•	7 8
		·	8
	1.2.3	Methods of Population Neurophysiology	9
Reti	nal ada	aptations to visual statistics across elevation	11
2.1	Abstra	ct and Introduction	13
2.2			14
			14
		•	15
		·	17
		·	17
0.0			19
			19
2.4			20
	cknown count to st of st	cknowledgen cout the Aur st of Collabo st of Figures st of Abbrev able of Cont Introduction 1.1 The M 1.1.1 1.1.2 1.2 Studyin 1.2.1 1.2.2 1.2.3 Retinal ada 2.1 Abstra 2.2 Results 2.2.1 2.2.2 2.2.3 2.2.4 2.2.5 2.3 Discus 2.4 Referen	Introduction 1.1 The Mouse Visual System 1.1.1 The Retina Anatomy of the Retina 1.1.2 The Superior Colliculus 1.2 Studying the Visual System 1.2.1 Models of Receptive Fields 1.2.2 Constraints and Adaptations: Normative Perspectives Efficient Coding Sparse Coding Predictive Coding 1.2.3 Methods of Population Neurophysiology Retinal adaptations to visual statistics across elevation 2.1 Abstract and Introduction 2.2 Results 2.2.1 Efficient coding predicts receptive field shapes across the visual field 2.2.2 Large-scale characterization of receptive fields across the retina 2.2.3 Receptive fields are adapted to anisotropic natural scene statistics 2.2.4 Adaptations to natural scene statistics across retinal pathways 2.2.5 In vivo panoramic receptive field anisotropies match predictions 2.4 References

	2.6	Supple	mentary Information	2
3	Coll		daptations to internal and external context	4
	3.1	Introdu	uction	4
	3.2	Results	5	4
			Population spike timing changes with luminance	4
			Temporal RFs shift with mean luminance	4
			Pupil size modulates RF dynamics	4
	3.3	Discus	sion	4
			Comparison to Efficient Coding	4
			Relative timing code	4
			Behavioral modulation of visual processing	4
			Limitations of this study	4
	3.4	Metho	ds	4
		3.4.1	Animal Management	4
		3.4.2	Surgical Preparation	4
		3.4.3	Behavioral Tracking	4
		3.4.4	Stimulus	5
		3.4.5	Electrophysiology	5
		3.4.6	Receptive Field Analysis	5
		3.4.7	RF Parametrization	5
		3.4.8	Spike Rasters	5
	3.5	Data A	Availability	5
	3.6		Availability	5
4	Disc	cussion		5
_	Disc	Lussion	The need for more	5 .
			Mechanisms of receptive field adaptations across retinal space	5
			Theoretical perspectives	5
			Ethological relevance of observed adaptations	5
			Concluding Remarks	5
			Concluding Nemarks	5
Bi	bliog	raphy		5
۸	Fun	ctional	imaging of RGCs projecting to genetically defined targets	7

CHAPTER 1

Introduction

Adaptation is a ubiquitous phenomenon that allows sensory systems to adjust their processing of incoming information based on changes in input statistics. The natural world is rich with both regularities and variations. Animals, including humans, need to adapt their physiology and behavior in order to best respond to such rich statistical information in the environment. Some examples of this phenomenon can be found in our daily life; think about how we are able to hear and understand speech in a loud action movie or a quiet whisper. Or when we are overcome by a certain smell while entering a room, but don't even notice it after a few minutes. Humans can even extend their sensory adaptations externally, for instance by tinting sunglasses to be darker at the top than the bottom, to account for the fact that the bright Sun only shines from above.

Why must sensory systems adapt to the incoming stimuli? For the simple reason that they should transmit as much relevant information about the input as possible (Atick, 2011; Barlow, 1961), but they only have limited resources to do so, a theoretical framework known as 'Efficient Coding' (Laughlin, 1981). For instance, a sensory neuron may be constrained by metabolic demands, the dynamic range of its outputs, or inherent biological noise. Natural inputs, on the other hand, can have vast dynamical range, or vary across extremely fast or slow timescales. Adaptation allows the system to continue to be parsimonious with resource use, even as changes in input statistics demand an update to the coding strategy.

While adaptation is prevalent in all sensory systems, the visual system is one of the better understood sensory modalities for the main reason that it is far easier to reproduce most kinds of visual stimuli in the lab, than it is to reproduce all the different odorants or touch sensations, etc. The mechanisms and principles learnt from studying visual adaptation have also been found in other modalities and will likely continue to inform sensory neuroscience in the future.

In this thesis, I investigate how the peripheral visual system in mice modulates the spatial or temporal representations of visual stimuli as a response to the different statistics of natural scenes. More specifically, in Chapter 2, I uncover how different locations of the retina have evolved different spatial processing strategies to compensate for the large luminance range between the sky and the ground. In Chapter 3, I investigate how a prominent retino-recipient part of the brain, the Superior Colliculus, dynamically adjusts the temporal dynamics of the neural code when the amount of light changes, like at different times of the day, or when the animal's pupil dilates.

To guide the reader, I will first introduce the parts of the mouse visual system relevant for this purpose. I will then discuss the recording technologies and computational theories that actually allow us to probe these questions.

1.1 The Mouse Visual System

The visual system is responsible for capturing, processing and interpreting information about the visual environment. The process begins in the eye, which is connected via the optic nerve to the image forming and non-image-forming pathways of the brain. The non-image forming functions of the visual system include circadian entrainment, optokinetic reflex and pupillary light reflex which are typically controlled by dedicated nucleii in the brain (Seabrook et al., 2017).

The hallmark of the image forming pathway is retinotopy: the phenomenon where nearby points in visual space are represented by nearby neurons in anatomical space. From the retina, one image-forming pathway leads to the Primary Visual Cortex (V1) via the Lateral Geniculate Nucleus (LGN) and the other heads to the Optic Tectum, also known as the Superior Colliculus (SC). The geniculocortical pathway is evolutionarily newer and highly developed only in mammals, while the tectal pathway evolved with the first vertebrates—jawless fishes. The relative importance and sophistication of the thalamic and tectal pathways varies across different vertebrate species (Isa et al., 2021).

1.1.1 The Retina

The vertebrate retina is a complex and highly species-specialized structure that serves as the starting point of the visual system. Not only is it responsible for transducing light into neural signals, but a sophisticated 3-layer network of neurons also shapes the signal to extract spectral-spatio-temporal features that are conveyed to the brain via the optic nerve.

Anatomy of the Retina

The retina is a layered neural tissue, approximately 100-300m in thickness, located at the back of the eye. From outside going inwards, these layers are the Outer Nuclear layer, Outer Plexiform Layer, Inner Nuclear Layer, Inner Plexiform Layer, and the Ganglion Cell Layers (Fig. 1.1. These layers house more than 100 different cell types (Masland, 2012; Yan et al., 2020), divided into the following major classes:

■ **Photoreceptors** are input neurons containing receptors called opsins, that convert photons into electrochemcial signals through a cascade of biochemical reactions (Fu, n.d.). Most mammalian retinas have two to three types of cone photoreceptors and one type of rod photoreceptor. Rods are highly sensitive to low light levels and are crucial for night vision, while cones carry more color information and function at brighter light levels. While some primates, including humans, evolved to have a third, red-sensitive (~560nm), L opsin, most mammalian cones possess one of two types of opsins, S or M opsin, which have their peak sensitivity in the UV-blue (~400nm) and green (~520nm) portions of the visual spectrum, respectively.

In the mouse retina, the distribution of these two cone opsins is non-uniform, with the upward-facing ventral retina and the downward-facing dorsal retina containing more of

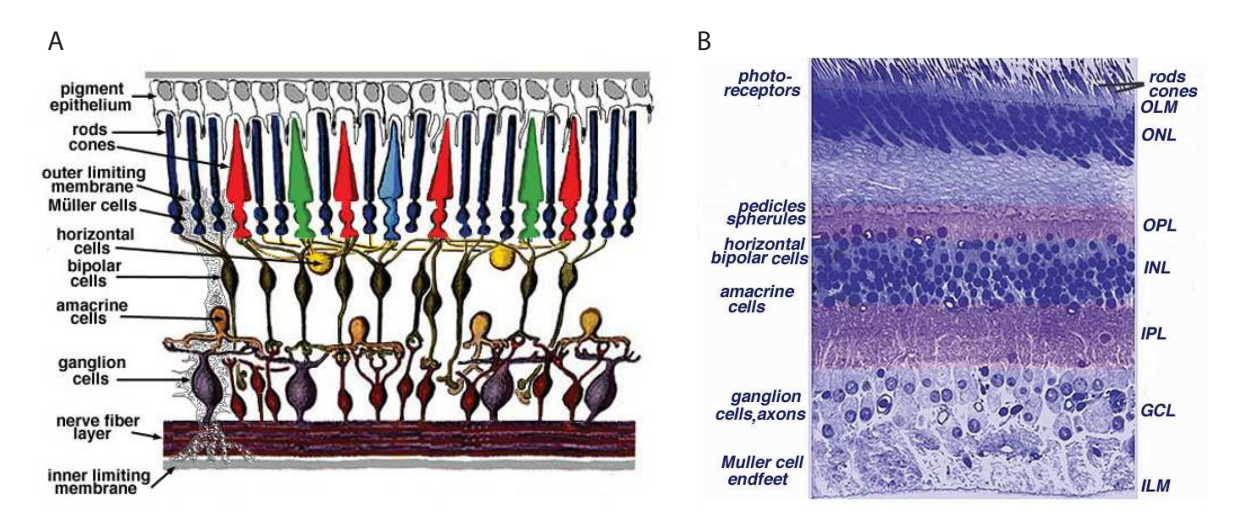


Figure 1.1: A. Schematic diagram of the organization of the Retina. B. Light micrograph of the a vertical section through the central human retina. Lightly adapted from Webvision by Dr. Helga Kolb / CC-BY-NC-4.0

the S or M opsins, respectively (Ortín-Martínez et al., 2014; Szél et al., 1992). This effectively divides the mouse retina into three functional domains: (1) the ventral retina which is dominated by the S opsin, where even 'M cones' co-express both M and S opsin, (2) a narrow Opsin Transition Zone (OTZ) where the S opsin expression drastically falls off (Nadal-Nicolás et al., 2020) and (3) a dorsal retina mostly dominated by the M opsin, with occasional 'true S cones'. This remarkable bias in the spectral sensitivity of the very first layer of the visual system has also been found in species as varied as hyenas and dragonflies. Experiments in mice have shown that from an information theoretic point of view, this non-uniform distribution would allow the photoreceptors to optimally encode contrast information contained in the UV or Green channel in the upper or lower parts of visual scenes (Baden et al., 2013) (see also 1.2.2).

- Horizontal cells are inhibitory interneurons in the retina that mediate lateral interactions between photoreceptors and bipolar cells, playing a crucial role in visual processes such as contrast enhancement or color opponency (Chapot et al., 2017; Joesch & Meister, 2016; VanLeeuwen et al., 2009). These cells have wide dendritic arborizations, creating a lateral network that is further extended through gap junctions, modulating photoreceptor output and contributing to their large receptive field sizes (Shelley et al., 2006). Apart from their somewhat contested role in establishing the inhibitory surrounds of ganglion cells (Chaya et al., 2017; Cook & McReynolds, 1998; Drinnenberg et al., 2018; Mangel, 1991; Ströh et al., 2018), they have recently been shown to also modulate the temporal dynamics of retinal output in a multitude of ways (Drinnenberg et al., 2018).
- Bipolar cells serve as the bridge between the photoreceptors and the retinal ganglion cells. They are broadly categorized into cone bipolar cells, which relay signals from the different cones, and rod bipolar cells, which is one of the outputs of the rod pathways. Recent studies have expanded our understanding of the genetic and functional diversity of bipolar cells in the mouse retina. Single-cell transcriptomic analysis has classified various bipolar cells into around 15 types, uncovering their unique genetic profiles and potential roles in visual signaling (Shekhar et al., 2016). Additionally, research utilizing genetic tools to report Glutamate release by the bipolar cells has provided insights into how these cells contribute to the processing of visual information through their

interplay with amacrine cells (Franke et al., 2017). An important feature of bipolar cell morphology is the laminar manner in which their axons connect to the ganglion cells. The axons of ON and OFF bipolar cells stratify into different sub-layers of the inner plexiform layer, separated by cholinergic amacrine cells, which are then sampled selectively by the dendritic trees of ON or OFF type ganglion cells.

• Amacrine cells Amacrine cells are a highly diverse group of inhibitory interneurons in the retina that play pivotal roles in modulating visual signals before they are transmitted to the brain. In the mouse retina, over 60 distinct types of amacrine cells have identified based on their morphology, neurotransmitter content, and connectivity patterns (Masland, 2012; Yan et al., 2020). These cells are primarily located in the inner nuclear layer and interact within the inner plexiform layer, forming synapses with bipolar cells, ganglion cells, and other amacrine cells. They are essential for various aspects of visual processing, including temporal modulation, contrast enhancement, direction selectivity (Vaney et al., 2012), and the shaping of receptive fields of bipolar cells (Franke et al., 2017).

Recent studies have provided significant insights into the specific functions and connectivity of different amacrine cell types in the mouse retina. For instance, starburst amacrine cells, which release both acetylcholine and GABA, are crucial for direction selectivity. They asymmetrically inhibit direction-selective ganglion cells, allowing these cells to respond preferentially to motion in a specific direction (Euler et al., 2002; Fried et al., 2002). Another example is the All amacrine cell, which plays a key role in scotopic (low-light) vision by linking the rod photoreceptor pathways to cone bipolar cells, effectively transmitting rod signals to both ON and OFF pathways (Demb & Singer, 2012). These findings highlight the complex interplay of various amacrine cell types in refining retinal output and enhancing visual processing in mice.

■ Retinal Ganglion Cells (RGCs) are the output layer of the retina, since their axons make up the optic nerve that proceeds up into the brain. The oldest and broadest possible classification of RGCs is based on whether they fire to increments, decrements, or both, of small spots of light, dividing them into ON, OFF or ON-OFF RGCs respectively (Hartline, 1938; Lettvin et al., 1959). This division of labor allows the retina to use much fewer spikes than a purely ON-ON organisation would have permitted (Gjorgjieva et al., 2014). As the size of the dark or bright spot is made larger, initially the RGC response gets stronger, but after a certain size, the response gets weaker rather than saturating. This was the discovery of an inhibitory surround around the center region, that has the opposite polarity (OFF surround for ON Center and vice-versa) and actively suppresses the signal from the center (Barlow et al., 1957).

Unfortunately for the lovers of simplicity, as stimulation and recording techniques improved, RGCs were found to be picky for much more than just simple brightening or dimming spots. Mouse RGCs are nowadays classified into more than 40 subtypes, each one selective for a specific subset of stimuli (Baden et al., 2016; Goetz et al., 2022), and covering the visual space in non-overlapping 'mosaics' (Wässle et al., 1981; Wässle, 2004). These 'functional types' typically also correspond to unique dendritic morphologies or gene expression profiles (Sanes & Masland, 2015), and target vastly different regions of the brain (Martersteck et al., 2017). Since RGCs represent the final retinal output to the brain, these different functional types can be thought to decompose the input image into parallel channels of extracted features like size, color, speed, direction or orientation. While some of these output features can be somewhat explained on the basis on RGC morphological features, like asymmetry (Kim et al.,

2008) or laminar stratification (Famiglietti & Kolb, 1976) of their dendritic trees, the contribution of the preceding cells of the retinal circuitry in extracting these output features remains an active area of research.

1.1.2 The Superior Colliculus

The Superior Colliculus is an evolutionarily conserved visual structure of the midbrain, that plays a key role in attentional shifts, multisensory integration and innate behaviors ranging from approach to avoidance (Basso et al., 2021). The most superficial layers of the Superior Colliculus (sSC) receive direct visual inputs from the retina and visual cortex. The intermediate layers (iSC) also receive somatosensory and auditory inputs from the cortex, inferior colliculus, cerebellum, and basal ganglia (Doykos et al., 2020; May, 2006). Finally, the deepest layers of the SC (dSC) receive these multimodal inputs from the upper layers and command orienting movements of the eye/pinna/head/body towards targets or away from threats (Basso & May, 2017).

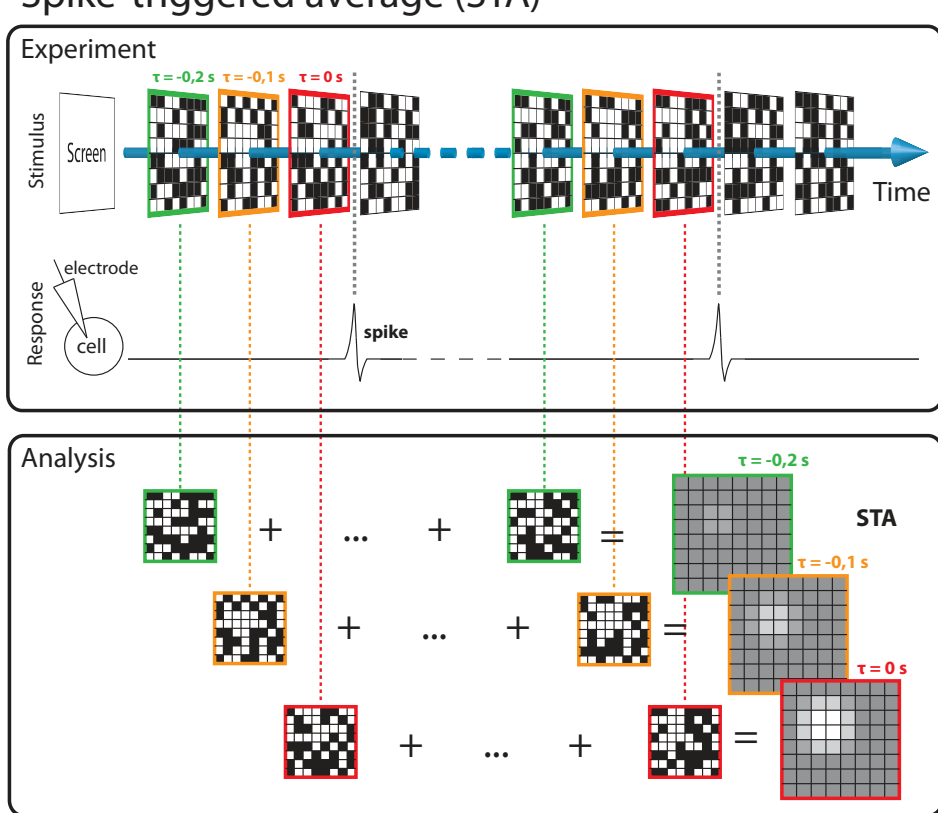
In the mouse brain, 85-90% of all RGC axons innervate the SC, even more than the canonical LGN-cortical pathway (Ellis et al., 2016). The axon terminals of RGC subtypes have been observed to retinotopically stratify at different depths in the SC, forming overlapping maps representing different stimulus features (Hofbauer & Dräger, 1985; Huberman et al., 2009; Kim et al., 2010). Each SC cell can receive inputs from ~5 RGCs and each RGC can synapse ~5 SC cells (Sibille et al., 2022). However, we are only now beginning to understand how these retinal maps affect the way the SC processes visual information. What features conveyed by RGC subtypes continue to be represented by SC neurons and what features are extracted *de novo*, continues to be an active area of research (Malmazet et al., 2024; Reinhard et al., 2019; Shi et al., 2017).

Despite being just one synapse from the retina and being responsible for a plethora of visually guided behaviors, the repertoire and modulation of visual responses in the SC has been much less explored than say, the visual cortex (Y.-t. Li & Meister, 2023). The SC also receives neuromodulatory inputs from a number of brain nuclei (Doykos et al., 2020; May, 2006), hinting the possibility that visual coding in the SC may adapt much more dynamically to visual and behavioral context than the retina can. For instance, (Joshi et al., 2016) investigated the relationships between pupil diameter and neuronal activity in several brain regions, including the SC. They found that changes in pupil size correlate with neuronal activity in the SC, supporting the idea that arousal-linked cholinergic or noradrenergic inputs could influence visual processing in the SC. The SC has also been shown to receive strong inhibitory inputs from the ventral LGN, that can help suppress visual responses during self-motion generated motion blur (Vega-Zuniga et al., 2024).

1.2 Studying the Visual System

1.2.1 Models of Receptive Fields

The Receptive Field (RF) of a neuron is the subspace of stimuli that maximally modulates a neuron's response. Equivalently, it is also described as the stimulus subspace that the neuron's activity carries the most information about. Some of the earliest methods of determining this subspace were developed by Barlow et al. (1957) and Hubel and Wiesel (1959), showing different visual patterns to an anesthetized cat and observing which patterns evoked the most



Spike-triggered average (STA)

Figure 1.2: Diagram showing how the STA is calculated

A stimulus (consisting here of a checkerboard with random pixels) is presented, and spikes from the neuron are recorded. The stimuli in some time window preceding each spike (here consisting of 3 time bins) are selected (color boxes) and then averaged to obtain the STA. The STA indicates that this neuron is selective for a bright spot of light just before the spike, in the top-left corner of the checkerboard. Reproduced without changes © User:StphTphsn / Wikimedia Commons / CC-BY-SA-4.0

spikes in a visual neuron. This continues to be a common method of interrogating neurons, by presenting them with dots/disks of different radii and colors, bars and stripes of different orientations and widths, and noting the 'tuning curves' of responses against different stimulus parameters.

More principled methods of RF determination are borrowed from the system identification theory in electrical engineering. Here, a neuron's response is modeled as a Linear Time Invariant system, and presenting stimuli with known statistical properties, for example, a Dirac's delta impulse or white noise, allows recovering the (linear) transformation that the neuron performs on the stimulus to generate its response. A slightly more general approach models visual neurons as Linear-Nonlinear (LN) units where the product of the RF and the input is passed through a non-linear activation function (Pitkow & Meister, 2012). If a radially symmetric stimulus, like Gaussian or binary white noise, is used as the stimulus, the linear component of the LN model can be estimated by a Spike Triggered Average (STA), where the stimuli before each spike are collected and averaged (Chichilnisky, 2001). Figure 1.2 shows a schematic of how the STA recovers RFs from a white noise stimulus.

While these linear estimates of RFs were a significant upgrade over tuning curves, natural stimuli are rarely gaussian distributed. Newer methods for estimating receptive fields from

arbitrary stimuli deploy information theory to estimate which stimulus properties does the neuron carry the most information about, the so called Maximally Informative Dimensions (MID). And indeed, RFs of neurons do look quantitatively different when they are probed with natural scenes, as opposed to gaussian white noise (Sharpee et al., 2006). See also (Sharpee, 2013) for an excellent review on different strategies for computing receptive fields for visual neurons. Remarkably though, theoretical work has shown that using maximum likelihood to fit LN models is equivalent to estimating the MID with plug-in estimates of entropy (Williamson et al., 2015).

Over the years, various extensions of the LN model have been developed, for example by including multiple linear filters followed by a multi-dimensional non-linearity (de Ruyter van Steveninck & Bialek, 1988; Rajan et al., 2013). Another important extension of the LN model instead allows modeling multiple layered non-linearities, in a so called LNLN model. These models have more expressive power and allow identifying 'subunits' of receptive fields, which in the case of RGCs, likely correspond to contributions from individual bipolar cell (Gollisch & Meister, 2008). The natural extension of stacking more and more layers of linear filters and non-linearities is the Convolutional Neural Networks (CNN) (Fukushima, 1980).

In recent years, CNNs have been used to model the hierarchical non-linear processing performed by the visual system at various stages (Bashivan et al., 2019; Franke et al., 2022; Goldin et al., 2022; McIntosh et al., 2016; Walker et al., 2019). These models even allow researchers to generate putative input images that would maximally activate a given neuron and then test that prediction in-vivo (Bashivan et al., 2019; Walker et al., 2019). Further, the extrapolation power of these neural networks allows researchers to study how the neurons would respond under different behavioral states (Franke et al., 2022) or to slight perturbations of the input image (Goldin et al., 2022), beyond what can be observed easily with limited experimental data.

1.2.2 Constraints and Adaptations: Normative Perspectives

Over the years, a number of prominent computational neuroscience theories have tried to explain sensory neural coding strategies under the guiding principles of information theory (Barlow, 1961; Shannon, 1948). Under this normative umbrella, the goal of a sensory neuron is to recode information about the inputs under different constraints like noise, output levels, metabolic cost, sparsity, etc. Different theories differ in the exact objectives and constraints of model neurons, and the equivalence of these various formulations and their rigorous comparison to physiological data continues to be an active area of research (Chalk et al., 2018; Młynarski et al., 2021). See Weber et al. (2019) for a comprehensive review of the commonalities and differences in these theories, with an emphasis on adaptation. A short summary of the most relevant ideas and observations in this broad topic is highlighted below.

Efficient Coding

The efficient coding hypothesis formalizes the notion of efficiency under constraints by postulating that neurons should maximize the mutual information between the stimulus and response, while minimizing some well defined constraints. Different approaches differ in the exact definition of these constraints and that lends to the broad applicability of this formulation.

For instance, a neuron only has a finite range of response levels, whether membrane potential or spiking rate, with which it must encode the incoming visual signal. A classic study by Laughlin (1981) introduced the idea of how a visual neuron may best utilize its output response

range while taking relative occurrences of its inputs into account. Comparing the neuron to an information channel, the range of responses should be utilized with equal probability, so as to maximize the entropy of the output (Shannon, 1948). To encode a visual input that is itself not uniformly distributed, the same number of output levels must be used for a wider range of less common inputs, as compared to a narrow range of more common inputs. In other words, an efficient visual system would utilize more of its dynamics range in finely disambiguating the most common inputs. Quantitatively, the (normalized) input-output relation of the neuron should be identical to the cumulative distribution of inputs, a phenomenon known as histogram equalization. This was initially found to be the case for the large monopolar cells in the blowfly visual system (Laughlin, 1981) and has since been found repeatedly across sensory neurons (Baden et al., 2013; Clemens et al., 2018; Maravall et al., 2007) even as the distribution of inputs is changed.

Atick and Redlich (1990) formalized how the limited dynamic range of the optic nerve should shape the spatial processing in the retina in order to maximize the amount of sensory information. In order to maximize information transfer under a given channel capacity of the optic nerve, they derived, ab-initio, that retinal filters should have surround antagonism under a high Signal to Noise Ratio (SNR) regime, and perform smoothing to combat noise under low SNR.

Another often quoted fact about the brain is that it consumes 20% of the body's energy input, despite measuring only 2% in bodyweight (Rolfe & Brown, 1997). Since most of this energy is used by neurons for electrical and chemical signalling in the form of spikes, the system must constantly make a trade-off between fidelity and metabolic cost. However, single spikes can be quite noisy, and thus neurons must use metabolically costlier spike bursts for encoding inputs. This delicate balance between noise, metabolic cost and information transmission was tested by (Balasubramanian & Berry, 2002) and salamander RGCs were found to avoid using burst lengths that were either too noisy or too costly, maximising information transmission under these dual constraints.

Sparse Coding

The observation of reducing spike counts has also been studied more abstractly under the notion of Sparse Coding. Visual neurons in the cortex have been found to be highly selective to input features, only rarely firing spikes and only for their preferred stimuli. How can a few neurons firing at any given time carry all the information necessary to encode visual scenes? (Olshausen & Field, 1996) developed a method to decompose a collection of natural images into an ensemble of basis features, under the constraint that only a few of them may be summed at a time to try and recreate the original images. Remarkably, the basis features obtained from this procedure closely resemble the RFs of primary visual cortical neurons. A conceptually similar procedure decomposed an ensemble of natural sounds and found that the wavelet-like basis functions closely resemble the responses of the auditory nerve (Lewicki, 2002).

Predictive Coding

Due to the spatial and temporal structure of natural phenomenon, sensory inputs are highly correlated across space and time. One way to increase encoding efficiency is to use the statistical nature of these correlations to 'predict' inputs from one other, thus reducing the need to transmit redundant information to downstream neurons (Barlow, 1961). This can

be implemented in the spatial domain by making a prediction of the center from surrounding values, and only responding when the center differs from the surround. The resulting operation resembles the antagonistic center-surround observed in retinal ganglion cells (Srinivasan et al., 1982). This operation can also be thought of as a spatial derivative. Similarly in the temporal domain, a derivative filter that subtracts away slow varying, and thus predictive, components of the input would also allow for such predictive coding (Atick & Redlich, 1990; Srinivasan et al., 1982). On a population level, it has been postulated that brain regions higher in the visual hierarchy may maintain and feed back a prediction of the stimulus representation by lower neurons, which the latter can use to detect incoming stimuli that deviate from this prediction (Mumford, 1992; Rao & Ballard, 1999).

Crucially, even though Efficient Coding (Atick & Redlich, 1990, 1992) and Predictive Coding (Srinivasan et al., 1982) use different objectives to derive optimal receptive fields, both normative frameworks predict qualitatively similar effects of SNR on the shape of receptive fields. As the signal-to-noise worsens, for example under dimmer conditions, the surround is no longer predictive of the center, and spatial RFs start to emphasize integrating all available inputs, rather than subtracting away redundancies (Atick & Redlich, 1990; Doi & Lewicki, 2006; Srinivasan et al., 1982). In the temporal domain as well, the filters start to emphasize lower frequency information at higher nose levels (Atick & Redlich, 1992; Srinivasan et al., 1982). Even when the statistics of the inputs change rapidly, these spatiotemporal properties of RGC RFs continue to adapt on a second-by-second basis so as to maximize information transfer about unexpected stimulus features (Hosoya et al., 2005).

1.2.3 Methods of Population Neurophysiology

Brains are made of billions of neurons, and studying the properties of these neurons individually can only get us so far. Over the years, the retina has been a prime model system for developing methods to study neuronal populations *en masse*. The ex-vivo retina preparation, despite being a complete system, closely resembles cultured cells, and was thus one of the first applications of both Mulit-Electrode Array (MEA) and 2 Photon calcium imaging (Denk & Detwiler, 1999; Meister et al., 1994). MEA consist of a 2D arrangement of microscopic conducting contact sites that measure the electric potentials generated by neurons. Since all neurons generate potential gradients in their membranes, either with or without spikes, in principle, the MEA method can be used for studying any brain region of any species.

The 2 photon imaging method, on the other hand, relies on fluorescence microscopy to measure a proxy of membrane potentials. Typically, a dye or protein (known as calcium indicator) is inserted in the neurons that changes its brightness based on the amount of Ca⁺² in the cell, which in turn is modulated (predictably) by the membrane potential. While using calcium imaging in the retina, there is inherent interference due to the light-sensitive nature of the tissue. The excitation or emitted light from fluorescence imaging can activate/saturate photoreceptors, while the visual stimulation can be captured into the imaging. Using the 2 photon effect to separate the spectra of the imaging and stimulation helps ameliorate these effects, but does introduce another artifact of a scanning laser that elicits strong visual responses and is akin to a moving bright bar superimposed on the visual stimulus (Euler et al., 2019).

In Chapter 2, I introduce a new calcium imaging method that separates the two spectra of the photoreceptors and the imaging by using a newer generation of red-shifted calcium indicators. This approach takes advantage of the fact that mice, like most mammals, do not possess red-sensitive L photoreceptors, allowing us to avoid exciting the retinal circuitry with

1. Introduction

the fluorescence imaging light. Appendix A discusses an alternate line of research that this approach allows— specifically, utilising in-vivo 2 photon calcium imaging to reconstruct RFs of RGCs axonal boutons in the SC. In chapter 3, I use a fork-shaped MEA called Neuropixels (Steinmetz et al., 2021), to model RFs from hundreds of SC neurons and study their adaptation to different luminance levels and behavioral states.

CHAPTER 2

Retinal adaptations to visual statistics across elevation

The following article was published in Nature Neuroscience on 23 March 2023. The main article, methods, extended figures and a supplementary table are reproduced here in full, without changes, under the CC-BY-4.0 license from www.nature.com.

Note that references to figures, tables, supplementary materials and citations within the article are self-consistent and self-exhaustive, and thus do not follow the numberings within the rest of the thesis.

Divyansh Gupta, Wiktor Młynarski and Anton Sumser share the first authorship for this work. Specific contributions to the project, article sections and figures are listed below:

Divyansh Gupta designed the study, developed the retinal imaging system, performed

the ex-vivo experiments and analysed the retinal data. I was involved in drafting the results and methods sections and subsequent editing of the entire manuscript. I collected the data for and/or generated Figs

2.2, 2.3, 2.4, 2.8, 2.9, 2.10, 2.11, 2.12, 2.13 and Supp. Table 1

Wiktor Młynarski designed the study, analysed the natural scene statistics, developed

the normative model, and assisted with the analysis of experimental data. He was involved in drafting the introduction, results and methods sections and subsequent editing of the entire manuscript. He generated

Figs 2.1, 2.3, 2.6, 2.7 and wrote Supp. Note 1

Anton Sumser developed the 2-photon imaging system, performed the in-vivo exper-

iments and analysed the SC data. He was involved in drafting the results and methods sections and subsequent editing of the manuscript.

He collected the data for and generated Figs 2.5, 2.10, 2.14

Olga Symonova developed the difference-of-Gaussians model used for ex-vivo analy-

sis and was involved in drafting the methods section. She directly contributed to Figs 2.2 and 2.9 and indirectly to all ex-vivo analysis. performed the pilot experiments to develop the shifting white noise

stimulus. The collected data were not used for final analyses, but these experiments formed the basis for Fig. 2.9 and the stimulus was

subsequently used for all ex-vivo and in-vivo experiments.

Jan Svatoň:

Maximilian Joesch

designed the study, developed the retinal and 2-photon imaging systems, assisted in ex-vivo experiments, conceptualized the shifting white noise stimulus and assisted in analysis of experimental data. He was involved in drafting the introduction, results, and discussion sections and subsequent editing of the entire manuscript. He contributed towards generating Figs 2.2, 2.13.

nature neuroscience



Article

https://doi.org/10.1038/s41593-023-01280-0

Panoramic visual statistics shape retina-wide organization of receptive fields

Received: 19 January 2022

Accepted: 14 February 2023

Published online: 23 March 2023



Divyansh Gupta ^{1,3}, Wiktor Młynarski^{1,3}, Anton Sumser ^{1,2,3}, Olga Symonova¹, Jan Svatoň ¹& Maximilian Joesch ¹□

Statistics of natural scenes are not uniform—their structure varies dramatically from ground to sky. It remains unknown whether these nonuniformities are reflected in the large-scale organization of the early visual system and what benefits such adaptations would confer. Here, by relying on the efficient coding hypothesis, we predict that changes in the structure of receptive fields across visual space increase the efficiency of sensory coding. Using the mouse (*Mus musculus*) as a model species, we show that receptive fields of retinal ganglion cells change their shape along the dorsoventral retinal axis, with a marked surround asymmetry at the visual horizon, in agreement with our predictions. Our work demonstrates that, according to principles of efficient coding, the panoramic structure of natural scenes is exploited by the retina across space and cell types.

The idea that sensory neurons exploit the statistical structure of natural stimuli to minimize the metabolic cost of information transmission has been a guiding principle in neuroscience for over half a century $^{1-3}$. This conceptual framework, known as the efficient coding hypothesis 4 , has provided successful theoretical accounts of sensory coding across species and sensory systems $^{5-8}$ with the retina being the paramount example 9 . Most of the work in the retina has focused on retinal ganglion cells (RGCs), the neurons that relay visual information from the eye to the brain. It has been demonstrated that multiple properties of RGCs—the shape of receptive fields (RFs) $^{10-13}$, organization of RF mosaics 14,15 and the ratio of ON to OFF RGC cell types 16 —can be explained as adaptations to the natural sensory environment. In all the mentioned cases, ab initio theoretical predictions about efficient encoding of natural scenes have led to a better understanding of the physiological and anatomical properties of the retina.

One way a sensory neuron could implement an efficient code is by removing predictable (or redundant) components from sensory stimuli, in a transformation known as predictive coding (PC). This prominent hypothesis suggests that the center–surround structure of RGC RFs is a manifestation of such design principle¹⁰. According to this hypothesis, the surround computes a prediction of the stimulus value in the center of the RF. The predicted value is then 'subtracted' from the center through inhibition, which dramatically reduces the amount of neural resources used to convey the stimulus downstream.

PC and related information–theoretic principles $^{11-13,17}$ typically assume that the structure of natural scenes is uniform across the visual field. However, as demonstrated recently, local contrast and luminance vary prominently across the elevation within the natural visual field of a mouse^{18,19}. Such systematic variation affects the signal-to-noise ratio (SNR) of the input to RGCs. To understand how this inhomogeneous noise structure should shape RGC RFs, we developed a simple, predictive coding model. When adapted to natural statistics of mouse vision, our model generates three key predictions linking the shape of optimal RFs and their position within the visual field. First, the relative surround strength should increase with increasing elevation, due to a consistent increase in brightness from the dim ground to the bright sky. Second, the center size should decrease along the same axis. Third, due to a rapid change of signal intensity between lower and upper FOVs, RFs $centered \, on \, the \, horizon \, should \, have \, strongly \, asymmetric \, surrounds,$ with the upper half being stronger than the bottom one.

To test these predictions experimentally, we established a new system that enables recording and characterization of the RF structure at high resolution, at the scale of thousands of RGCs in a single retina. Such technological development enabled us to collect a dataset of 31,135 RGC RFs covering the entire central retina, which was crucial to test our theory. We found a close agreement between theoretically optimal RF architecture and the variation of RF shapes across the retina, suggesting that RGCs exploit global asymmetries of natural

¹Institute of Science and Technology Austria, Klosterneuburg, Austria. ²Division of Neuroscience, Faculty of Biology, LMU, Munich, Germany.

³These authors contributed equally: Divyansh Gupta, Wiktor Młynarski, Anton Sumser. 🖂 e-mail: maxjosch@ist.ac.at

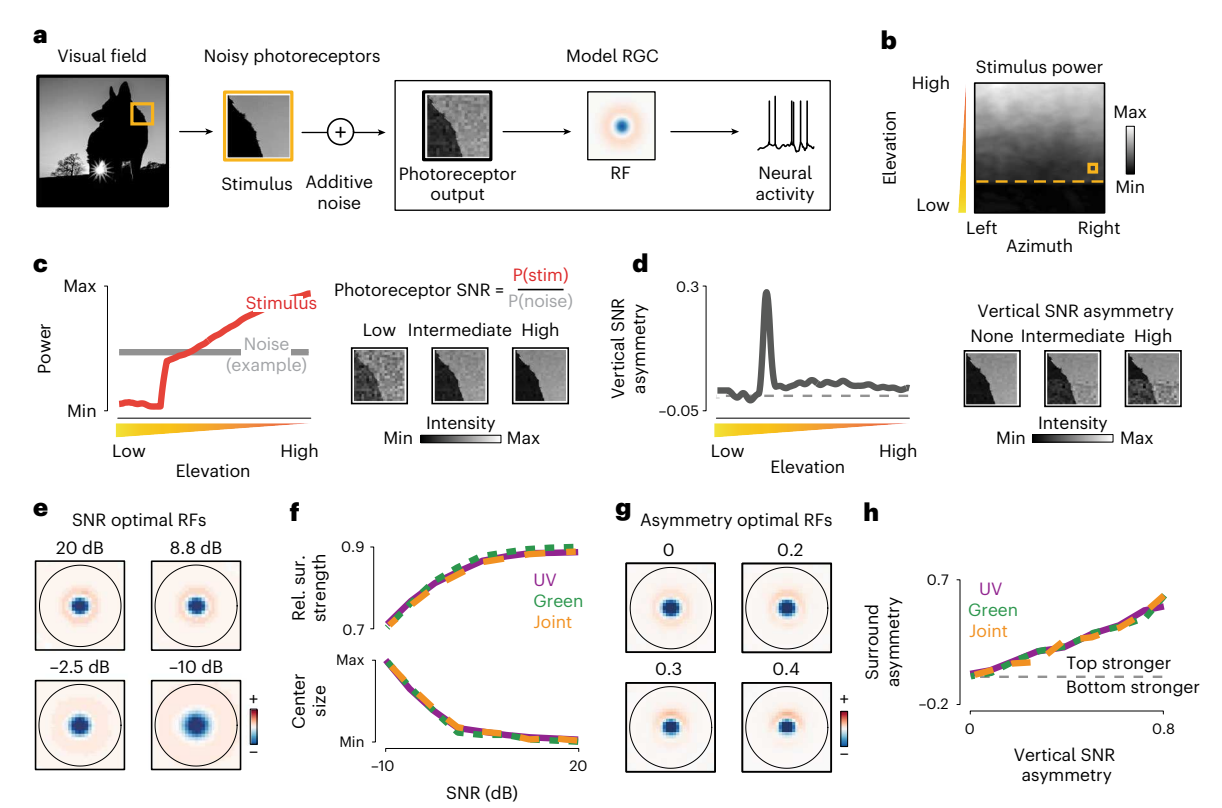


Fig. 1| **Predictive coding and natural scene statistics. a**, Schematic of the linear model of a receptive ganglion cell encoding noisy photoreceptor outputs. **b**, Average stimulus power in the mouse FOV in the UV range (natural image data, courtesy of H. Asari¹⁸). Orange dashed line denotes the simulated horizon. Orange frame illustrates the size of the model RF. **c**, Stimulus power in the UV range (left; red line) and example noise power level (left; gray line) as a function of elevation in the visual field. Increasing stimulus power increases the SNR (right). **d**, Vertical SNR asymmetry in the UV range as a function of elevation in the visual field (left). Change in SNR asymmetry is due to asymmetric power in the stimulus at the horizon line (right). **e**, Predictive coding RFs optimal for different levels of

SNR. RFs were smoothed with a 2×2 -pixel window for display purposes. \mathbf{f} , Relative surround strength (top) and center size (bottom) of optimal predictive coding RFs increase and decrease respectively, with increasing photoreceptor SNR. Purple, green and orange lines correspond to the UV, green and joint spectra, respectively. \mathbf{g} , Predictive coding RFs optimal for different levels of vertical SNR asymmetry. RFs were smoothed with a 2×2 -pixel window for display purposes. \mathbf{h} , Surround asymmetry of optimal predictive coding RFs increases with increasing vertical SNR asymmetry of photoreceptor output. Line colors analogous to \mathbf{f} .

scenes for maximizing coding efficiency. Furthermore, we explored these adaptations across the diversity of functional RGC types²⁰, each thought to share the same physiology, morphology and intraretinal connectivity²¹⁻²⁴. We identified a systematic dorsoventral variation of the RF shape, regardless of the functional type. Finally, we show that these global adaptations are preserved in awake-behaving animals with intact eyes. Our results thus indicate that adaptations to the panoramic natural statistics structure retinal representations used by the brain.

Results

Efficient coding predicts receptive field shapes across the visual field

To understand how the statistical structure of natural scenes shapes RFs across the visual field, we developed a model of sensory coding in RGCs (Fig. 1a). Our approach is closely related to the PC theory, which postulates that RGCs recode outputs of photoreceptor cells to minimize the metabolic cost of sensory information transmission 10 . Following this theory, we modeled neural responses as a linear combination of the RF and natural stimuli, distorted by different sources of constant noise, for example, biochemical or synaptic 9,25,26 (Fig. 1a). The computation performed by such RFs can be understood as the difference of the weighted center of the stimulus and its surrounding neighborhood. Our model generates predictions consistent with PC (Extended Data Fig. 1) as well as related theories of efficient sensory coding 11,13 .

Predictive coding theory of the retina assumes that statistics of natural stimuli are stationary across the visual field¹⁰. However, natural

scenes are spatially inhomogeneous. To understand this inhomogeneity, we examined a set of natural images collected specifically to study mouse vision 18 . In agreement with previous studies 18,19 , we found that the power of the light intensity decreases gradually with the elevation and drops off suddenly close to the simulated horizon line (Fig. 1b,c). Under the assumption of constant noise level, the SNR of photoreceptor outputs (that is, RGC inputs) should therefore follow the analogous pattern (Fig. 1c). Moreover, due to an abrupt change of the stimulus power, stimuli centered at the horizon yield a highly nonuniform SNR pattern (Fig. 1d). To find how such inhomogeneities could affect sensory representations across the retina, we numerically optimized RFs to minimize the strength of neural responses averaged across a set of natural image stimuli (Methods).

The shape of the optimal RF depends on the relative strength and the structure of noise. When the SNR decreases, the center of the optimal RF broadens, and the surround becomes more diffuse (Fig. 1e). These trends are dependent on the relative change but not on the absolute SNR. This qualitative change is manifested in increasing relative surround strength (Fig. 1f) and decreasing center sizes (Fig. 1f). The optimal RF shape is additionally modulated by the spatial pattern of the SNR (Fig. 1g). When the SNR is spatially nonuniform (for example, when the signal is stronger in the upper half of the stimulus), the optimal RF becomes asymmetric (Fig. 1g). This effect is particularly visible in the increasing asymmetry of the surround as a function of SNR asymmetry (Fig. 1h). Because of such systematic variation in the stimulus power across the visual field, the PC model predicted three

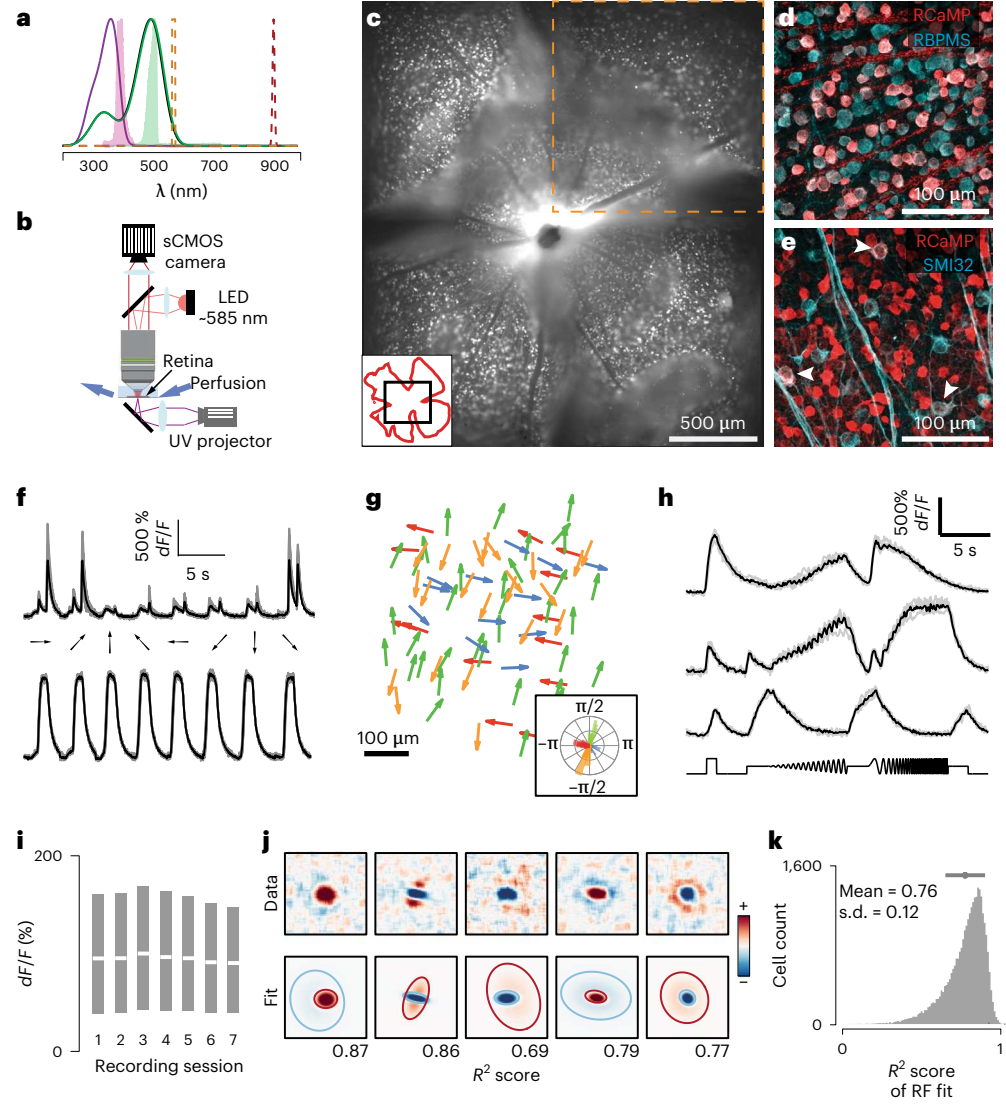


Fig. 2 | **Large-scale retinal receptive field mapping. a**, Normalized absorption spectra of mouse photoreceptors (purple, S-opsin; green, M-opsin). Normalized emission spectra of the UV and green light emitted by the DLP projector (filled purple, UV; filled green, green stimulus light), epifluorescence (orange) and two-photon (red) excitation are overlaid. **b**, Schematic of the epifluorescence imaging setup. **c**, Montage of five consecutively recorded fields (orange dashed box denotes one field) of a whole-mounted mouse retina from a Vglut2-ires-cre; TITL-R-CaMP1.07-D; ROSA26-ZtTA triple-transgenic mouse. Inset: black, imaged montage; red, retinal outline. **d**, Double-labeled immunostaining of RCamp1.07-expressing RGCs (red) and RBPMS (cyan; n = 3). **e**, As in **d** but labeling with SMI32 (cyan). Arrowheads depict double-labeled cells. **f**, Example Ca²⁺ signals (gray, five

repetitions; black, mean) from DS (top) and non-DS (bottom) RGCs. **g**, Example distribution of preferred directions in one FOV. Inset shows a polar plot of DS preference. **h**, Example Ca²⁺ signals to chirp stimulus from three different RGCs (gray, five repetitions; black, mean). **i**, Recording Ca²⁺ signal stability across sequentially imaged FOVs for nine retinas (each session lasted -25 min, 3–7 sessions per retina). White lines denote medians, and minima and maxima of the gray bars indicate the 25th and 75th percentile range of the dF/F distribution, respectively. **j**, Example RFs recorded using 'shifting' white noise (top) and their respective parametrizations (bottom). Blue and red ellipses correspond to 2 s.d. contours of the ON and OFF Gaussians, respectively. **k**, Histogram of goodness of fit for all recorded RFs.

qualitative links between the position of a neuron in the retina and the shape of its RF. First, the strength of the RF surround relative to the center should be increasing with elevation across the visual field. Second, the size of the center should increase in the opposite direction. Third, RFs located at the horizon should have surrounds that are substantially stronger in the upper half than in the lower half. Such distribution of RF shapes would indicate that RGCs exploit global statistics of the visual field to maximize the efficiency of sensory coding. These three predictions stand in contrast to the dominant view that RGC RFs are uniform across the retinal surface. Furthermore, predictions of the PC model are reproducible across different ranges of the light spectrum (Fig. 1f,h) and sets of natural stimuli (Extended Data Fig. 1) and depend primarily on weak assumptions about the correlation

structure of natural images¹⁰ (Supplementary Note 1 and Extended Data Fig. 2). We thus consider them to be a robust consequence of the efficient coding hypothesis.

Large-scale characterization of receptive fields across the retina

Testing these theoretical predictions requires a high-resolution characterization of RGC RFs from extended regions of the retinal surface. Currently, however, it is not practical to perform such large-scale characterizations with any of the existing methods. Multiphoton imaging approaches can measure large numbers of RGCs 20,27 , but only at a moderate throughput (-150 RGCs at a time 20,27). Multielectrode array recording approaches have improved this number but are limited

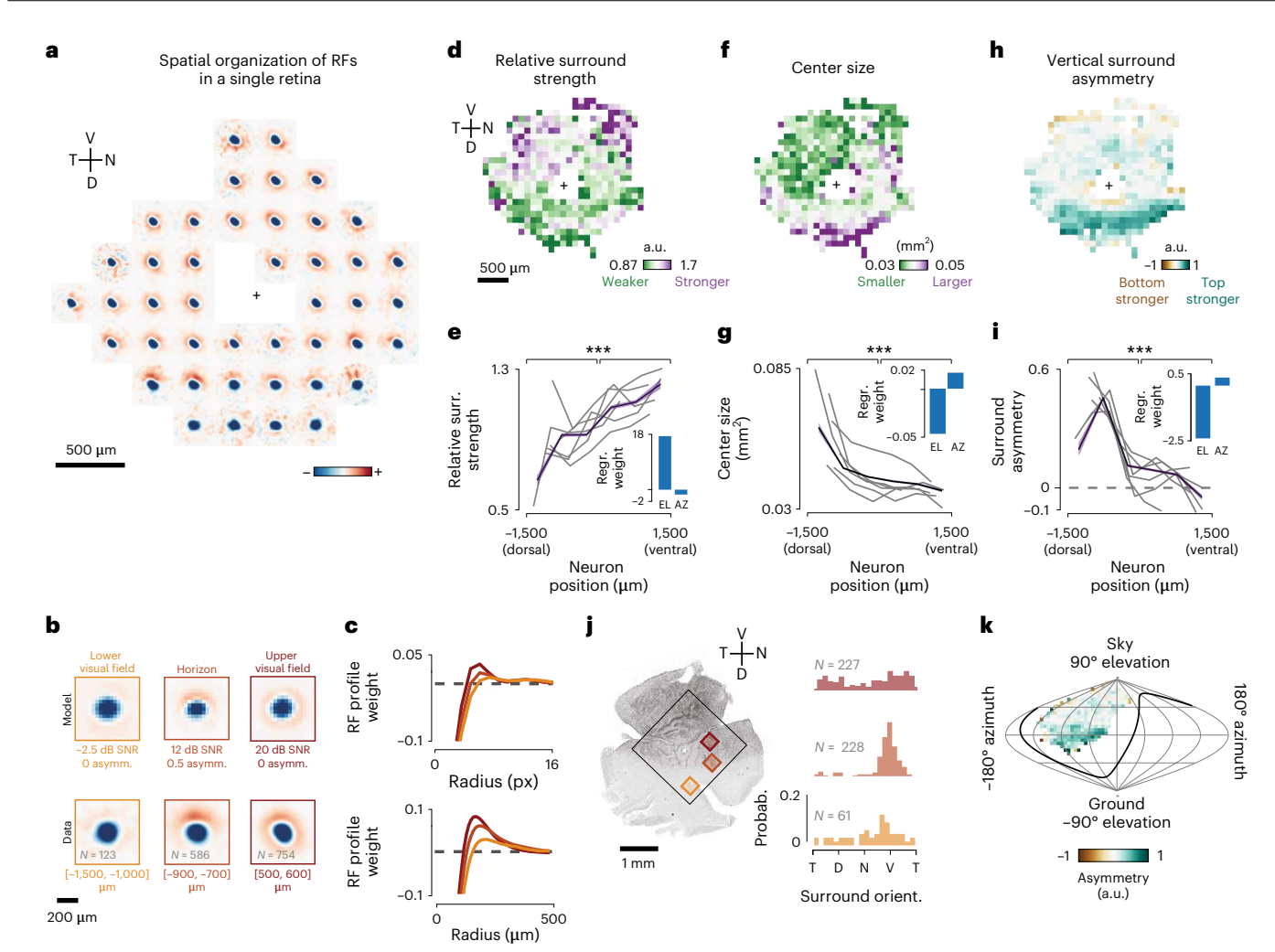


Fig. 3 | **Retina-wide receptive field architecture. a**, Average spatial RFs of all RGCs pooled from square bins of 300 μm in size at different positions of one retina ($n = 64 \pm 52$ cells per bin; black cross indicates the optic nerve head). **b**, Top row, optimal RFs predicted by the model at different elevations of the visual scene. Bottom row, average spatial RFs of neurons along different dorsoventral locations on the retina. **c**, Top, radial profiles of model RFs at different SNR levels. Bottom, mean radial profiles of RGC RFs in bins along the dorsoventral axis. **d**, Mean relative surround strengths of RGCs within 100-μm bins, pooled from n = 6 retinas. **e**, Relative surround strengths for RGCs within six equally spaced bins along the dorsoventral axis (color indicates the mean and s.e.m. pooled from n = 15,686 RFs, gray lines denote individual retinas, and the inset shows linear regression weights of RF parameter on elevation

(EL) and azimuth (AZ)). **f,h**, Same as **d**, but for center size and vertical surround asymmetry, respectively. **g,i**, Same as **e**, but for center size and vertical surround asymmetry, respectively. **j**, Left, one of the retinas, immunostained for S-opsin. Black box shows the region imaged for RF mapping. Right, normalized histograms of surround orientations of RGCs within corresponding bins marked on the left. **k**, Data from **h** overlaid on a sinusoidal projection of visual space (n = 6 retinas). The animal is centered at 0° latitude and 0° longitude facing toward the viewer, and the black line shows the area of the visual field viewed by one eye. P values for two-sided Kolmogorov–Smirnov test: 6.11×10^{-5} (**e**), 2.84×10^{-4} (**g**) and 1.16×10^{-5} (**i**); see Extended Data Fig. 6 for extensive statistical comparisons). V, ventral; N, nasal; D, dorsal; T, temporal. a.u., arbitrary units.

by the recording area that is placed on top of the electrode array¹⁵. Moreover, RF estimates generated by current approaches lack a clear surround structure²⁰. To circumvent these limitations, we designed a high-throughput and low-cost epifluorescence approach that enables imaging a larger field of view (FOV; 1.7 mm² sampling at ~1 μm per pixel) and permits >1 h-long recordings of the same FOV while avoiding artifacts caused by small retina wrinkles and laser scanning. Our method takes advantage of red calcium sensors (for example, RCamp1.07)²⁸ that separate the Ca²⁺ indicator's red-shifted excitation light from the opsin absorption spectrum (Fig. 2a,b and Methods), and allows robust responses to ultraviolet (UV) visual stimulation. We used the VGluT2-cre driver line to specifically target RGCs (Fig. 2c), leading to a uniform expression across the entire retina. All RCamp1.07-positive somata correspond to RGCs, as seen by the RGC-specific marker RBPMS²⁹ (Fig. 2d). Double-positive cells accounted for ~40% of all RGCs. This expression pattern appears to be RGC-type specific, as seen

by co-labeling of SMI32 alpha-RGCs. Alpha-RGCs were consistently excluded from the expression profile, apart from a single, sparse and spatially distributed type (Fig. 2e). Using this line, we were able to reproduce and expand previous large-scale imaging results in single retinas, as seen in direction-selective (DS) and non-DS responses (Fig. 2f), the cardinal DS response distributions (Fig. 2g) and clustering and reproducibility of responses to changes in frequency, contrast and luminance, known as the 'chirp' stimulus²⁰ (Fig. 2h and Extended Data Fig. 3). By sequentially recording 3-7 FOVs (Fig. 2c), each for approximately 25 min, we could record neural activity from up to ~6 mm² of retinal surface (~40% of the total retinal area). By experimental design, the position of each FOV was random. Moreover, the strength of the functional responses in each consecutive session was unaltered (Fig. 2i). Importantly, using a new 'shifting' white-noise approach, where the checker positions are randomly shifted to increase the RF spatial resolution (Extended Data Fig. 4a-f, Methods and ref. 30), we were able

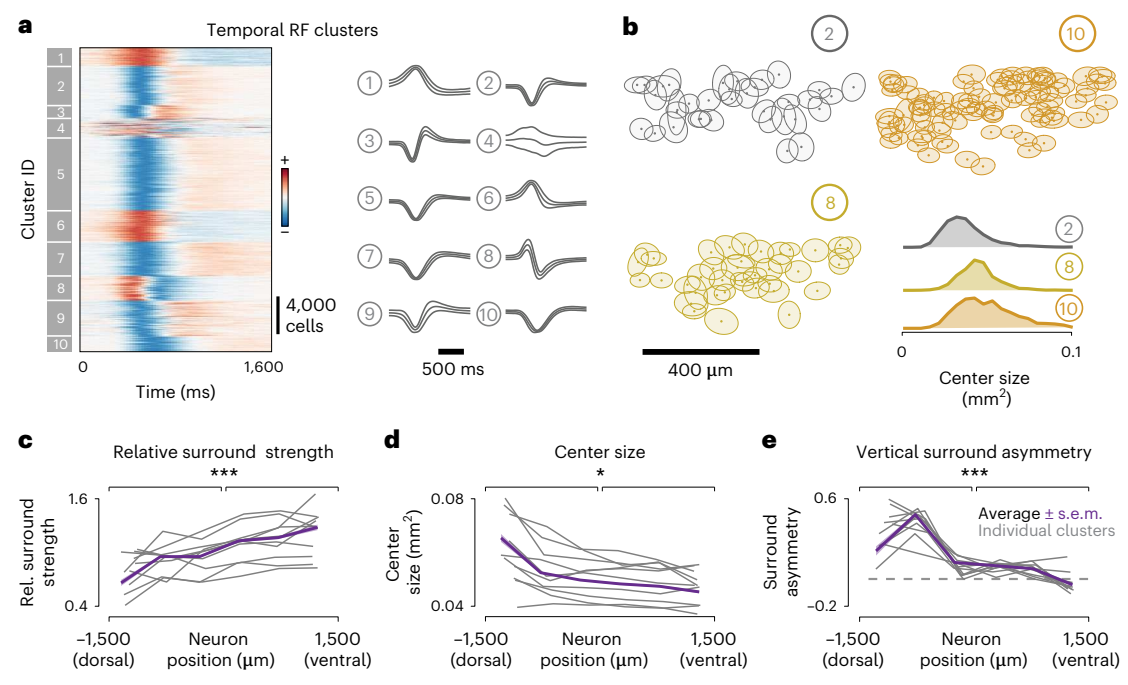


Fig. 4 | **Global adaptation across retinal pathways. a**, Left, temporal RFs of 31,135 RGCs, grouped by cluster membership. Right, mean and s.d. of temporal RFs in each cluster. **b**, Locations of RGCs (dots) and their RF centers (filled ellipses—1 s.d. of the center Gaussian) belonging to three different clusters in a small region of one retina. Bottom right, distribution of center sizes for these

three clusters. **c**-**e**, Trends for relative surround strength (**c**), center size (**d**) and vertical surround asymmetry (**e**) for cells within each cluster (gray) and pooled from all clusters (color), binned as in Fig. 3e. (P values for two-sided Kolmogorov–Smirnov test: 6.17×10^{-5} (**c**), 0.02 (**d**) and 2.62×10^{-7} (**e**).

to estimate high-resolution and high-SNR spatiotemporal RFs for ~85% of recorded cells (Fig. 2j). The quality of these RF estimates allowed for automatic parametrization of the spatial RF into the center and surround using a difference of Gaussians model (Figs. 2j,k, Extended Data Fig. 4g–l and Methods). In total, we recorded 11 retinas, reconstructing and parametrizing 31,135 spatiotemporal RFs, enabling an unprecedented opportunity to index RGC responses across single retinas. This methodology will enable functional developmental screens and circuit dissections due to its simplicity, efficiency and affordability, extending the current retinal research toolbox.

Receptive fields are adapted to anisotropic natural scene statistics

Taking advantage of the high-resolution RFs, we examined variations in RF shapes and strengths across the retina. Given that the PC model does not determine the polarity of the optimal RF and to globally compare all retinal RFs, ON-center RFs were flipped in sign, such that all centers were negative, and all surrounds were positive. This allowed us to pool across all cells within small bins on the retinal surface and visualize the average spatial RF at different locations of the retina (Fig. 3a and Extended Data Fig. 5a). We observed a general and reproducible trend across 11 retinas: a streak-shaped area where all RF surrounds were oriented toward the optic nerve, and below which, hardly any RF surrounds were observed (Fig. 3a and Extended Data Fig. 5a). To compare these spatial variations of RFs with our theoretical predictions, we oriented six of the recorded retinas to a common coordinate system using the immunohistochemically determined S-opsin gradient. Average RFs in the ventral, centrodorsal and peripheral-dorsal retina (Fig. 3b) qualitatively matched model RFs predicted for the upper, medial and lower visual fields, respectively (Fig. 3b). To confirm the change of relative surround strengths independently from surround asymmetry, we computed the radial profiles of RFs and these also strongly resembled the radial profiles for model RFs (Fig. 3c).

Overall, model RFs qualitatively reproduced all aspects of average spatial RFs across different elevations with remarkable detail.

To measure these phenomena quantitatively, we made use of the RF parametrizations and pooled RF parameters for all cells in different two-dimensional (2D; Fig. 3d-h) or one-dimensional (1D; Fig. 3e-i) bins across the retina. In line with our theoretical predictions (Fig. 1f), our analysis shows that the relative surround strength increases gradually along the dorsoventral axis (Fig. 3d), a trend visible in every single retina (Fig. 3e). Next, we explored if we could observe any global change in RF center size. As predicted (Fig. 1f), center sizes decreased only across the dorsoventral axis (Fig. 3f,g and Extended Data Fig. 6). While examining the spatial distribution of differences in upper and lower halves of the RF surrounds, we identified a consistent and prominent asymmetric streak in the dorsal retina, between 700 and 900 µm dorsally from the optic nerve (Fig. 3h,i), as one would expect from asymmetric visual inputs (Fig. 1e). Accordingly, linear regressions weights were substantially stronger in elevation, but not azimuth, for all three trends (Fig. 3e-i and Extended Data Fig. 6). Overlaying the measured RF asymmetries with the opsin gradient indicated that the asymmetry is pronounced in the opsin transition zone (Fig. 3j). To test whether this streak corresponds to the horizon line within the animal's visual field, we transformed the retinal coordinates to visual coordinates³¹ and used the S-opsin gradient³² to define the dorsoventral axis (Fig. 3j,k and Methods). In visual coordinates, the center of this asymmetric streak is located at 0° elevation, spanning the entire azimuth of our imaged FOVs (Fig. 3k), in line with our theoretical predictions (Fig. 1c). Finally, these trends also aligned in five additionally imaged retinas, where the true orientation could not be determined by the opsin gradient (Extended Data Fig. 7).

Adaptations to natural scene statistics across retinal pathways It has long been assumed that specific RGC pathways have stereotyped response properties, shaped by the interactions between direct

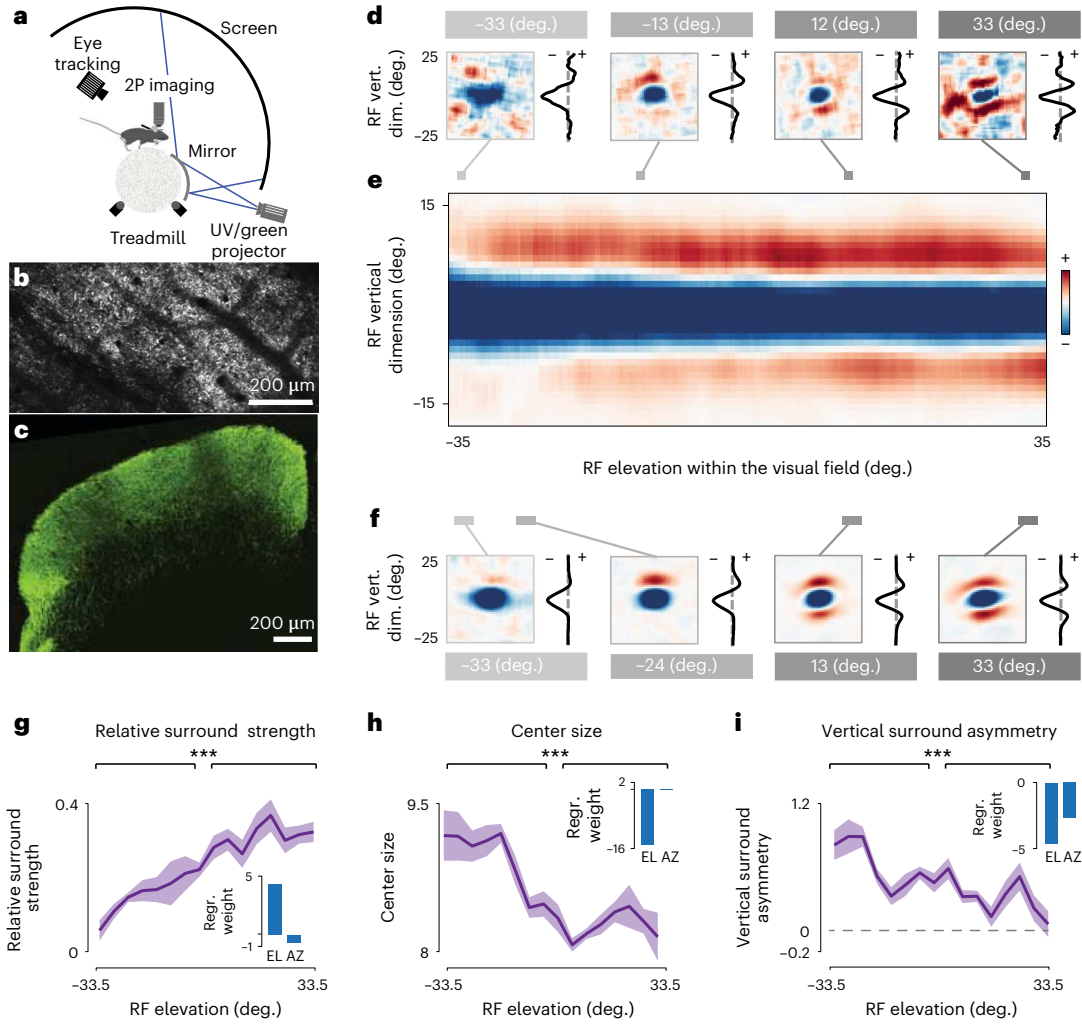


Fig. 5 | **Colliculus-wide retinal ganglion cell's receptive field architecture. a**, Schematic of in vivo multiphoton imaging setup. **b**, FOV of a standard multiphoton recording of RGC axons expressing GCaMP8m in the SC (maximum projection, n=10 sessions of three animals). **c**, Immunostaining of GCaMP8m of an example coronal section of the SC (n=3 animals), showing homogeneous RGC labeling across the visual layers (green). **d**, Example RGC bouton RFs recorded using 'shifting' white noise (left) and their respective vertical 1D center profiles (1D RFs; right) at different elevation levels (gray lines). Note, ON-center RFs were inverted as done in Fig. 3. **e**, Average 1D RFs in 0.22° bins over elevation

(smoothed horizontally in a 5° Gaussian window for display purposes). **f**, Example average RFs binned at a 4.1° visual angle (left), with their respective 1D RFs (right) at different elevation levels (gray bars). **g**, Relative surround strength of 4.1° binned and parametrized average 1D RFs; shading indicates the s.e.m. across azimuth bins (Extended Data Fig. 9g–i). Inset shows linear regression weights of individual bouton (n = 9,810) 1D RF parameters on elevation (EL) and azimuth (AZ). **h**,**i**, As in **g**, but for center size and vertical asymmetry, respectively. (P values for two-sided Kolmogorov–Smirnov test: 2.91×10^{-10} (**g**), 1.16×10^{-12} (**h**) and 1.48×10^{-6} (**i**). 2p, two photon.

excitation in their center and indirect inhibition in their surround³³. Thus, one would expect that these center-surround interactions are uniform across visual space for most RGC pathways. To assess the specificity of the observed RF adaptations across functional RGC pathways, we clustered cells based on the temporal RF profile of 31,135 RGCs into functional groups using a Gaussian mixture model (GMM), as done previously²⁰. Consistent with the proportion of RGCs labeled in our line (Fig. 2d), we defined ten functional clusters (Fig. 4a). Chirp responses were not used for clustering because we observed reliable responses only in RGCs with weak surrounds. Therefore, for RGCs with strong surround, the chirps did not help us to match cluster identities (Extended Data Fig. 3c,d), despite finding new response properties that would have aided classification (for example, clusters 3, 11 and 14; Extended Data Fig. 3b). Each cluster group had distinctly shaped temporal filters, corresponding to different functional properties such as ON or OFF selectivity, transient or sustained responses, and monophasic or biphasic selectivity, as seen in their average profiles (Fig. 4a). Cluster membership statistics were conserved across different retinas (Extended Data Fig. 8). Moreover, the relative positions of RGCs belonging to individual clusters tile the retina in a mosaic-like arrangement in many cases (Fig. 4b), confirming that some clusters are indeed functionally distinct and irreducible RGC types¹⁵. As expected, many clusters represent a combination of RGC types that cannot be identified solely by their temporal profiles (Fig. 4b, cluster 10; see Supplementary Table 1 for tiling statistics). We next used this classification and looked at the relative surround strength, center size and asymmetric strength across clusters (Fig. 4c). As with the global pooling of RF (Fig. 3), cells in each functionally defined cluster increase their relative surround strengths gradually in the dorsoventral axis and decrease their center sizes accordingly. Moreover, all clusters contribute to the asymmetric streak (Extended Data Fig. 8c), consistent with the distribution of asymmetries in the opsin transition zone, where most cells have a strongly oriented surround with a ventral bias (Fig. 3k). All three trends were statistically significant for all clusters in elevation,

but not azimuth (Supplementary Table 1). These results indicate that a substantial proportion of RGC pathways adapt to the constraints imposed by natural statistics.

In vivo panoramic receptive field anisotropies match predictions

To test whether the adaptations to the panoramic visual scene statistics affect sensory coding during behavior in naturalistic conditions, we decided to map RFs of the RGC axonal terminals in the superior colliculus (SC; Fig. 5a,b). These experiments have the advantage of testing our hypothesis in retinas that retain the complete adaptation machinery, from an attached pigment epithelium to functioning pupil constriction. Moreover, they provide important additional insights into the effects of the M-cone and rod pathways, which are saturated in our ex vivo retinal imaging system. For this purpose, we expressed the calcium indicator GCaMP8m³⁴ in RGCs, using adeno-associated viruses (AAVs) in three mice. Subsequent implantation of a cranial window above the SC allows for visualization of RGC axonal terminal activity with two-photon calcium imaging in awake, behaving mice. The FOV varied for each recording from 0.32 to 1.85 mm² (median of 0.68 mm²) of superficial SC surface (Fig. 5b), encompassing 23 to 57 (median of 41) visual degrees in elevation. GCaMP8m expression spread homogeneously across the SC (Fig. 5c). Using the same previously used 'shifting checker' stimulus, we recorded 53,000 terminals in total, reconstructing 10,000 RFs above our quality index (Methods). Compared to the RFs recorded from ex vivo retinas, in vivo measured RFs were blurred along the main axis of saccadic movements (Figs. 2d and 5d; RFs). Thus, to compare across animals, we aligned the RFs of each animal to their respective saccadic plane, which, due to the head fixation, had one consistent axis parallel to the ground to each animal as shown previously³⁵ (Extended Data Fig. 9a-c) and corrected the mouse head position to match the retinal coordinates (Methods). To avoid any bias due to eye movements, we then used the 1D profiles (1D RFs) of the orthogonal axis for further analysis (Figs. 5e). By binning and averaging 1D RFs along the lateromedial axis, spanning from the lower visual field to the higher visual field (Fig. 5fg-i and Extended Data Fig. 9d), the three predicted trends became visible: (1) the surround strength increased, (2) the center size reduced and (3) the surround became more symmetric. Similarly to our retinal results (Fig. 3b), the mean 2D RFs qualitatively matched model RFs predicted for the upper, medial and lower visual fields (Fig. 5f). Next, we analyzed the RF parameters on mean 1D RFs across visual space. As with previous results, the RF properties were significantly different above and below the horizon and had substantial regression weights on elevation (Fig. 5g-i) but not $on \, azimuth \, (Extended \, Data \, Fig. \, 9h-I). \, Consistently, the \, average \, visual \,$ maps (Extended Data Fig. 5b) resembled the ones measured ex vivo (Fig. 3d-h). Thus, our in vivo results provide independent corroboration that the visual system is adapted to the constraints imposed by the panoramic natural statistics.

Discussion

In this study, we leveraged a new, high-throughput neural imaging setup (Fig. 2) to identify a novel kind of adaptation to panoramic scene statistics in the retina. In agreement with theoretical predictions derived from the efficient coding framework (Fig. 1), our experimental results indicate that the global RF architecture is adapted to encode panoramic natural scenes efficiently (Figs. 3 and 4). These results were further corroborated in RGC terminals of awake animals (Fig. 5), indicating that panoramic, efficient representations impact downstream processing during behavior. Classically, RGCs are known to dynamically change the strength of the RF surround in response to varying light levels 16,37, which is thought to further increase the efficiency of sensory coding 18,38,39. Our findings demonstrate that, in addition to such dynamic effects, RF shapes are also determined by static factors, namely their position within the visual field. In that way, the retina simultaneously

exploits the large-scale spatial and fine-scale temporal structure of the visual space.

How could the visual system establish such global RF architecture without fine-tuning each RGC pathway independently? One partial mechanism would be the nonuniform distribution of spectral sensitivity across the retina³². Such distribution has been discussed to be relevant for color vision⁴⁰, contrast coding^{19,41} and the detection of aerial predators in the sky⁴², but simultaneously, could influence the static RF adaptations. For example, whereas the mouse retina has green light-sensing photoreceptors across the entire retina (M-opsin and Rod-opsin), UV sensitivity follows a sharp dorsoventral gradient (S-opsin)³². From the RGC's perspective, both inputs will be added at mesopic conditions, leading to a net enhancement of the UV sensitivity from the ground to the sky. Our in vivo results support this perspective by corroborating the ex vivo findings in an intact eye. Intriguingly, in vivo and ex vivo measured RFs differ subtly. Whereas ex vivo RFs show a clear asymmetrical peak at the horizon, in vivo RFs are more asymmetric across large proportions of the visual field (Fig. 5j). This is consistent with PC predictions because natural image patches located above the horizon tend to be vertically asymmetric (Fig. 1d) due to a gradient of stimulus power (Fig. 1b). Such an RF pattern indicates that other mechanisms, apart from the S-opsin gradient, have to be involved. One possibility could be the circuitry mediating the asymmetric surround of J-RGCs^{33,40}, which is ventrally displaced and sensitive to M-cones and rods. Interestingly, the vertical gradient of stimulus power will flatten at lower ambient light levels, for example, at dusk and dawn. In conjunction, the relative strength of UV sensitivity and the antagonistic surround would also decrease 36,37. In these conditions, efficient coding hypothesis would predict a more homogeneous RF distribution across the dorsoventral axis. Conversely, the horizon will become more prominent in photopic conditions, where rods are less active. In such situations, the in vivo RF architecture should have a localized asymmetric streak, as measured in our ex vivo data. It would be revealing to test if the retina-wide RF organization is dynamically reshaped under scotopic and photopic conditions. Finally, to fully benefit from this panoramic retinal code, the eye should maintain a relatively constant position on the horizon. In agreement with this idea, eye and head movements stabilize the retinal image remarkably well, on average ~10° in azimuthal angle, during behavior $^{35,\!43}.$

A distinct, yet related question can be asked about the emergence of DS computations in retinorecipient areas, such as the SC, where neurons integrate input from the entire retina, including the asymmetric streak. DS encoding can emerge as a consequence of an asymmetric and time-shifted surround, as shown before ^{33,44}. Consistent with the measured center–surround asymmetry, some studies have described these neurons as sensitive to upward motion ⁴⁵, whereas others do not find such specificity ^{46,47}. The efficient coding interpretation, such as the one adopted here, suggests that the key to resolving this puzzle might be understanding the statistics of what the animal ought to see in nature.

Our theoretical predictions established qualitative links between properties of RFs and their elevation within the visual field. They can be therefore thought of as a first-order approximation of how the retina is adapted to large-scale, spatial statistics of natural scenes. The exact pattern of global retinal adaptation should vary across species occupying diverse environments. It has been found that dorsoventral opsin gradients are present in many different mammalian species. For example, the rabbit, Chilean subterranean rodent cururo, European mole, the shrew and even the spotted hyena^{42,48} show higher S-opsin expression in the ventral retina. However, not all ecological niches are identical. For example, in dense forests, the vertical gradients of luminance and contrast are less prominent, and a clear horizon line might not be apparent. Interestingly, forest mice species whose opsin distribution has been described present a spatially uniform opsin distribution⁴⁹. This further strengthens our hypothesis, which relates the global organization of the retina to the statistics of the ecological visual field. Understanding this adaptation in more detail will require a careful analysis of stimuli from the ecological sensory niche, as well as an estimation of biophysical parameters such as biological SNR, RF size and tiling to refine our theoretical predictions. The combination of these approaches will be a critical requirement for building a more general theory of vision across the animal kingdom⁵⁰.

Online content

Any methods, additional references, Nature Portfolio reporting summaries, source data, extended data, supplementary information, acknowledgements, peer review information; details of author contributions and competing interests; and statements of data and code availability are available at https://doi.org/10.1038/s41593-023-01280-0.

References

- Shannon, C. E. A mathematical theory of communication. Bell Syst. Tech. J. 27, 379–423 (1948).
- Barlow, H. B. Possible principles underlying the transformation of sensory messages. in *Sensory Communication* (ed. W. A. Rosenblith) MIT Press (1961).
- Attneave, F. Some informational aspects of visual perception. Psychol. Rev. 61, 183–193 (1954).
- Laughlin, S. A simple coding procedure enhances a neuron's information capacity. Z. Naturforsch. C. Biosci. 36, 910–912 (1981).
- Nemenman, I., Lewen, G. D., Bialek, W. & de Ruyter van Steveninck, R. R. Neural coding of natural stimuli: information at sub-millisecond resolution. PLoS Comput. Biol. 4, e1000025 (2008).
- Fairhall, A. L., Lewen, G. D., Bialek, W. & de Ruyter Van Steveninck, R. R. Efficiency and ambiguity in an adaptive neural code. *Nature* 412, 787–792 (2001).
- Rieke, F., Bodnar, D. A. & Bialek, W. Naturalistic stimuli increase the rate and efficiency of information transmission by primary auditory afferents. *Proc. Biol. Sci.* 262, 259–265 (1995).
- Olshausen, B. A. & Field, D. J. Emergence of simple-cell receptive field properties by learning a sparse code for natural images. *Nature* 381, 607–609 (1996).
- 9. Rieke, F. & Rudd, M. E. The challenges natural images pose for visual adaptation. *Neuron* **64**, 605–616 (2009).
- Srinivasan, M. V., Laughlin, S. B. & Dubs, A. Predictive coding: a fresh view of inhibition in the retina. *Proc. R. Soc. Lond. B Biol. Sci.* 216, 427–459 (1982).
- Doi, E. & Lewicki, M. S. A simple model of optimal population coding for sensory systems. *PLoS Comput. Biol.* 10, e1003761 (2014).
- 12. Atick, J. J. & Redlich, A. N. What does the retina know about natural scenes? *Neural Comput.* **4**, 196–210 (1992).
- 13. Karklin, Y. & Simoncelli, E. P. Efficient coding of natural images with a population of noisy linear–nonlinear neurons. *Adv. Neural Inf. Process.* Syst. **24**, 999–1007 (2011).
- 14. Balasubramanian, V. & Sterling, P. Receptive fields and functional architecture in the retina. *J. Physiol.* **587**, 2753–2767 (2009).
- Roy, S., Jun, N. Y., Davis, E. L., Pearson, J. & Field, G. D. Inter-mosaic coordination of retinal receptive fields. *Nature* 592, 409–413 (2021).
- Ratliff, C. P., Borghuis, B. G., Kao, Y.-H., Sterling, P. & Balasubramanian, V. Retina is structured to process an excess of darkness in natural scenes. Proc. Natl Acad. Sci. USA 107, 17368–17373 (2010).
- Chalk, M., Marre, O. & Tkačik, G. Toward a unified theory of efficient, predictive, and sparse coding. *Proc. Natl Acad. Sci. USA* 115, 186–191 (2018).
- 18. Abballe, L. & Asari, H. Natural image statistics for mouse vision. *PLoS ONE* **17**, e0262763 (2022).
- Qiu, Y. et al. Natural environment statistics in the upper and lower visual field are reflected in mouse retinal specializations. *Curr. Biol.* https://doi.org/10.1016/j.cub.2021.05.017 (2021)

- 20. Baden, T. et al. The functional diversity of retinal ganglion cells in the mouse. *Nature* **529**, 345–350 (2016).
- Sümbül, U. et al. A genetic and computational approach to structurally classify neuronal types. Nat. Commun. 5, 3512 (2014).
- 22. Helmstaedter, M. et al. Connectomic reconstruction of the inner plexiform layer in the mouse retina. *Nature* **500**, 168–174 (2013).
- 23. Macosko, E. Z. et al. Highly parallel genome-wide expression profiling of individual cells using nanoliter droplets. *Cell* **161**, 1202–1214 (2015).
- Masland, R. H. The neuronal organization of the retina. Neuron 76, 266–280 (2012).
- 25. Baylor, D. A., Nunn, B. J. & Schnapf, J. L. The photocurrent, noise and spectral sensitivity of rods of the monkey *Macaca fascicularis*. *J. Physiol.* **357**, 575–607 (1984).
- Schneeweis, D. M. & Schnapf, J. L. The photovoltage of macaque cone photoreceptors: adaptation, noise, and kinetics. *J. Neurosci.* 19, 1203–1216 (1999).
- 27. Sabbah, S. et al. A retinal code for motion along the gravitational and body axes. *Nature* **546**, 492–497 (2017).
- 28. Bethge, P. et al. An R-CaMP1.07 reporter mouse for cell-type-specific expression of a sensitive red fluorescent calcium indicator. *PLoS ONE* **12**, e0179460 (2017).
- 29. Tran, N. M. et al. Single-cell profiles of retinal ganglion cells differing in resilience to injury reveal neuroprotective genes. *Neuron* **104**, 1039–1055 (2019).
- 30. Pamplona, D. et al. Receptive field estimation in large visual neuron assemblies using a super-resolution approach. *J. Neurophysiol.* **127**, 1334–1347 (2022).
- 31. Sterratt, D. C., Lyngholm, D., Willshaw, D. J. & Thompson, I. D. Standard anatomical and visual space for the mouse retina: computational reconstruction and transformation of flattened retinae with the Retistruct package. *PLoS Comput. Biol.* **9**, e1002921 (2013).
- 32. Nadal-Nicolás, F. M. et al. True S-cones are concentrated in the ventral mouse retina and wired for color detection in theupper visual field. *Elife* **9**, e56840 (2020).
- Kim, I.-J., Zhang, Y., Yamagata, M., Meister, M. & Sanes, J. R. Molecular identification of a retinal cell type that responds to upward motion. *Nature* 452, 478–482 (2008).
- Zhang, Y. et al. Fast and sensitive GCaMP calcium indicators for imaging neural populations. Preprint at bioRxiv https://doi. org/10.1101/2021.11.08.467793 (2021).
- 35. Meyer, A. F., O'Keefe, J. & Poort, J. Two distinct types of eye-head coupling in freely moving mice. *Curr. Biol.* **30**, 2116–2130 (2020).
- 36. Barlow, H. B., Fitzhugh, R. & Kuffler, S. W. Change of organization in the receptive fields of the cat's retina during dark adaptation. *J. Physiol.* **137**, 338–354 (1957).
- 37. Farrow, K. et al. Ambient illumination toggles a neuronal circuit switch in the retina and visual perception at cone threshold. *Neuron* **78**, 325–338 (2013).
- Młynarski, W. F. & Hermundstad, A. M. Efficient and adaptive sensory codes. Nat. Neurosci. https://doi.org/10.1038/s41593-021-00846-0 (2021).
- 39. Laughlin, S. B. The role of sensory adaptation in the retina. J. Exp. Biol. 146, 39–62 (1989).
- 40. Joesch, M. & Meister, M. A neuronal circuit for colour vision based on rod-cone opponency. *Nature* **532**, 236–239 (2016).
- Baden, T. et al. A tale of two retinal domains: near-optimal sampling of achromatic contrasts in natural scenes through asymmetric photoreceptor distribution. *Neuron* 80, 1206–1217 (2013).
- Peichl, L., Künzle, H. & Vogel, P. Photoreceptor types and distributions in the retinae of insectivores. Vis. Neurosci. 17, 937–948 (2000).

- 43. Wallace, D. J. et al. Rats maintain an overhead binocular field at the expense of constant fusion. *Nature* **498**, 65–69 (2013).
- Rossi, L. F., Harris, K. D. & Carandini, M. Spatial connectivity matches direction selectivity in visual cortex. *Nature* 588, 648–652 (2020).
- Dräger, U. C. & Hubel, D. H. Responses to visual stimulation and relationship between visual, auditory, and somatosensory inputs in mouse superior colliculus. J. Neurophysiol. 38, 690–713 (1975).
- de Malmazet, D., Kühn, N. K. & Farrow, K. Retinotopic separation of nasal and temporal motion selectivity in the mouse superior colliculus. *Curr. Biol.* 28, 2961–2969 (2018).
- 47. Chen, H., Savier, E. L., DePiero, V. J. & Cang, J. Lack of evidence for stereotypical direction columns in the mouse superior colliculus. *J. Neurosci.* 41, 461–473 (2021).
- 48. Heukamp, A. S., Warwick, R. A. & Rivlin-Etzion, M. Topographic variations in retinal encoding of visual space. *Annu Rev. Vis. Sci.* **6**, 237–259 (2020).
- Szél, Á. et al. Different patterns of retinal cone topography in two genera of rodents, Mus and Apodemus. Cell Tissue Res. 276, 143–150 (1994).

50. Baden, T., Euler, T. & Berens, P. Understanding the retinal basis of vision across species. *Nat. Rev. Neurosci.* **21**, 5–20 (2020).

Publisher's note Springer Nature remains neutral with regard to jurisdictional claims in published maps and institutional affiliations.

Open Access This article is licensed under a Creative Commons Attribution 4.0 International License, which permits use, sharing, adaptation, distribution and reproduction in any medium or format, as long as you give appropriate credit to the original author(s) and the source, provide a link to the Creative Commons license, and indicate if changes were made. The images or other third party material in this article are included in the article's Creative Commons license, unless indicated otherwise in a credit line to the material. If material is not included in the article's Creative Commons license and your intended use is not permitted by statutory regulation or exceeds the permitted use, you will need to obtain permission directly from the copyright holder. To view a copy of this license, visit http://creativecommons.org/licenses/by/4.0/.

© The Author(s) 2023

Methods

Theory

We modeled neural responses r_t as a dot product of the model RF $\vec{\phi}$ and noisy stimulus vectors (image patches) $\vec{s}: rt = \phi \vec{T} st$, where T denotes vector transposition. RFs (filters) were optimized to minimize the following cost function:

$$L\left(\vec{\phi}\right) = \left\langle \sqrt{r_t^2} \right\rangle_t + \lambda \sum_{i=1}^N \phi_i^2 d(i)$$

Where d(i) is the squared distance between the i-th value of the RF and the one with the peak absolute value, and λ is the strength of the spatial locality constraint. This form of the locality constraint was introduced in ref. 11, and it has been demonstrated that it is consistent with RGC properties $^{11,13}.\,$ We note that the activity-related term in the cost function is equivalent to maximizing the sparsity of the neural activity quantified as the average absolute value of neural responses⁸. Without the spatial locality constraint (that is, $\lambda = 0$), the optimal RF is an oriented, Gabor-like filter. During optimization, to avoid convergence to trivial solutions, the norm of the RF $\vec{\phi}$ was constant and equal to 1. Overall, this cost function enforces minimization of activity conveyed downstream, while preserving the information about the image and meeting the locality constraints. Conceptually, this goal is equivalent to that of the PC model¹⁰. Our model generates predictions consistent with the PC model proposed in ref. 10 (Extended Data Fig. 1). It is, however, more flexible, and enables us to capture changes in the center size.

We modeled output of photoreceptor cells (stimuli s_t) as natural image patches distorted with the additive Gaussian noise with variance σ^2 that is: $s_{t,i} = x_{t,i} + \xi$, where $\xi \sim N(0, \sigma^2)$ is the noise term. To simulate different SNR conditions, we manipulated the noise variance level, and optimized RFs for each of the noise levels separately.

We optimized RFs by numerically minimizing the cost function L via gradient descent. For training, we used a dataset of 50,000 square image patches of 27 × 27 pixels in size taken from a dataset of natural images from the mouse visual environment¹⁸. We sampled images uniformly across the upper and lower visual fields. Each image patch was normalized to have a zero mean and unit variance. To simulate the impact of changing SNR, we normalized images with added noise. During optimization, the dimensionality of natural image data was reduced with principal-component analysis (PCA) to 128 dimensions. For each noise level, dimensionality reduction was performed using the same matrix of PCA components computed on noiseless data. To simulate the impact of changing SNR homogeneity, before normalization we multiplied the bottom half of each image by a scaling factor of less $than \, one, resulting \, in \, the \, range \, of \, vertical \, surround \, asymmetry \, values \,$ reported in Fig. 1h. After such scaling, we normalized the data and added noise of constant variance. During optimization of RFs on asymmetric stimuli, we computed PCA for each level of SNR asymmetry separately.

In all cases, before optimization, in order to enforce that the RF is centered in the image patch, we initialized RFs with random Gaussian noise with variance equal to 0.1 but set the central pixel value to -1. We independently optimized RFs using images taken in the UV and green parts of the spectrum, as well as in the 'joint' spectrum where intensity of each pixel was the average of green and UV values. To ensure that results do not depend on the choice of natural image dataset, we performed the simulations with the images of the African savanna from the van Hateren repository used in ref. 51 (Extended Data Fig. 2).

To evaluate RF properties, we defined the size of the RF to be the smallest circle that included 90% of energy (that is, ϕ_i^2) of optimal RFs averaged across all noise levels (Fig. 1b,c). Within that circle, we defined the center to be all $\vec{\phi}$ values smaller than 0, and the surround to be those larger than or equal to 0. The strength of the surround was thus equal to $\sum_{i:\phi_i>0}|\phi_i|$ and the center to $\sum_{i:\phi_i<0}|\phi_i|$. Sizes of the center were simply numbers of entries that were smaller than 0.

To characterize changes in contrast and luminance across the visual field, we used natural images published in ref. 18. We limited our $analysis \,to\,UV\,images\,only; however, light \,statistics\,of\,the\,green\,channel$ do not differ qualitatively. The images provided in ref. 18 were divided into two classes—upper visual field and lower visual field. To simulate the visual horizon, we concatenated pairs of images randomly selected from the upper and lower visual fields. We created a dataset of 1,000 such concatenated images and used them to compute the mean and variance of light intensity as estimates of local luminance and contrast, as well as to estimate the SNR as a function of elevation. To estimate the vertical asymmetry of the SNR pattern we used a square stimulus window, and a fixed noise variance. We note that key, qualitative aspects of our predictions do not depend on these choices. For each position y of the window along the vertical dimension of the visual field, we computed the vertical SNR asymmetry as: $\operatorname{asym}(y) = \frac{m_{\operatorname{up}}^y - m_{\operatorname{down}}^y}{m_{\operatorname{up}}^y + m_{\operatorname{down}}^y}$ where $m_{\rm up}^y$ and $m_{
m down}^y$ are sums of the SNR value within the stimulus window above and below its midline, respectively.

Animals

Mouse protocols were reviewed by the institutional preclinical core facility at IST Austria. All breeding and experimentation were performed under a license approved by the Austrian Federal Ministry of Science and Research in accordance with the Austrian and EU animal laws (BMF-66.018/0017-WF/V/3b/2017). For retinal experiments, triple-transgenic male and female mice (n=8 mice, 3 males, 5 females; n=11 retinas, 5 from the left eye, 6 from the right) aged 5–12 weeks were used for this study (Vglut2-ires-cre (JAX 28863), TITL-R-CaMP1.07-D (JAX 030217) and ROSA26-ZtTA (JAX 012266)). Original strains were obtained from Jackson Laboratories. For in vivo imaging experiments, C57BL/6J (JAX, 000664; n=3, 2 males, 1 female), aged 6–11 weeks at eye injection, were used. The mice were housed in a standard (in vivo inverted) 12-h day–night cycle and euthanized by cervical dislocation before in vitro imaging.

Statistics and reproducibility

No statistical method was used to predetermine sample size. Low SNR RFs were excluded from analysis, as described below. As done previously²⁰, only chirp responses that passed a quality criterion were used for further analysis. Given the nature of the retinal experiments, the location of the recordings was randomized to prevent any biases in the outcome.

Ex vivo imaging

The dark-adapted mouse retina was isolated under far-red light (LED peak 735 nm, additionally filtered with a 735-nm LP filter eliciting an isomerization rate of ~17 R s⁻¹) in oxygenated Ames' medium (Sigma) with constant bubbling (95% O₂, 5% CO₂) at room temperature. Left and right retinas were kept separate for identification. Four incisions were made to flat mount the retina, with ganglion cells facing up, on an 18-mm coverslip (VWR, 631-0153), and held down with a filter paper (Merck, GSWP01300) with a ~2.5 mm × 2.5 mm imaging window cut out. The preparation was then placed in a heated (32 °C) superfusion chamber on the stage of a custom-built upright fluorescence microscope. The retina was left to recover for a minimum of 10 min with the excitation light of the microscope turned on. An amber LED (Thorlabs, M595L4) filtered with a BP filter (Thorlabs, FB580-10) was used for excitation and a BP filter (Thorlabs, 641-75) in series with a 600-nm LP filter (Thorlabs, FEL0600) was used for collection. Background excitation light intensity was at a constant mean photopic intensity of $10^5 \,\mathrm{R}\,\mathrm{s}^{-1}$ per rod (at 585 ± 5 nm). Isomerization rates were determined using opsin templates⁵² and assuming that the mouse rod has an optical density at peak absorption wavelength of $0.015\,\mu\text{m}^{-1}$, a length of $24\,\mu\text{m}$, a diameter of 1.4 µm and a quantum efficiency of 0.67 (refs. 53,54). Each retina was tiled by recording 3-7 different FOVs at ×10 magnification

(Olympus XLUMPLFLN20XW objective) using a sCMOS camera (Photometrics Prime 95B) at 10 frames per second and 1.1-µm pixel resolution. Setup was controlled and data were acquired using custom-built LabVIEW software (National Instruments, version 2019).

Visual stimuli for retinal experiments

Light stimuli were delivered from a modified Texas Instruments DLPL-CR4500EVM DLP projector through a custom-made lens system and focused onto the photoreceptors (frame rate of 60 Hz, magnification of 2.5 µm per pixel, total area of 3.2 mm × 2 mm). The projector's blue LED was replaced with a high-power UV LED (ProLight 1 W UV LED, peak 405 nm), to improve the differential stimulation of S pigments. Two SP filters in series (Thorlabs, FESH0550) were put in the stimulus path to block green light from entering the camera. Intensities and spectra were measured using a calibrated spectrometer (Thorlabs, CCS-100) and a digital power meter (Thorlabs, S130C sensor). A shifting spatiotemporal white-noise stimulus was presented using a binary pseudorandom sequence, in which the two primary lights (green and UV) varied dependently. All white-noise stimuli were presented at a 6-Hz update for 15 min. The checker size was $100 \times 100 \,\mu m$ and the entire grid was shifted by random multiples of 10 µm in both x axis and y axis after every frame. In comparison experiments, static checkers (without shifts) of $100 \times 100 \,\mu\text{m}$ and $25 \times 25 \,\mu\text{m}$ were interleaved with the shifting checkers in chunks of 5 min for a total of 20 min for each of the three checker types. A 'chirp' stimulus with a 1-s bright step, increasing amplitude (0 to 127 over 8 s) and increasing frequency (0 to 4 Hz over 8 s) was repeated for five trials to reproduce clustering of responses²⁰. Moving square gratings (temporal frequency of 0.6 cycles per second and spatial frequency of 0.025 cycles per micron) or a wide bright bar (1 mm s⁻¹ speed, 2 mm width) in eight directions, repeated for five trials, were used for assessing direction selectivity. All visual stimuli were generated using the Psychtoolbox (version 3)55.

Histology

After the ex vivo recordings, some of the retinas were fixed with 4% paraformaldehyde (PFA) for 30 min and stained for S-opsin and RFP. Retinas were incubated for 7 d at 4 °C in PBS, containing 5% donkey serum, 0.5% Triton X-100, goat anti S-opsin (1:500 dilution; Rockland, $600\text{-}101\text{-}MP7) and rabbit anti-RFP (1:1,000 \, dilution; Rockland, 600\text{-}401\text{-}$ 379). After washing thrice in PBS for 15 min each, retinas were incubated overnight in secondary antibodies, donkey anti-goat Alexa Fluor 488 (1:1,000 dilution; Abcam, ab150129) and donkey anti-rabbit Alexa Fluor 594 (1:1,000 dilution; Invitrogen, R37119). Retinas were then mounted and imaged with an Olympus VS120 Slidescanner with a ×20 objective. For cell-type characterization, Vglut2-ires-cre; TITL-R-CaMP1.07-D; ROSA26-ZtTA mice were euthanized and perfused intracardially, followed by retina extraction and staining for RBMPS or SMI32, along with RFP (primary antibodies: guinea pig anti-RBPMS (1:500 dilution; Sigma, ABN1376), mouse anti-SMI32 (1:500 dilution; BioLegend, 801701), rabbit anti-RFP (1:1,000 dilution; Rockland, 600-401-379) or mouse anti-RFP (1:500 dilution; MBL, M155-3); secondary antibodies: goat anti-guinea pig Alexa Fluor 647 (1:1,000 dilution; Invitrogen, A21450), donkey anti-mouse Alexa Fluor 647 (1:1,000 dilution; Abcam, A-31571) and donkey anti-rabbit Alexa Fluor 594 (1:1,000 dilution; Invitrogen, R37119). The staining protocol was the same as above and these retinas were imaged with a Leica SP8 confocal microscope.

After the final in vivo recording, mice were terminally anesthetized with ketamine/xylazine (100 mg per kg body weight/10 mg per kg body weight) intraperitoneally (i.p.) and transcardially perfused with PBS, followed by 4% PFA. Brains were extracted and post-fixed in 4% PFA at 4 °C overnight. Brains were then washed and transferred to 30% sucrose solution for cryoprotection overnight at 4 °C and subsequently frozen and the midbrain coronally sliced into 40- μ m sections on a Leica SM2010R sliding microtome. Sections were washed and then incubated in PBS, containing 5% donkey serum, 0.3% Triton X-100 and

goat anti-GFP (1:2,000 dilution; Abcam, ab6673) overnight at 4 °C. After washing thrice in PBS for 15 min each, brain sections were incubated for 1 h in secondary antibody solution, donkey anti-goat Alexa Fluor 488 (1:1,000 dilution; Abcam, ab150129), washed thrice again in PBS and mounted on slides, where they were stained with DAPI (not shown) and coverslipped with custom-made Mowiol. Brain sections were imaged with a Nikon CSU-W1 spinning disk confocal microscope at $\times 20$ tile stack acquisition. Shading correction was performed on image stacks with BaSiC 56 in ImageJ and, finally, maximum projection was performed over the whole stack.

Preprocessing

Regions of interest (ROIs) were detected automatically from raw calcium movies using Suite2p⁵⁴. Fluorescence traces, F, were detrended by computing dF/F, where the 8th percentile in a 20-s sliding window centered around each time point was taken as the baseline fluorescence. Different FOVs from the same retina were stitched together based on coordinates from the stage motors and repeated ROIs in overlapping regions were manually annotated using an open-source tool⁵⁷. Repeated ROIs with the highest score in Suite2p's built-in classifier were kept for analysis. The deconvolved signal from Suite2p (with tau = 1.0 s) was used for calculating RFs.

The median d*F/F* response across trials was taken as the response to the chirp and normalized by dividing by the maximum of the absolute values across time. Quality Index was computed as in ref. 20 , and only responses with a score > 0.45 were kept for clustering (8,019 of 30,798 neurons). For moving gratings and bar, the mean across trials and maximum across time was taken as the response in any one direction.

Receptive field mapping

The RF for each neuron was computed as a calcium-triggered average. The spatiotemporal RF at latency τ , position (x,y) for neuron i was computed as

$$\mathsf{RF}\left(i, x, y, \tau\right) = \sum_{t=1}^{T} s\left(x, y, t - \tau\right) \cdot r\left(i, t\right) - \sum_{t=1}^{T} s(x, y, t - \tau) \cdot \sum_{j=1}^{N} r(j, t),$$

where r(i,t) is the deconvolved response of neuron i at time t, s(x,y,t)) is the white-noise stimulus, T is the length of the recording and N is the total number of neurons in the recording. The second term in this equation subtracts away the residual distribution of the stimulus and the contribution of slow bleaching that is common to all neurons in that recording and leads to RFs that had noticeably less noise. Only the UV channel of the stimulus was used for RF mapping. The latency τ was varied in increments of $0.025 \, \mathrm{s}$ (40 Hz), and the stimulus was interpolated by using the last frame before a particular time, t- τ . The RF for each neuron was normalized between -1 and 1 by subtracting the mean value of the RF at latencies $\tau < 0$, and dividing by the maximum absolute value of the entire RF.

The location of the center of an RF was estimated by finding the pixel that varied the most across time, $P_{var} = argmax\ Var^t(x,y)$ where $Var^t(x,y)$ is the variance across time for position (x,y). Each neuron's RF was cropped within a square window of edge 1 mm centered on this pixel. The SNR of an RF was computed as the peak-to-noise ratio where the power of noise was estimated in regions with distance >0.5 mm from the point P_{var} . Only RFs with a peak SNR > 15 dB were kept for analysis (31,135 selected RFs of 37,086 recorded neurons). The location of the RF in time was found in a similar way; $T_{var} = argmax\ Var^{xy}(t)$ here, $Var^{xy}(t)$ is the variance in space.

Parametrization of receptive fields

We parametrized spatiotemporal properties of the center and surround of the RFs as a sum of two 2D Gaussian distributions (Gaussians) $G_1 + G_2$. The first Gaussian represents the center of the RF; its amplitude can be

either negative or positive corresponding to an OFF or an ON cell. The amplitude of the second Gaussian is required to be of the opposite sign to model the properties of the surround. We computed a spatial representation of the RF, denoted as RF_{2D} as the median of the RF within a small time window around $T_{\rm var}$. To reduce noise, we excluded the pixels that were weakly correlated with $P_{\rm var}$ across time. The sum of 2D Gaussians G_1+G_2 was then fitted to RF_{2D}. Each Gaussian is defined by the amplitude A, center (m^x,m^y) , width (σ^x,σ^y) and the orientation angle θ . We fit only one Gaussian G_1 to parametrize the location (m^x,m^y) , the size and the orientation θ_1 of the center. In the next step, we fit the sum of Gaussians, where we fixed $(m^x,m^y,\sigma^{x0},\sigma^{y0},\theta_1)$ parameters of G_1 while allowing all other parameters to be fitted anew.

Here we differentiated two types of RFs: a RF with a strong center and a weaker surround that largely overlap, and a RF where both center and surround components are strong and well separated. For the first case, we imposed a constraint such that the center of G₂ is within the distance $d = 2 \min (\sigma_1^{x_0}, \sigma_1^{y_0})$ from the center (m_1^x, m_1^y) . We implemented this constraint as a penalty sigmoid function $P(\text{dist}(G_1, G_2))$ of the distance between the locations of the center and surround components. We added $P(\text{dist}(G_1, G_2))$ to the Gaussian mixture and allowed it to be prohibitively large for $dist(G_1, G_2) > d$. Encoding the constraint in this manner allowed us to remove the bias for the location of the surround on the diagonals of the RF_{2D}, which otherwise happens when fitting Gaussian mixture on the square bound-constrained region. There were no constraints for the second type of the RFs where the surround component is strong and more distant from the center. To decide the type of the RF, we found the maximum and minimum points of the RF, and we computed the distance between them and the ratio of their absolute values. If the ratio of the smaller to the bigger values was less than 0.75 or if the distance between the extrema points was less than d, then we classified such an RF as the first type, and as the second type otherwise. Experimentally, we found that imposing such a constraint on the location of the second Gaussian leads to a better fitted sum of Gaussians for RFs with largely overlapping center and surround components. All the fitting procedures were implemented using the nonlinear least-squares solver lsqcurvefit in MATLAB.

Using parametrization, we computed various RF characteristics. We found two sets of pixels corresponding to the center and the surround. Center pixels are the pixels within two standard deviations from the center of the G_1 . Surround pixels are the pixels within two standard deviations from the center of the G_2 and that are not center pixels. The center size is the number of pixels in the center set, converted to mm² for display. The relative surround strength is the ratio of the absolute value of sum of surround pixels to the absolute value of sum of center pixels. Vertical surround asymmetry is defined as (u-l)/(u+l) where u and l denote the absolute value of sum of pixels in the upper and lower halves of the surround pixels, respectively. The distance between the center and the surround is the distance between the center of mass (COM) of the center pixels and the COM of the surround pixels. The orientation is the angle between the hori $zontal\,ax is\,and\,the\,line\,connecting\,the\,two\,COMs.\,Radial\,profiles\,were$ computed as the average values of the pixels in RF_{2D} within rings of increasing radii centered on the point P_{var} . The average value of the center or surround pixels across time was taken to be the RF center or surround temporal dynamics, respectively. The R^2 goodness of fit was computed as

$$R^{2} = 1 - \frac{\sum_{i} (RF_{2D_{i}} - M_{i})^{2}}{\sum_{i} (RF_{2D_{i}} - \overline{RF}_{2D})^{2}},$$

where $M = G_1 + G_2$ is the RF parametrization. The values of the above RF parameters are reported for a few representative neurons in Extended Data Fig. 4.

Retina alignment

All functional imaging experiments were performed with randomized retina orientations. For retinas that were co-stained against S-opsin and RCaMP1.07 (n=6 retinas), the direction with the highest density of S-opsin was taken to be the ventral direction⁵⁸. The stitched maximal projection images of the functional imaging experiments were aligned to the RCaMP channel using the retinal vasculature. In each of these retinas, we observed that a streak of asymmetric surrounds was always consistently present across the dorsal retina. Thus, we assumed this to be a reproducible feature, which we then used to manually align the remaining n=5 retinas that did not have an S-opsin staining (and hence no ground truth orientation). To avoid any potential circular arguments, we present the location of neurons from these five retinas only in Extended Data Fig. 7, with a clear indication that the retinal orientation is presumed.

The coordinates of cells from each retina were then translated to make the optic nerve the zero of the coordinate system and rotated such that the positive y axis denoted ventral direction. Left retinas were flipped in the nasotemporal axis such that the positive x axis denoted nasal direction for all retinas. All spatial RFs were also translated and rotated accordingly. The cartesian retinal coordinates of cells in the stained retinas were converted to spherical visual coordinates using the R package Retistruct, assuming the optical axis of the mouse eye to be oriented at an azimuth of 64° and an elevation of 22° from the long axis of the animal³¹.

Binning of receptive field properties

For 2D bins, the retinal space from $-1,500~\mu m$ to $1,500~\mu m$ in both nasotemporal and dorsoventral axes was divided into a square grid and all neurons within each bin were collected. Only 2D bins with at least five neurons were analyzed to minimize sampling bias. The spatial RF values of all neurons within each bin of 300 μm in size were averaged and plotted at the location of the bin in Fig. 3a and Extended Data Fig. 6. The RF parameter values of neurons within each bin of size 50 μm were averaged to yield a 2D map of the parameter, and this map was visualized (without smoothing) in Fig. 3d–h. Owing to its area-preserving property, the sinusoidal projection of visual space was binned in the same way as the retinal surface, and the fraction of cells in each bin that had ventrally oriented surrounds were plotted in Fig. 3k.

For 1D analysis, the bins were defined along the dorsoventral or nasotemporal axis based on the range of coordinates in a particular group (by retina (Fig. 3) or cluster (Fig. 4)). The range was divided into six equally spaced bins and the mean parameter value of neurons within each bin was plotted at the coordinate of the center of the bin. As a summary statistic, two-sample Kolmogorov–Smirnov-tests were performed between ventral and dorsal samples of these binned values (n = 56 (Fig. 3) and n = 60 (Fig. 4) samples). Two-sample Kolmogorov–Smirnov tests (with Bonferroni correction for multiple comparisons) were also performed between raw values of RF parameters for Extended Data Fig. 6. In addition, the weights of linear regressions of RF parameters in elevation (dorsoventral) and azimuth (nasotemporal) orientations are reported.

Clustering into functional types

The GMM procedure developed in ref. 20 was used for clustering temporal RFs and chirp responses, separately. In brief, after normalization, the trace was first reduced in dimension using PCA (10 components for temporal RFs and 20 components for chirp responses) and then GMM models with diagonal covariance matrices were fitted while increasing the number of clusters. The numbers of clusters were identified to be 10 for temporal RFs and 20 for chirp responses based on elbow points in the respective Bayesian information criteria curves. One chirp cluster (n = 68 cells) lacked stimulus-evoked responses and was discarded on visual inspection. To assess the degree of overlap between the RFs of neurons belonging to each of the clusters, we defined the tiling index

(TI) of the cluster *K* as the area of the union of all RF centers in a cluster, divided by the sum of their individual areas:

$$\mathsf{TI}_K = \frac{\mathsf{Area}(\cup_{i \in K} \mathsf{RF}_i)}{\sum_{i \in K} \mathsf{Area}(\mathsf{RF}_i)}$$

The value of this index for each cluster was computed separately for each retina and the mean and s.d. across retinas are reported in Supplementary Table 1.

Viral eye injections

For viral-mediated gene transfer, 6- to 11-week-old wild-type C57BL/6J mice (JAX, 000664) were anesthetized with ketamine/xylazine by i.p. injection. A 1/2-inch, 30-gauge needle was used to make a small hole in the temporal eye, below the cornea. Then, 1 μ l of vitreous fluid was withdrawn and 1 μ l of AAV2.7M8-syn-GCaMP8m viral vector solution (at a titer of ~1 \times 10 13 genome copies per ml, ISTA viral facility) was injected into the subretinal space with a Hamilton syringe and a 33-gauge blunt-ended needle.

Mouse surgery for in vivo imaging

Two to three weeks after viral eye injections, mice were injected with meloxicam (20 mg per kg body weight, subcutaneous (s.c.), 3.125 mg ml⁻¹ solution) and dexamethasone (0.2 mg per kg body weight i.p., 0.02 mg ml⁻¹ solution). Anesthesia was induced by 2.5% isoflurane in oxygen in an anesthesia chamber. The mouse was subsequently fixed in a stereotaxic device (Kopf) with a constant isoflurane supply at 0.7% to 1.2% in O₂ and body temperature controlled by a heating pad to 37.5 °C. After the assertion that reflexes subsided, the cranium was exposed and cleaned of periosteum and connective tissue. A circular craniotomy of 4 mm in diameter was drilled above the left SC and from this point onwards, the exposed brain was constantly irrigated with artificial cerebrospinal fluid. The exposed dura mater was removed, and subsequently, the left transverse sinus was sutured twice with 9-0 monofil surgical suture material (B. Braun) and cut between the sutures. Cortical areas covering the left SC were aspirated with a cell culture vacuum pump (Accuris) connected to a blunt needle of 0.5 mm in diameter. A 3-mm circular coverslip was glued (Norland optical adhesives 61) to a thin-walled custom-made conical ring, made from stainless steel. The coverslip ring was inserted into the cavity left by the aspirated cortex, so that the glass was sitting flush on the surface of the SC. Slight pressure was applied with the help of a thinned toothpick, fixed to the stereotaxic arm. The space around the insert was filled with Dura-Gel (Cambridge Neurotech) and the insert was fixed in place with VetBond (3M). After cleaning and drying the surrounding cranium, a multilayer of glues was applied. First, to provide adhesion to the bone, All-in-One Optibond (Kerr) was applied and hardened by blue light (B.A. Optima 10). Second, Charisma Flow (Kulzer) was applied to cover the exposed bone and fix the metal ring in place by also applying blue light. After removal of the fixation toothpick, a custom-designed and manufactured (RPD) headplate, selective laser-sintered from the medical alloy TiAl6V4 (containing a small bath chamber and micro-ridges for repeatable fixation in the setup), was positioned in place and glued to the Charisma on the cranium with Paladur (Kulzer). Mice were given 300 µl of saline and 20 mg per kg body weight meloxicam (s.c.), before removing them from the stereotaxic frame and letting them wake up while keeping them warm on a heating pad. Another dose of 20 mg per kg body weight meloxicam s.c. and 0.2 mg per kg body weight i.p. dexamethasone was further injected 24 h after conclusion of the surgery. After the implantation surgery, animals were allowed to recover for 1 week.

In vivo visual stimulation and eye movements

Mice were head-fixed while awake using a custom-manufactured clamp, connected to a three-axis motorized stage (8MT167-25LS, Standa). Mice could run freely on a custom-designed spherical treadmill (20-cm

diameter). Visual stimuli were projected by a modified LightCrafter (Texas Instruments) at 60 Hz, reflected by a quarter-sphere mirror (Modulor) below the mouse and presented on a custom-made spherical dome (80 cm in diameter) with the mouse's head at its center. The green and blue LEDs in the projector were replaced by cyan (LZ1-00DB00-0100, Osram) and UV (LZ1-00UB00-01U6, Osram) LEDs respectively. A double bandpass filter (387/480 HD Dualband Filter, Semrock) was positioned in front of the projector to not contaminate the imaging. The reflected red channel of the projector was captured by a transimpedance photo-amplifier (PDA36A2, Thorlabs) and digitized for synchronization. Cyan and UV LED powers were adjusted so that the reflectance on the screen matched the relative excitation of M-cones and S-cones during an overcast day, determined and calibrated using opsin templates⁵² and a spectrometer (CCS-100, Thorlabs). Stimuli were designed and presented with Psychtoolbox (version 3)55, running on MATLAB 2020b (MathWorks). Stimulus frames were morphed on the GPU using a customized projection map and an OpenGL shader to counteract the distortions resulting from the spherical mirror and dome. The dome setup allows the presentation of mesopic stimuli from circa 100° on the left to circa 135° on the right in azimuth and from circa 50° below to circa 50° above the equator in elevation.

Visual stimuli were like ex vivo retinal imaging experiments: A shifting spatiotemporal white-noise stimulus was presented using a binary pseudorandom sequence, in which the two primary lights (cyan and UV) varied dependently. All pseudo white-noise stimuli were presented at a 5-Hz update in 5-min episodes, interleaved with different stimuli (for example, gray screen, moving gratings (not shown)) with a total pseudo white-noise duration of 15–60 min (median of 25 min) per recording. The checker size was a visual angle of $8\times8^\circ$ and the entire grid was shifted by random multiples of a 0.4° visual angle in both elevation and azimuth axis after every frame. Eye movements of the right eye were recorded with a camera (Basler acA1920-150um, 18–108 mm macro zoom lens (MVL7000, ThorLabs), set at 100 mm, and infrared illumination of 830 nm) via an infrared mirror at 50 frames per second.

In vivo retinal terminal imaging

Two-photon axonal terminal imaging was performed on a custom-built microscope, controlled by ScanImage (Vidrio Technologies) running on MATLAB 2020b (MathWorks) and a PXI system (National Instruments). The beam from a pulsed Ti:Sapphire laser (Mai-Tai DeepSee, Spectra-Physics) was scanned by a galvanometric-resonant (8 kHz) mirror combination (Cambridge Scientific) and expanded to underfill the back-aperture of the objective (×16 0.8-NA water-immersion, Nikon); 1.9 × 1.9-mm FOV; 30-Hz frame rates. Fast volumetric imaging was $acquired\ with\ a\ piezo\ actuator\ (P-725.4CA, Physik\ Instrumente).\ Emit-noise actuator\ (P-725.4CA, Physik\ Instrumente).$ ted light was collected (FF775-Di01, Semrock), split (580 nm long-pass, FF580-FDi01, Semrock), bandpass filtered (green, FF03-525/50; red, FF01-641/75; Semrock), measured (GaAsP photomultiplier tubes, H10770B-40, Hamamatsu), amplified (TIA60, Thorlabs) and digitized (PXIe-7961R NI FlexRIO FPGA, NI 5734 16-bit, National Instruments). The laser wavelength was set between 920 and 950 nm. Average laser output power at the objective ranged from 57 to 101 mW (median of 69 mW)⁵⁶. A FOV of 0.32–1.85 mm² (median of 0.68 mm²) was imaged over 3-7 planes (median of 6 planes) with a plane distance of 14-40 µm (median of 25 μm) at a pixel size of 0.6–1.9 μm (median of 1.3 μm) and a volume rate of 4.3–9.5 Hz (median of 5.0 Hz). Each mouse was recorded in 2–4 imaging sessions on different days. In a subset of mice (n = 2) in separate imaging sessions, absence of substantial z-motion was verified by injecting 40 μl of Texas Red dextran (3000 MW, X 14.3 mg ml⁻¹, diluted in saline, Themo Fisher Scientific) s.c. and imaging brightly red labeled blood vessels at 980 nm⁵⁹.

In vivo eye movement analysis

Behavior videos were analyzed with DeepLabCut⁶⁰, labeling eight points around the pupil. The eight points were then fitted to an ellipse

and the ellipse center position transformed to rotational coordinates under the assumption of eyeball radius = $1.5\,\mathrm{mm^{61}}$, using custom Python scripts. The median of all eye positions was set to zero azimuth and elevation, that is, all eye coordinates were relative to the median position. The individual horizontal axis, which varied slightly between mice due to differences in the positioning of the head plate, was corrected by leveraging a behavioral feature of head-fixed mice: Saccadic movements are nearly exclusively in one plane 35 . Saccades were extracted by determining events of fast position changes on a median filtered position trace (median filter window of $0.7\,\mathrm{s}$, minimal saccadic speed of 45° per second, minimal saccade amplitude of 3° , minimal saccade interval of $0.25\,\mathrm{s}$). The preferred saccadic orientation and orientation tuning was determined in a similar fashion as that for neuronal visual orientation tuning based on circular variance:

$$\bar{\alpha} = \frac{1}{2} arg \left[\sum_{t} r_{t} \exp(2i\alpha_{t}) \right]$$

$$\bar{r} = \frac{1}{\sum_{t} r_{t}} \left| \sum_{t} r_{t} \exp(2i\alpha_{t}) \right|$$

with $\bar{\alpha}$ as the saccadic orientation angle, \bar{r} as saccadic orientation tuning, r_t as saccade amplitude and α_t as direction of saccade t (Extended Data Fig. 9a–c). Saccade orientation tuning was very high, with mean selectivity = 0.8.

In vivo axonal terminal analysis

Functional calcium imaging data were first analyzed with suite2p (v0.10.0)⁶² for motion correction and ROI extraction. ROIs were then curated manually based on morphological and activity shape. Further analysis was performed in custom MATLAB R2021a (MathWorks) scripts: dF/F_0 was estimated based on published procedures⁶³ by first subtracting neuropil contamination (from suite2p, fluorescence signal of 350 pixels surrounding the ROI, excluding other ROIs) with a factor of 0.5 (estimated from fluorescence of small capillaries as reported previously). From the neuropil-corrected ROI fluorescence, baseline F_0 was defined as the 8th percentile of a moving window of 15 s⁶⁴. dF/F_0 was then calculated by first subtracting and then dividing the fluorescence trace by the median of the same 15-s window⁶³. Fluorescence SNR was defined for each neuron by dividing the 99th percentile of the dF/F trace ('signal') by the standard deviation of its negative values after baseline correction ('noise'). Only axonal segments with a fluorescence $SNR \ge 5$ were included in further analysis. The deconvolved signal from Suite2p (with tau = 0.7 s) was used for calculating RFs. Note that multiple axonal ROIs can originate from the same RGC. Spatiotemporal RF analysis for in vivo retinal terminals was conducted as for ex vivo RGC imaging, but on visual stimuli downsampled to a resolution of a 1° visual angle. The resulting $50 \times 50^{\circ}$ RFs were contaminated by eye movements and exhibited a lower SNR (as determined by temporal variance of the most $varying\ pixel\ over\ the\ temporal\ variance\ of\ pixels\ with\ >50^{\circ}\ visual\ angle$ distance) than ex vivo soma recordings, requiring further inclusion criteria: SNR > 15 (as in ex vivo data) and peak variance over time located at tau values between -0.1 and 0.6 s. Additionally, the retinotopic projection pattern of RGCs to the SC was utilized by fitting a map from visual coordinates to collicular space. For each recording, RF center azimuth and elevation values were fitted separately to the location of the ROI in the SC using the 'poly22' fit option in MATLAB and using only the highest 15% ROIs in SNR and SNR as a fitting weight. Boutons with peak location of the RF deviating by more than a 20° visual angle from its expected location based on the retinotopy fits were removed from further analysis (828 boutons removed).

The main saccadic axis was used to rotate the computed spatial RFs around their respective center and the center positions in visual space as spherical rotation around the approximate eye axis (65° from

frontal direction in the horizontal plane). Finally, while freely moving mice hold their head at an approximate pitch angle of 30° downwards for vivo imaging allowed only for a pitch angle of 10° downwards. To compensate, the center positions of all RFs were spherically rotated 20° downwards around the main pitch axis (90° from frontal direction in horizontal plane). Note that these calculations only allow an estimate of the position of the horizon in free locomotion.

To avoid biasing the analyses by eye movements, RF parametrization was conducted on mean vertical 1D profiles of extracted $50 \times 50^\circ$ 2D RF crops at the peak azimuthal position $\pm 1^\circ$, where ON center bouton RFs were inverted. To extract parameters from 1D RFs, they were fitted with a difference of two Gaussians, initialized with the central peak magnitude (Mpeak) and width (Wpeak). The fitting procedure was then constrained with amplitude center $\in [M_{peak}/2, \inf]$, amplitude surround $\in [0,\inf]$, location center $\in [-20,20]^\circ$, location surround $\in [-25,25]^\circ$ (edge of crop), sigma center $\in [W_{peak}/4,\inf]$ and sigma surround $\in [W_{peak},\inf]$. Boutons with a center fit location in 1D RFs of more than 5° or with a surround fit location of more than 25° distant from peak estimation based on variance in 2D RFs, were excluded from further analysis (1,609 boutons removed). Extraction of parameters was identical to ex vivo RF parametrization, except center size, where in vivo 2sigma_{center} of the fit was used.

For presenting RF characteristics of RGC axonal boutons in the SC, the centered 1D RFs were binned and averaged in each bin. RF parameters varying over elevation and azimuth are presented as parameters of the fit on the mean 1D RF in the respective bin. Linear regression weights were computed from the parameters and location of each individual bouton.

Reporting summary

Further information on research design is available in the Nature Portfolio Reporting Summary linked to this article.

Data availability

Data used in the analysis can be found at ISTA data repository: https://doi.org/10.15479/AT:ISTA:12370.

Code availability

 $Code \, used \, to \, generate \, the \, results \, is \, available \, at \, GitHub: \, https://github. \, com/joesch-lab/panoramic-retina/.$

References

- Cadieu, C. F. & Olshausen, B. A. Learning intermediate-level representations of form and motion from natural movies. *Neural Comput.* 24, 827–866 (2012).
- 52. Govardovskii, V. I., Fyhrquist, N., Reuter, T., Kuzmin, D. G. & Donner, K. In search of the visual pigment template. *Vis. Neurosci.* **17**, 509–528 (2000).
- Carter-Dawson, L. D. & LaVail, M. M. Rods and cones in the mouse retina. I. Structural analysis using light and electron microscopy. J. Comp. Neurol. 188, 245–262 (1979).
- 54. Penn, J. S. & Williams, T. P. A new microspectrophotometric method for measuring absorbance of rat photoreceptors. *Vis. Res.* **24**, 1673–1676 (1984).
- Brainard, D. H. The psychophysics toolbox. Spat. Vis. 10, 433–436 (1997).
- Peng, T. et al. A BaSiC tool for background and shading correction of optical microscopy images. *Nat. Commun.* 8, 14836 (2017).
- GitHub. ROIMatchPub: Match suite2p ROIs between imaging sessions. https://github.com/ransona/ROIMatchPub
- Sondereker, K. B., Stabio, M. E., Jamil, J. R., Tarchick, M. J. & Renna, J. M. Where you cut matters: a dissection and analysis guide for the spatial orientation of the mouse retina from ocular landmarks. J. Vis. Exp. https://doi.org/10.3791/57861 (2018).

- Ryan, T. M., Hinojosa, A. J., Vroman, R., Papasavvas, C. & Lagnado, L. Correction of z-motion artefacts to allow population imaging of synaptic activity in behaving mice. J. Physiol. 598, 1809–1827 (2020).
- Mathis, A. et al. DeepLabCut: markerless pose estimation of user-defined body parts with deep learning. *Nat. Neurosci.* 21, 1281–1289 (2018).
- Hammel, B. & Sullivan-Molina, N. bdhammel/ least-squares-ellipse-fitting: v2.0.0. Zenodo (2020).
- Pachitariu, M. et al. Suite2p: beyond 10,000 neurons with standard two-photon microscopy. Preprint at *bioRxiv* https://doi.org/10.1101/061507 (2017).
- Keller, G. B., Bonhoeffer, T. & Hübener, M. Sensorimotor mismatch signals in primary visual cortex of the behaving mouse. *Neuron* https://doi.org/10.1016/j.neuron.2012.03.040 (2012).
- Dombeck, D. A., Khabbaz, A. N., Collman, F., Adelman, T. L. & Tank, D. W. Imaging large-scale neural activity with cellular resolution in awake, mobile mice. *Neuron* 56, 43–57 (2007).
- Stabio, M. E. et al. A novel map of the mouse eye for orienting retinal topography in anatomical space. J. Comp. Neurol. 526, 1749–1759 (2018).

Acknowledgements

We thank H. Asari for sharing the dataset of naturalistic images, Y. B. Simon for initial explorative work with the generation of AAVs, R. Beattie for the custom retina and T. Vega-Zuñiga for help with immunostainings. We also thank G. Tkačik and members of the Neuroethology group for their comments on the manuscript. This research was supported by the Scientific Service Units of IST Austria through resources provided by Scientific Computing, MIBA Machine Shop, the Preclinical Facility, the Lab Support Facility and the Imaging and Optics Facility. This work was supported by European Union Horizon 2020 Marie Skłodowska-Curie grant 665385 (to D.G.), Austrian Science Fund (FWF) stand-alone grant P 34015 (to W.M.), Human

Frontiers Science Program LT000256/2018-L (to A.S.), EMBO ALTF 1098-2017 (to A.S.) and the European Research Council Starting Grant 756502 (to M.J.).

Author contributions

D.G., W.M. and M.J. designed the study. D.G. and J.S. performed the retina imaging experiments with help from M.J. D.G. and M.J. developed the retinal imaging system. J.S. and M.J. developed the shifting stimuli. A.S. performed the in vivo imaging experiments and developed the imaging system with help from M.J. D.G., A.S. and O.S. analyzed the experimental data with inputs from W.M. and M.J. W.M. analyzed natural scene statistics and developed the normative model. D.G., W.M. and M.J. wrote the manuscript with help of the other authors.

Competing interests

The authors declare no competing interests.

Additional information

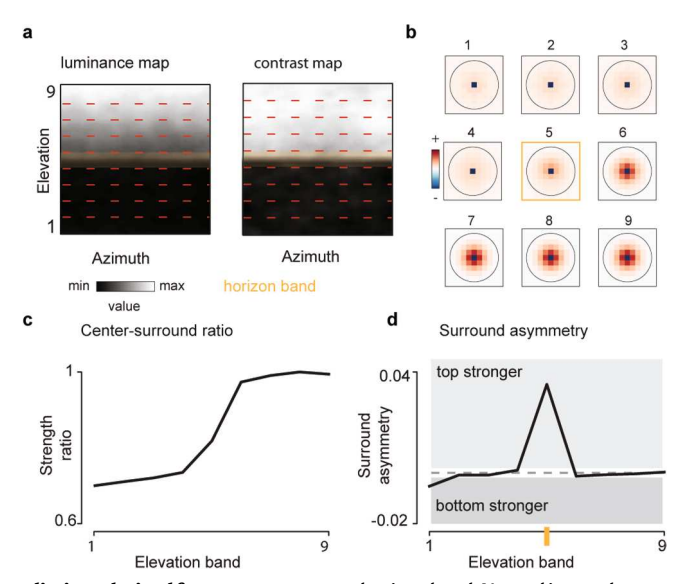
Extended data is available for this paper at https://doi.org/10.1038/s41593-023-01280-0.

Supplementary information The online version contains supplementary material available at https://doi.org/10.1038/s41593-023-01280-0.

Correspondence and requests for materials should be addressed to Maximilian Joesch.

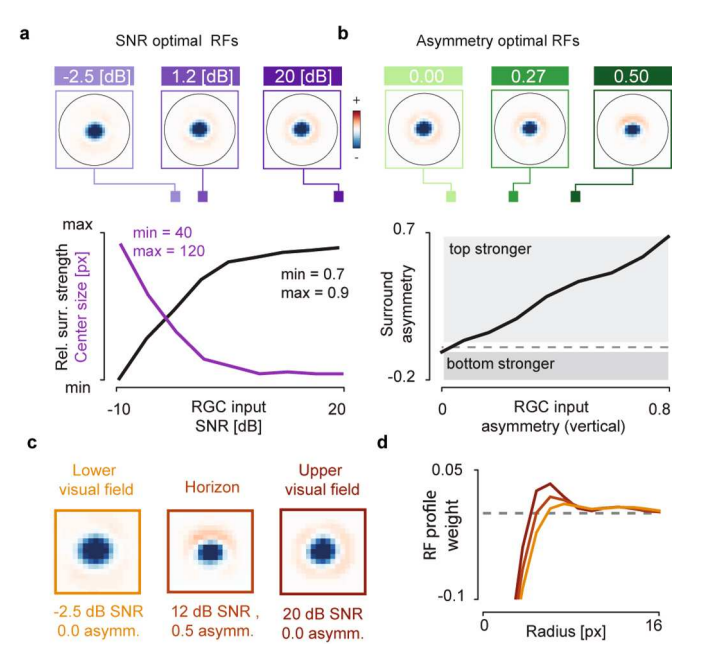
Peer review information *Nature Neuroscience* thanks Philipp Berens, Olivier Marre and Stephanie Palmer for their contribution to the peer review of this work.

Reprints and permissions information is available at www.nature.com/reprints.



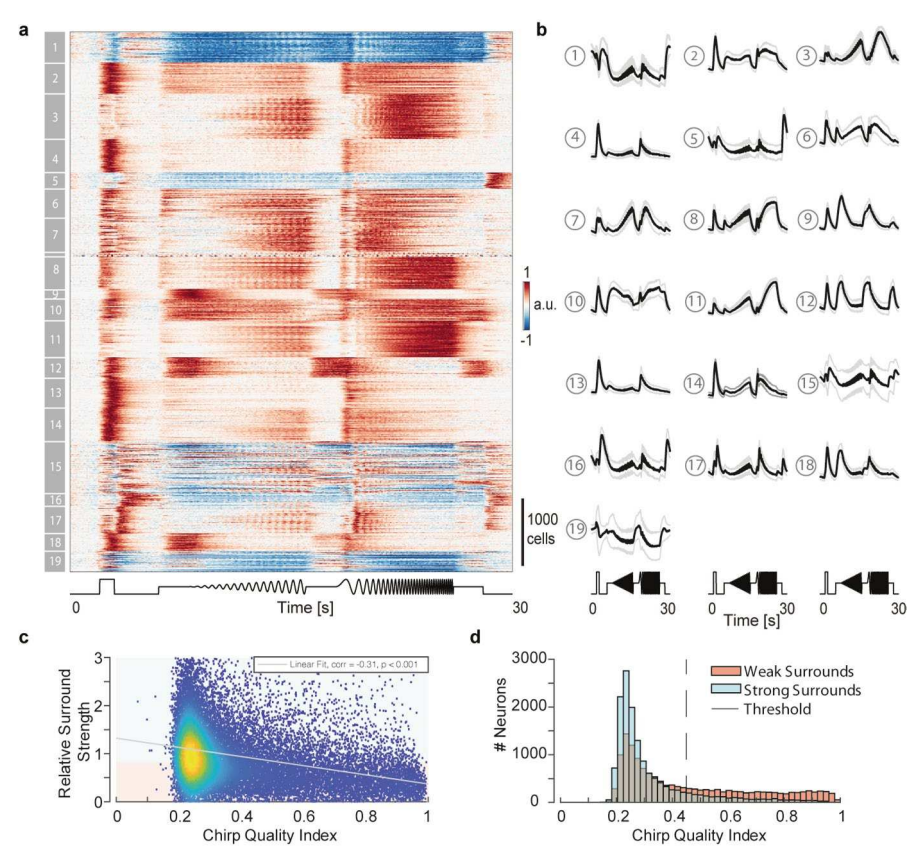
Extended Data Fig. 1 | **Predictive coding predictions derived from a previously proposed model. (a)** Average luminance (left panel) and local contrasts (right panel) in the mouse field of view in the ultraviolet range. Red dashed lines separate elevation bands. Orange opaque rectangle denotes the

horizon band. Natural image data - courtesy of Hiroki Asari¹⁸. (**b**) Receptive fields optimized for each band in (a). (**c**) Relative surround-to-center strength as a function of the elevation band. (**d**) Surround asymmetry as a function of elevation band. Orange mark denotes the horizon band.



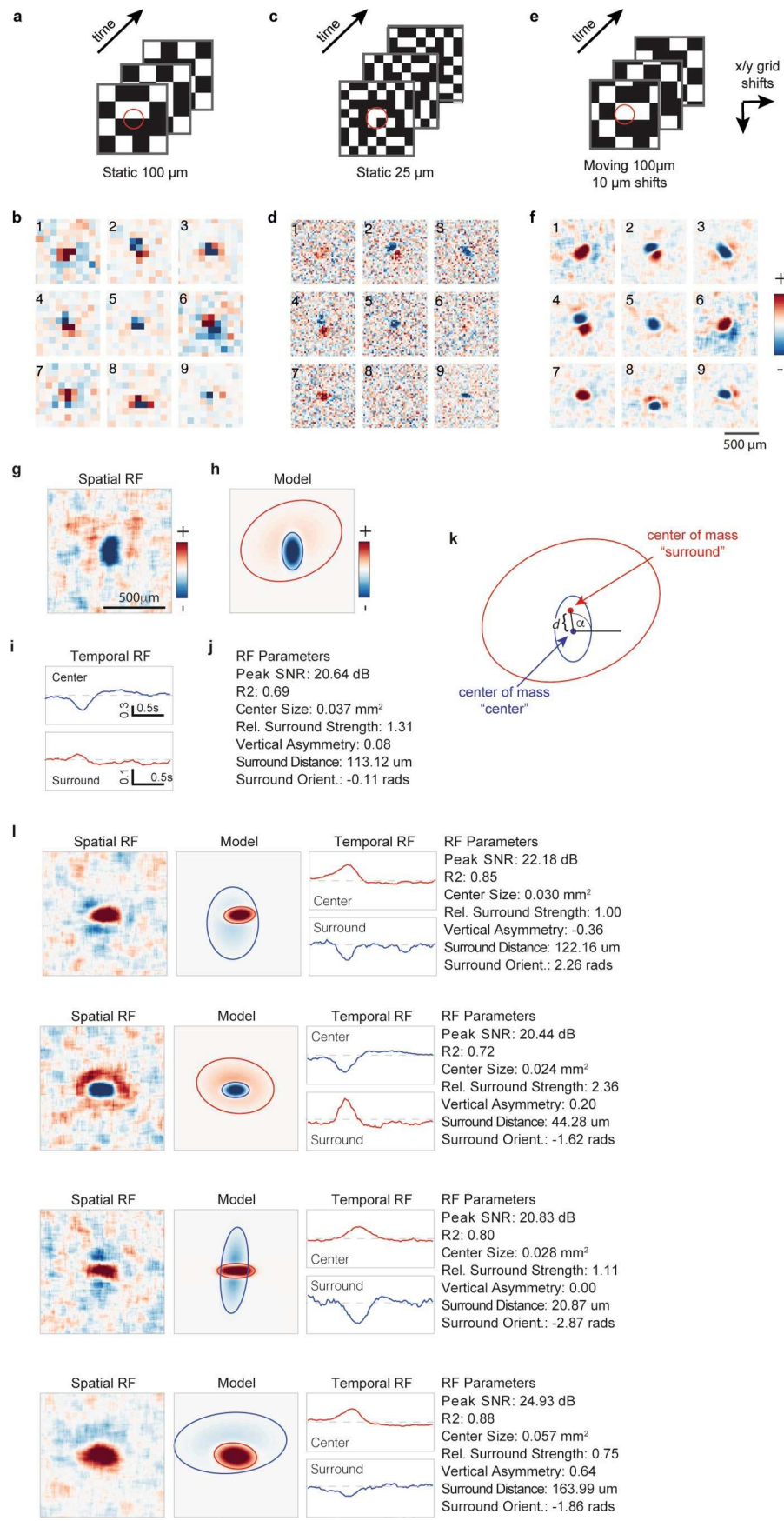
Extended Data Fig. 2 | Predictive coding model trained with an alternative set of natural images. We used natural images of animals and landscapes of the African savanna from van Hateren repository, used in 51 (a) Top - RFs optimized at different levels of SNR. Bottom – center size (purple line) and relative surround strength (black line) plotted as a function of the SNR. (b) Top - RFs optimized

at different levels of the vertical SNR asymmetry. Bottom – vertical surround asymmetry plotted as a function of the vertical SNR asymmetry of the model photoreceptor output (RGC input). (\mathbf{c}) RFs predicted for different positions within the visual field. (\mathbf{d}) Horizontal cross-sections of model RFs in (\mathbf{c}).



Extended Data Fig. 3 | **Clustering of Ca²⁺ signals to "chirp" stimulus shows segregation into functional types.** (a) normalized Ca^{2+} responses to changes in frequency, contrast, and luminance, known as "chirp" stimulus from RGCs, sorted by cluster ids, as determined by GMM. (b) Mean and standard deviation of each cluster reveal ON (cluster 2, 4, 8, 9, 10, 11, 13, 14, 18), OFF (5, 12, 15, 16), ON-OFF (3, 6, 7, 17), suppressed-by contrast (1, 19) RGC-types, as well as differences in frequency tuning to slow (for example, cluster 4), mid (for example, cluster 3), fast (for

example, cluster 11) and all frequency modulations (for example, cluster 2) or difference in luminance sensitivity (for example, compare ON responsive cluster 14 and 18). Note: clusters 15 and 19 are not homogeneous, as seen in their large standard deviations. (c) Chirp-response quality index versus surround strength, determined using their spatiotemporal filters (as in Fig. 2]). Good-quality chirp responses have a strong bias for weak surrounds. (d) Distribution of chirp quality index for weak and strong surround, as defined in (c, see color code).

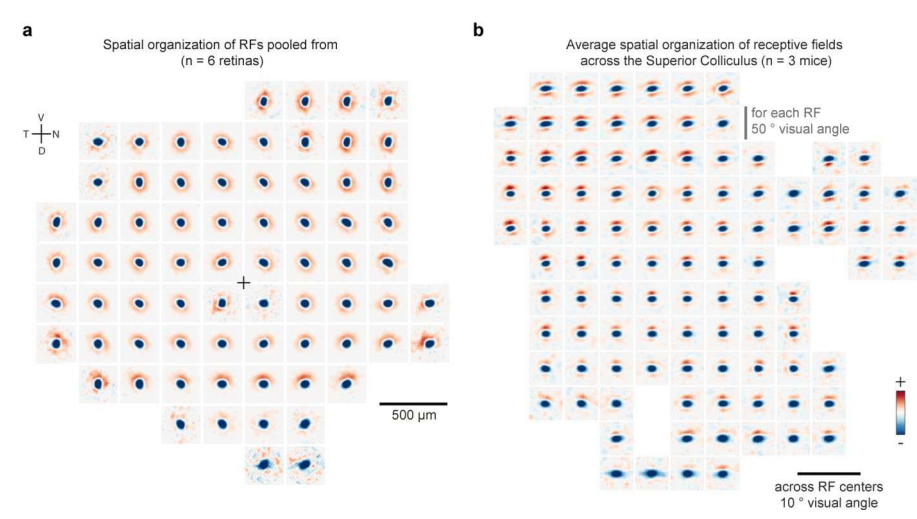


Extended Data Fig. 4 | See next page for caption.

 $\textbf{Extended Data Fig. 4} \ | \ \textbf{Comparison and parametrizations of RFs.} \ (\textbf{a})$

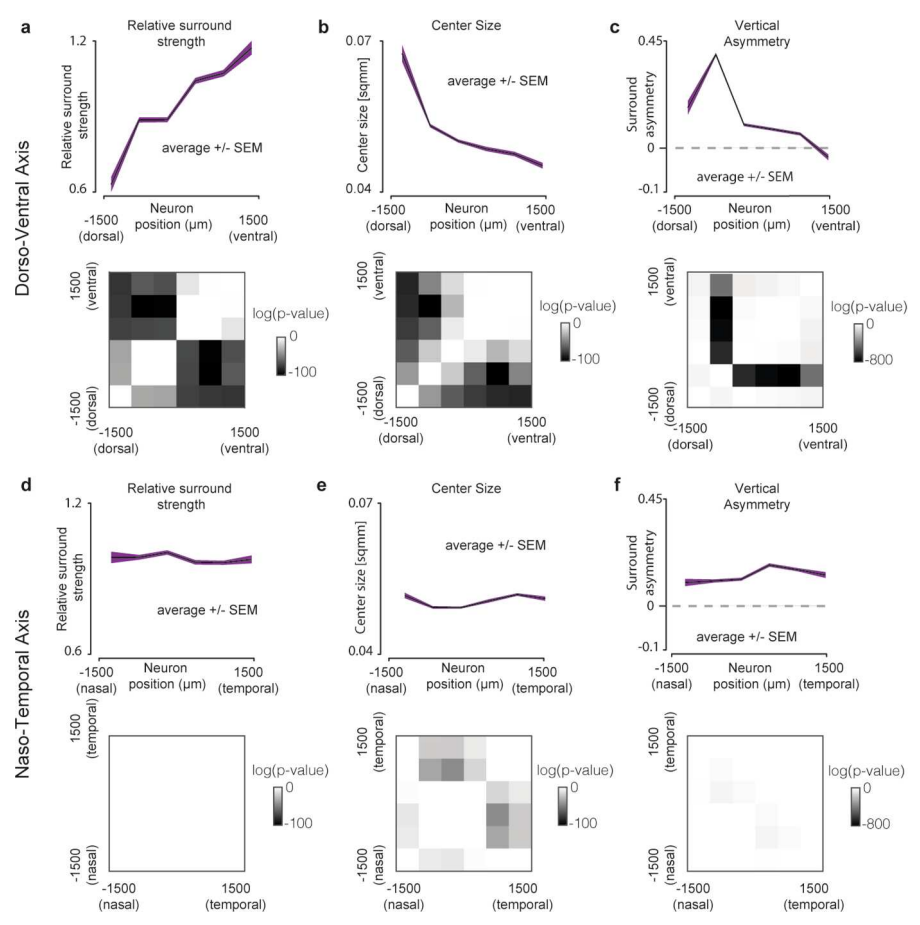
Schematic of binary white noise stimuli used for recovering RFs during imaging experiments for static checkers with grid size $100\times100~\mu m^2$. (b) Spatial RFs of 9 representative neurons were generated from the stimuli above. (c,d) Same as (a,b) for the same neurons, but for static 25 μm sized checkers. (e,f) Same as in (a,b) for the same neurons but for a shifting checkers with grid size $100\times100~\mu m^2$, where the entire grid was shifted by random multiples of $10~\mu m$ in both x- and y-axis. While the static $100~\mu m$ checkers were too low resolution for automatic analysis and the static $25~\mu m$ checkers were unable to drive many neurons strongly enough to elicit sufficient responses for RF reconstruction, the moving white noise stimulus was able to unambiguously recover the most detail in the

center–surround structure of RFs. (\mathbf{g}) Spatial receptive field snapshot at the peak center strength. (\mathbf{h}) Difference of Gaussians model fitted to the spatial RF. Ellipses represent 2 SD of the two Gaussians. (\mathbf{i}) Temporal trace of the mean value of pixels within the respective Gaussians (top: center, bottom: surround). Dashed line represents no correlation between stimulus and response. (\mathbf{j}) Values of different parameters of the RF reconstruction (Peak SNR), the goodness of fit (R2), centersurround structure (Center Size, Rel. Surround Strength) and eccentricity of surround (Vertical Asymmetry, Surround Distance, Surround Orientation). All neurons are plotted with the same scale and limits (after normalization). (\mathbf{k}) Schematic depicting the parametrization of the receptive field in (\mathbf{g}), showing the surround distance ("d") and orientation (" $\mathbf{\alpha}$ "). (\mathbf{l}) Example parametrizations.



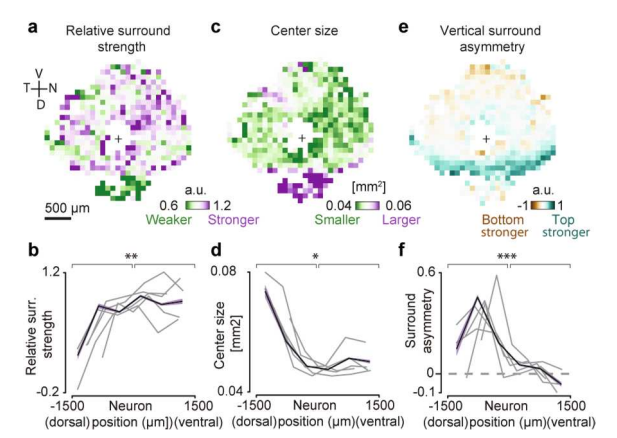
Extended Data Fig. 5 | Spatial structure of average RFs across the retina and superior colliculus. (a) Average spatial RFs of all RGCs in square bins of size $300\,\mu\text{m}$ at different positions of the retinal surface. As in Fig. 3a, but including cells from 6 retinas (n = 220 ± 200 cells per bin). Black cross: optic nerve head

position. (b) Average spatial RFs of all RGC boutons in square bins of size 5.6 ° at different positions in visual space. $n=93\pm68$ boutons per bin, only bins with n>=20 boutons shown.



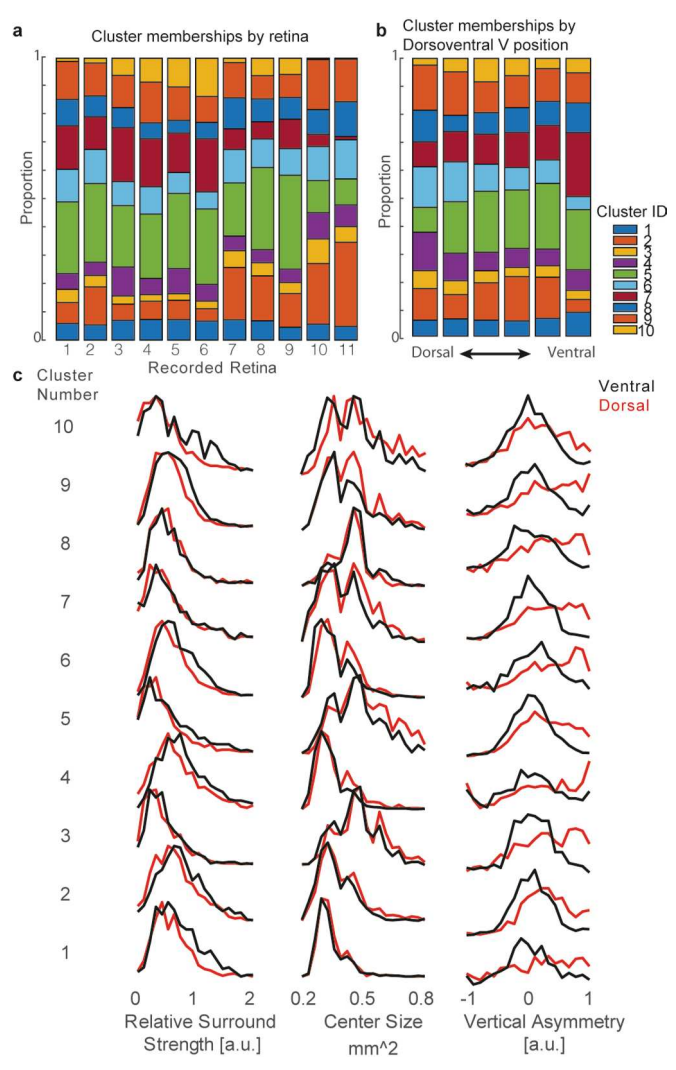
Extended Data Fig. 6 | Homogeneity of receptive field architecture in the temporal-nasal axis. (a) Top: Mean relative surround strength at 6 different dorsoventral positions. Bottom: p-values of two-sided Kolmogorov-Smirnov tests (with Bonferroni correction) between all pairs of bins. Darker colors represent higher significance levels that the cells in the two corresponding bins

have different surround strengths. (**b**) Same as (a), but for trends and significance levels across the naso-temporal axis. (**c**,**d**) Same as (a,b), respectively, but for center sizes. (**e**,**f**) Same as (a,b), respectively, but for Vertical surround asymmetry (n = 6 retinas with S-opsin staining).



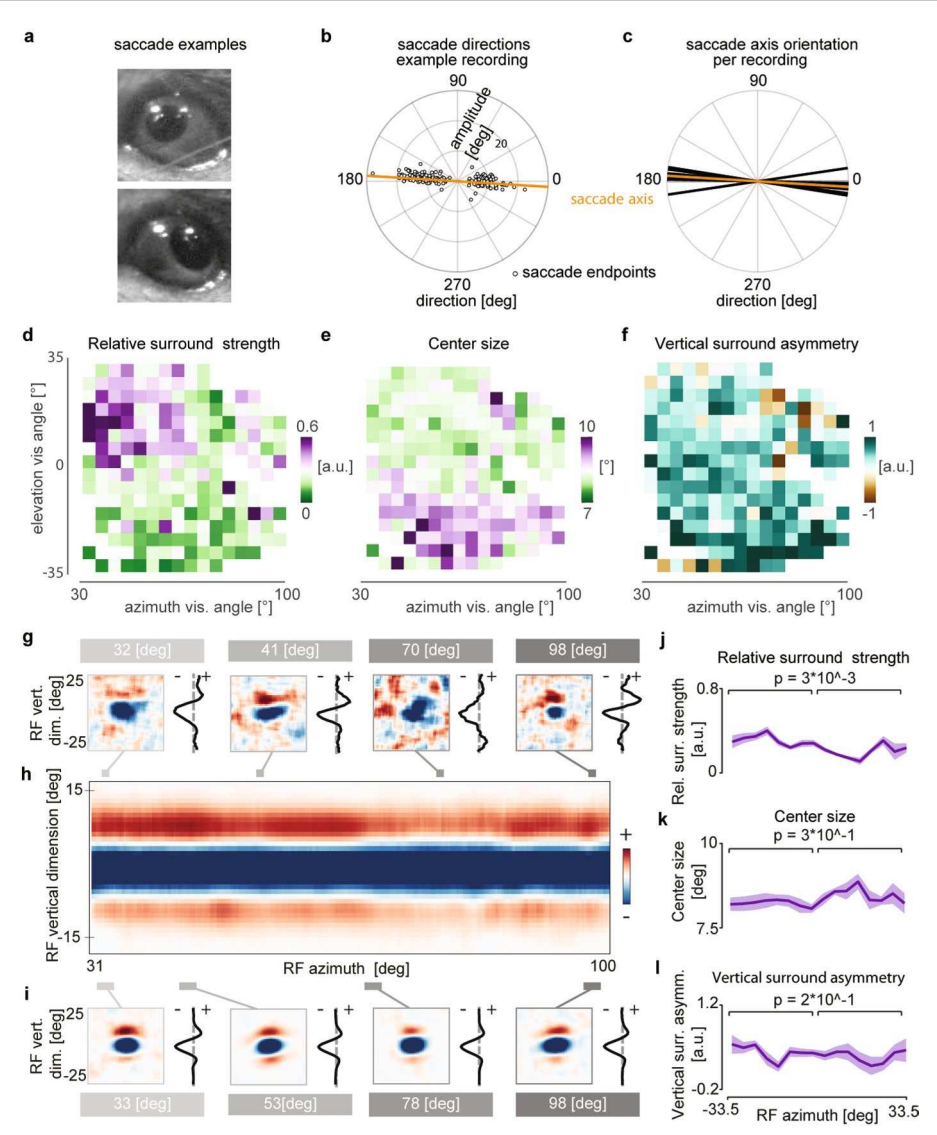
Extended Data Fig. 7 | Surround strength, center size and asymmetric streak align in retinas without an S-opsin staining. (a) Mean relative surround strengths of RGCs within $100 \, \mu m$ bins, pooled from n = 5 retinas. (Same as Fig. 3d) (b) Relative surround strengths for RGCs within 6 equally spaced bins along the presumed dorsoventral axis (color: mean and SEM pooled from n = 15449

RFs, grey lines: individual retinas). ($\mathbf{c} \& \mathbf{e}$) Same as (a), but for center size and vertical surround asymmetry, respectively. ($\mathbf{d} \& \mathbf{f}$) same as (b), but for center size and vertical surround asymmetry, respectively. (p-values for two-sided Kolmogorov-Smirnov test: (\mathbf{b}) 0.0047, (\mathbf{d}): 0.0168, (\mathbf{f}): 2.3766e-04.



Extended Data Fig. 8 | Proportions of cluster membership. (a) Fraction of cells from each retina that were classified into each of the 10 temporal RF clusters (from Fig. 4). **(b)** Fraction of cells across dorsoventral positions within bins of width 500 µm. **(c)** Distribution of relative surround to center strength,

center sizes and vertical asymmetry for each cluster, subdivided into ventral (above the optic nerve) and dorsal (below the optic nerve). For all statistics, see Supplementary Table 1.



Extended Data Fig. 9 | Sampling RGC bouton receptive field architecture across superior colliculus. (a) Two example video frame crops of eye in two extreme horizontal positions. (b) Polar scatter plot of individual saccade amplitudes and directions (gray dots) in example recording and computed saccade axis (orange line, saccadic orientation tuning r = 0.92). (c) Saccade axes of all recordings (n = 10 in 3 mice) close to the horizon (offset $= 5.5 \pm 2.9$ °). (d) Relative surround strengths of mean 1-d-RFs within 4.3° bins. $n = 45 \pm 40$ boutons per bin, only bins with n > = 5 boutons shown. (e & f) Same as (d), but for center size and vertical surround asymmetry, respectively. (g) Example RGC bouton

receptive fields recorded using "shifting" white noise (left) and their respective 1-d RFs (right) at different azimuth positions (gray lines). (h) Average 1-d RFs, in smoothed 0.22 ° bins over azimuth. (i) Example average receptive fields binned at 2.9 ° visual angle (left), with their respective 1-d RFs (right) at different azimuth positions (gray bars). (j) Relative surround strength of 4.1 ° binned average 1-d RFs, shading indicating SEM across elevation bins (shown in (a)). Regression weights for both elevation and azimuth shown in Fig. 5g. (k, l) as (j), but for center size and vertical asymmetry, respectively. p-values indicated in j-l for two-sided Kolmogorov-Smirnov test.

Supplementary Information

Supplementary Note 1

Here by following the derivation and assumptions proposed in 10 , we present an alternative, analytically-tractable model of predictive coding in retinal receptive fields. The receptive field model in 10 assumes that the center pixel $s_{t,cent}$ of the t-th stimulus $\vec{s_t}$ is subtracted from its linear prediction computed from the surround $\vec{s}_{t,sur}$. Instead of encoding the raw value of the central pixel, the model RGC encodes the difference between this prediction and the center in order to minimize the dynamic range of its output. The optimal prediction weights \vec{w} are optimized to minimize the mean squared error:

$$E(w) = \langle (s_{t,cent} - \vec{w}^T \vec{s}_{t,sur})^2 \rangle_t$$

where T denotes vector transposition.

The optimal vector of surround weights \vec{w} is a solution to the following equation:

$$R_{-c}\vec{w} = \vec{R}_c$$

where $R_{i,j} = \langle s_{t,i} s_{t,j} \rangle_t$ is the spatial autocorrelation of natural images, and i,j index pixels within an image patch, \vec{R}_c is the autocorrelation vector of the center pixel with all other pixels, and R_{-c} is the square correlation matrix of all pixels without the center pixel.

The correlation function $R_{i,j}$ is approximated analytically as:

$$R_{i,j} = M_i M_j + S_i S_j \exp\left[-\frac{d(i,j)}{D}\right]$$
, for $i \neq j$ and,

$$R_{i,j} = M_i^2 + S_i^2 + N^2$$
, for $i = j$,

Where M_i and S_i are mean and standard deviation of the i-th entry of the image intensity respectively, d(i,j) is the Euclidean, spatial distance between entries labeled i and j, D is a constant controlling the decay of the correlation, and N is the standard deviation of the noise.

The term $N_i N_i$ vanishes for $i \neq j$ because noise is assumed to be uncorrelated.

To approximate the spatial autocorrelation function of natural images as a function of elevation within the visual field, we created a dataset of images with simulated horizon as described in the Methods. We then divided each of these images into uniformly separated horizontal bands. We sampled square image patches within each band. We then computed mean vectors \vec{M}^y and standard deviation vectors \vec{S}^y , where the upper index y indicates the elevation band. Individual entries of these vectors corresponded to mean and variance of pixel values within the elevation band y respectively. We assumed constant values of the decay constant D and noise standard deviation N. Ratio of surround-to-center strength and surround asymmetry were computed as described in the Methods. We note that our results do not depend qualitatively on parameter choice and reveal similar trends across a broad range of parameter values.

	etry	p-value	1.65E-07	5.25E-29	1.08E-15	2.70E-09	4.77E-48	5.74E-22	5.18E-37	3.17E-18	2.11E-36	2.33E-09
DorsoVentral	Surround Asymmetry	ventral	0.03	0.08	90.0	0.03	90.0	0.09	0.05	0.04	0.04	0.04
	Surrc	dorsal	0.14	0.28	0.32	0.19	0.27	0.29	0.29	0.27	0.31	0.2
	Center Size	p-value	8.46E-09	1.12E-05	1.21E-02	1.16E-04	2.71E-15	5.86E-08	2.66E-12	7.56E-05	6.29E-05	2.64E-02
		ventral	548.77	498.37	538.77	539.96	422.16	584.43	398	549.61	456.73	401.73
		dorsal	664.41	522.56	511	554.94	455.46	640.8	438.7	595.29	479.29	407.83
	Strength	p-value	1.75E-11	1.42E-09	8.71E-01	7.31E-02	5.75E-19	1.48E-07	5.79E-12	3.80E-04	2.79E-07	8.13E-06
Dor	Relative Surround Strength	ventral	1.17	1.01	0.82	1.05	1.08	0.86	1.29	0.75	1.24	1.08
	Relativ	dorsal	0.77	0.88	0.87	0.94	0.88	0.68	1.04	99.0	1.08	0.91
	Tiling properties	ventral cell	457	1,115	280	494	1,682	209	1,009	674	880	386
		dorsal cell	475	096	372	989	1,672	922	875	579	1,032	579
		STD of Tiling	0.05	0.15	0.11	0.1	0.09	0.08	0.14	0.09	90.0	0.21
		Tiling	0.61	0.45	0.74	0.64	0.33	0.46	0.56	0.58	0.52	0.67
		Cluster	1	2	3	4	5	9	7	8	6	10

						Nas	NasoTemporal						
		Tiling p	Tiling properties		Relativ	Relative Surround Strength	Strength		Center Size		Surro	Surround Asymmetry	netry
Cluster	Tiling index	STD of	ncount	tcount	nasal	temporal	p-value	nasal	temporal	p-value	nasal	temporal	p-value
- 1	0.61	0.05	425	507	0.93	1	5.13E-01	637.35	582.86	2.13E-03	0.1	0.07	1.89E-01
2	0.45	0.15	1,020	1,055	0.95	0.94	5.27E-01	510.91	508.26	1.44E-01	0.19	0.16	3.82E-02
3	0.74	0.11	337	315	0.85	0.84	2.61E-01	525.55	520.12	6.33E-01	0.27	0.15	4.81E-05
4	0.64	0.1	491	639	0.89	1.06	3.67E-02	588.26	517.75	1.25E-03	0.17	80.0	1.10E-03
5	0.33	0.09	1,401	1,953	0.99	86.0	5.64E-01	441.21	437	2.95E-02	0.21	0.14	3.63E-06
9	0.46	0.08	754	775	0.72	0.78	7.59E-02	634.15	603.12	1.59E-02	0.22	0.2	1.01E-01
7	0.56	0.14	778	1,106	1.16	1.18	4.29E-01	420.44	414.42	1.83E-01	0.22	0.12	1.06E-05
8	0.58	0.09	579	674	0.67	0.74	3.81E-03	597.96	547.32	7.52E-07	0.15	0.14	3.13E-01
6	0.52	90.0	911	1,001	1.15	1.15	9.47E-01	463.65	473.69	7.22E-01	0.2	0.18	3.70E-01
10	0.67	0.21	346	619	0.97	86.0	3.85E-01	403.1	406.67	1.42E-01	0.15	0.12	2.78E-01

Supplemtary Table 1: RF properties across retinal quadrants for different functional clusters All axis are defined from the optic nerv perspective, i.e., dorsal: below the optic nerve. Statistics: Kolmogorov-Smirnov test

Collicular adaptations to internal and external context

Abstract — Sensory systems constantly adapt their representations to maintain efficient processing and perception across contexts. Previous *ex-vivo* experimental work in the retina has shown that the spatiotemporal filters shift to higher frequencies with increasing luminance, while neurons in the visual cortex are modulated by the behavioral demands of the animal. However, the adaptability of the superior colliculus (SC), an important sensorimotor hub, to such external and internal contexts is less understood. Here, we try to address this gap using neuropixel recordings in awake-behaving mice, measuring high-resolution spatiotemporal receptive fields at different light levels and arousal states. Early results suggest that the SC primarily adjusts temporal processing through latency shifts without significant changes in frequency selectivity. Additionally, we show that pupil dynamics also modulate receptive field (RF) latencies in a manner similar to luminance adaptation, with faster visual responses at times of higher arousal. These latency shifts were conserved for all neurons in a population, suggesting that relative timing between neurons may play a crucial role in maintaining an invariant visual code across internal and external contexts.

3.1 Introduction

Sensory systems exhibit remarkable adaptability, adjusting to changing environmental conditions to maintain efficient processing and accurate perception. The amount of ambient light increases by roughly 8-10 orders of magnitude (~billion-fold) between a moonless night (scotopic) and high noon (photopic)(Spitschan et al., 2016). In the early visual system, *ex-vivo* retinal ganglion cells (RGCs) have been shown to adapt their filtering properties in response to varying light levels. As light levels increase, the center-surround structure of spatial filters becomes more pronounced and temporal filters become faster and more biphasic (Barlow et al., 1957; Enroth-Cugell & Shapley, 1973;

Ogawa et al., 1966; Ruda et al., 2022). As a result, RGCs tend to emphasize lower frequency content at lower light levels. These adaptations align with efficient coding theories, which suggest that sensory systems subtract away predictable components of the environment in order to maximize information transfer (Atick & Redlich, 1990; Barlow, 1961; Srinivasan et al., 1982). Crucially, this subtraction is only possible given sufficient Signal to Noise Ratio (SNR), and thus, optimal filters look like stretched monophasic integrators at low light levels, and faster biphasic differentiators at higher light levels (Atick & Redlich, 1990; Gupta et al., 2023; Srinivasan et al., 1982). Some RGC responses have even been found

to reverse their ON or OFF polarity depending on global or local brightness levels (Goldin et al., 2022; Tikidji-Hamburyan et al., 2015), presumably to continue to signal unexpected inputs under changing contexts.

Such diversity in coding strategies by the retina raises the question about how downstream areas interpret these adaptive codes and whether they also show similar adaptations in filtering properties. Although studies have failed to find significant luminance adaptations of spatial tuning in the visual cortex (Bisti et al., 1977; Duffy & Hubel, 2007; O'Shea et al., 2024; Ramoa et al., 1985), more dynamic modulations of visual coding have indeed been found in-vivo. Arousal-like signals, as measured by locomotion or pupil dilation, have been shown to dynamically affect the firing rates or spectral preferences of cortical neurons (Franke et al., 2022; Niell & Stryker, 2010; Reimer et al., 2014; Saleem & Busse, 2023; Vinck et al., 2015), altering sensory processing based on behavioral demands.

While substantial adaptation research has focused on the retina and the primary visual cortex, the adaptability of another important visual pathway, the superior colliculus (SC), under varying environmental and arousal states remains less understood. The SC is crucial for computing spatial attention to guide orienting behaviors (Basso & May, 2017; Krauzlis et al., 2013), yet the repertoire of its visual processing capabilities is only starting to be fully appreciated (Hafed et al., 2023; Y.-t. Li & Meister, 2023). It remains largely unknown if it adjusts its visual processing under different luminance levels like the retina or varying arousal states like the cortex. Studies that have looked at modulation of SC visual responses with locomotion have found somewhat mixed effects on response amplitude and spatial tuning (Ito et al., 2017; Savier et al., 2019; Schröder et al., 2020). Furthermore, owing to the limitations of calcium imaging, these studies often did not have enough temporal resolution, to investigate fine modulation of temporal processing.

In the present study, we leverage the power of

high-throughput Neuropixel recordings (Steinmetz et al., 2021) and high-resolution spatiotemporal receptive field analysis (Gupta et al., 2023) to explore the adaptation of visually responsive SC cells under changing luminance and arousal settings. Our current results show that under lower light levels or low arousal states, neural populations in the SC slow down their response latencies in concert. This temporal latency was measurable both in spike timings of responses to natural movies and in temporal RFs measured from white noise analysis. Unlike retinal adaptations, we did not see a significant stretching of spatial or temporal filters under low light levels. These preliminary results suggest that the SC may utilize a relative timing code to maintain invariant visual representations across light levels, while also facilitating faster visual processing under states of higher arousal.

3.2 Results

Population spike timing changes with luminance

To study the effects of luminance on visual responses in the intact early visual system, we recorded neural activity from the superior colliculus of a mouse running on a spherical treadmill, while viewing stimulus movies on an immersive dome screen (Fig. 3.1A). Using Neuropixel 2.0 probes, we could target the visually responsive superficial SC (sSC) on all four of its shanks, allowing us to collect data from a span of around $800\mu m$ along the mediolateral and rostro-caudal extent of the SC (Fig. 3.1B). We varied the mean luminance of the visual input using neutral density filters, going from a scotopic regime to roughly mesopic, while allowing some time for bright adaption in between (Fig. 3.1C).

Spike responses to repeated trials revealed that population spike timing varies systematically with luminance. Firstly, spike rasters and Peri-Stimulus Time Histograms (PSTHs) demonstrate that although the time-varying firing rate of a given neuron did not appear to

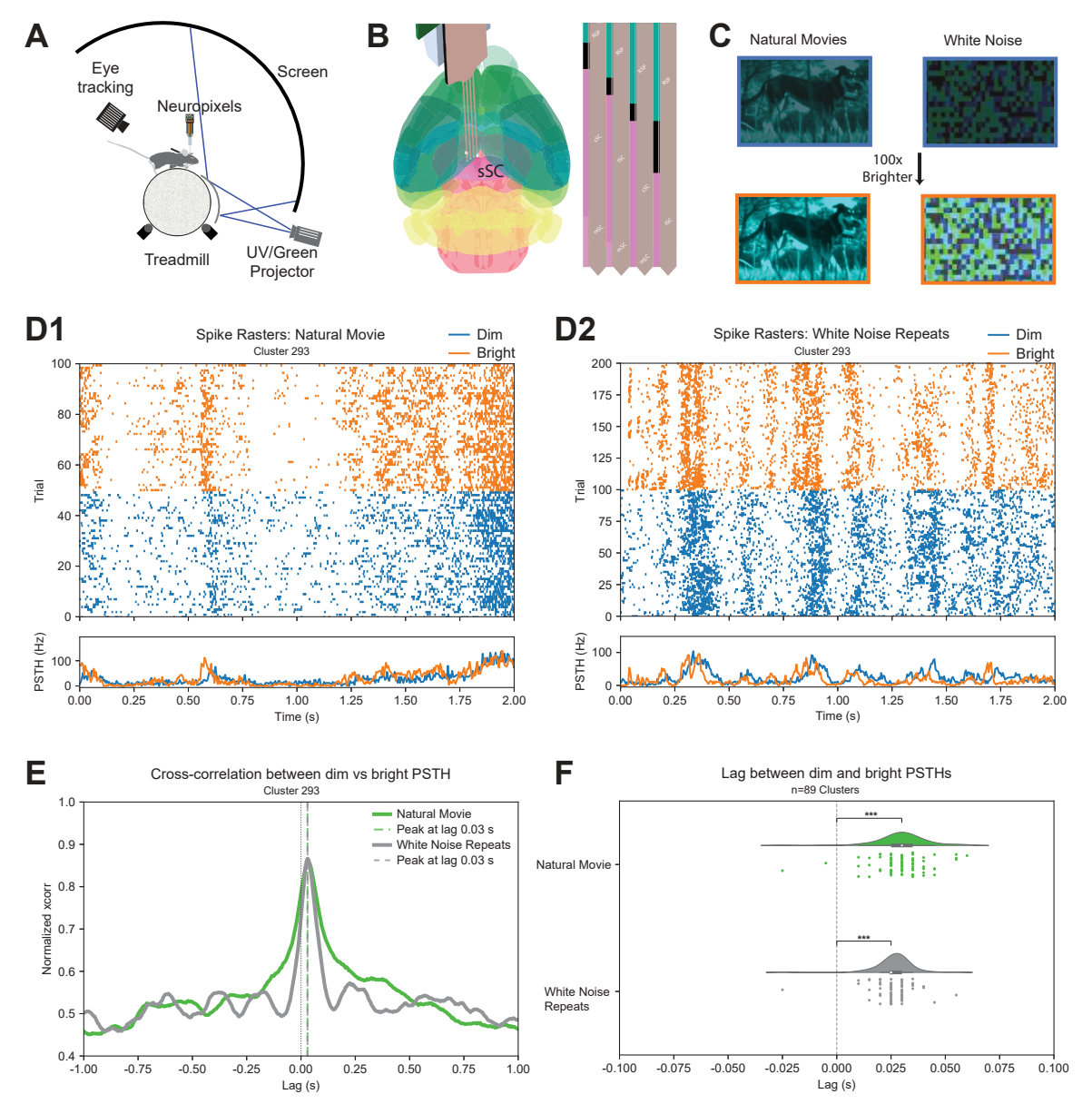


Figure 3.1: Population spike timing changes with luminance. (A) Schematic of recording setup for in-vivo extracellular electrophysiology. (B) Left, trajectory of Neuropixel 2.0 insertions in the superficial superior colliculus (sSC). Right, the brain structures encountered along the length of the 4 shanks. Schematic adapted from the Pinpoint software (Birman et al., 2023) using the Allen Mouse Brain Atlas. Green, Retrosplenial Cortex (RSP), Pink: SC. (C) Stimulus paradigm schematic showing example frames from the Natural Movie and Shifting White Noise Stimuli at different mean luminance levels. (D1) Top, spike raster plot for one neuron showing the timing of spike responses to different repeats of the natural movie stimulus at the dim and bright conditions. Bottom, mean response across trials, i.e. the Peri-Stimulus Time Histogram (PSTH), in spikes/second. (D2) Same as (D1) but for white noise stimulus. The dim PSTH slightly lags behind the bright PSTH for both stimuli types. (E) The cross-correlation function between the dim and bright PSTHs of the neuron in (D) and the lag at which it peaks. Note that positive lags indicate a leading bright PSTH. (F) Distributions of the lags at which the cross correlations peak for a population of simultaneously recorded SC neurons visualised as a 'raincloud' plot (Allen et al., 2021). One sample Wilcoxon test for greater than zero lag; Natural Movies p-value=9.8e-12, White Noise p-value=2.7e-7

change its shape between the dim and bright conditions, the dim responses lagged the bright responses by a consistent delay (Fig. 3.1D). This phenomenon was observed for both the natural movies and the white noise stimulus.

Next, we quantified this temporal lag using cross-correlation analysis, which showed that although the PSTHs in the dim and bright conditions were highly correlated to each other, the peak of this correlation was at a positive lag of around 30ms, confirming that dim responses do largely mimic bright responses but with a considerable lag (Fig. 3.1E). Finally, and perhaps most strikingly, this lag was similar for all neurons in the recorded population (Fig. 3.1F), suggesting that the entire population slows down in concert.

Temporal RFs shift with mean luminance

The effect of faster responses under higher luminance (and vice-versa) was also observed in the temporal receptive fields of SC neurons. We computed the spatiotemporal filters for dim and bright conditions separately using the shifting white noise stimulus introduced previously, and then decomposed them into spatial snapshots and temporal traces (Gupta et al., 2023). Although the spatial filters were mostly unchanged across luminance, the dim temporal filters appeared to be delayed versions of the bright filters (Fig. 3.2A1-2). This latency between the dim and the bright temporal filters can be quantified by measuring the difference in time to peak of the two filters for each neuron. Similar to the cross-correlation analysis of PSTHs (Fig. 3.1F), it was observed that these delays could range from 20 to 60ms, but were tightly clustered for all neurons of each simultaneously recorded population (Fig. 3.2B).

A delay in the peak of the temporal filters can be caused either when the filter is stretched in the time axis (corresponding to selectivity for lower frequencies in the Fourier domain) or shifted (corresponding to a phase difference). Previous experimental and theoretical work has shown that ex-vivo retinal ganglion cells (RGC) tend to show a change in their frequency tuning with light levels, with stretched filters at low light levels (Enroth-Cugell & Shapley, 1973; Ogawa et al., 1966; Ruda et al., 2022). To quantitatively distinguish between these two possibilities, we parameterized the temporal RFs with a biphasic function adapted from (Adelson & Bergen, 1985) (Fig. 3.2A3). First, all the parameters of the function (sign, first phase, second phase, stretch, and shift) were fitted to the bright RF, and then either the stretch or the shift was re-optimized to best fit the dim RFs, while keeping the other parameters fixed. This analysis shows that for two of the four animals, the dim RFs were closer to a shifted version of the bright RFs, than to a stretched version, while for the other two, the shifted or stretched filters were comparably good at describing dim RFs (Fig. 3.2C). The variability between animals could possibly arise from differences in the initial dark adaptation period, and requires further investigation. See also the discussion section (3.3).

Pupil size modulates RF dynamics

In the intact visual system, the pupil also plays an important role in modulating the amount of light reaching the retina. Besides being modulated by external light levels (via the pupillary light reflex), the pupil diameter can also change dynamically under constant luminance by upto 10-fold as a result of the state of arousal of the animal (Joshi et al., 2016) (Fig. 3.3A-B). Neurons in the mouse visual cortex have been found to change their spectral preferences as the arousal state changes (Franke et al., 2022), however the effect of this dynamic behavioral modulation on spatiotemporal feature selectivity is still unknown.

To study the effect of pupil dilation on feature selectivity, we computed spatiotemporal RFs separately at different pupil sizes. The duration of the recording was divided into 'rest' or 'active' epochs based on the pupil area being below or above the 33rd and 66th percentiles, respectively. The absolute thresholds were thus different for each animal, but the upper

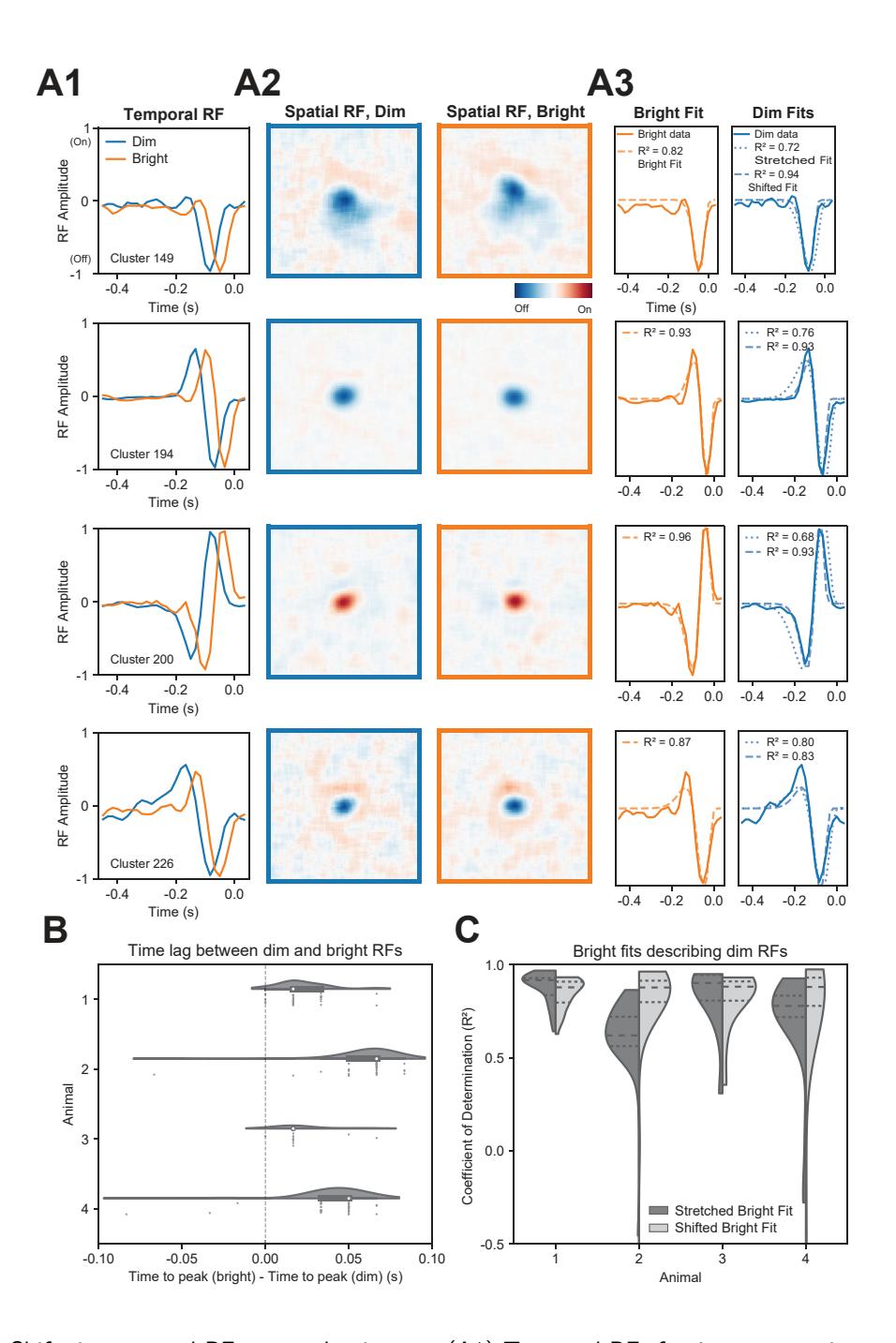


Figure 3.2: Shifts in temporal RFs across luminance. (A1) Temporal RFs for 4 representative neurons under dim and bright white noise stimuli. (A2) Spatial RFs for the neurons in (A1). (A3) Left, a parametric biphasic function fitted to the bright temporal RFs along with its goodness of fit (R 2). Right, performance of the parametric function in describing the dim RFs when only a stretch or a shift was allowed, while fixing the other parameters to the bright fit. Solid lines show the temporal RFs from (A1) and dashed or dotted lines show fits. (B) Differences in the peak timepoint of the temporal RF between the dim and bright conditions. One sample Wilcoxon test for pooled data with n = 114 neurons, p = 2.9e-17. Wilcoxon test for animal means, N = 4 animals, p = 0.0625. (C) Comparison of goodness of fit to the dim RFs for parametric functions that allow either stretch or shift to the bright fits, as in (A3), n = 132 neurons. Dashed lines inside the violin plots represent quartiles.

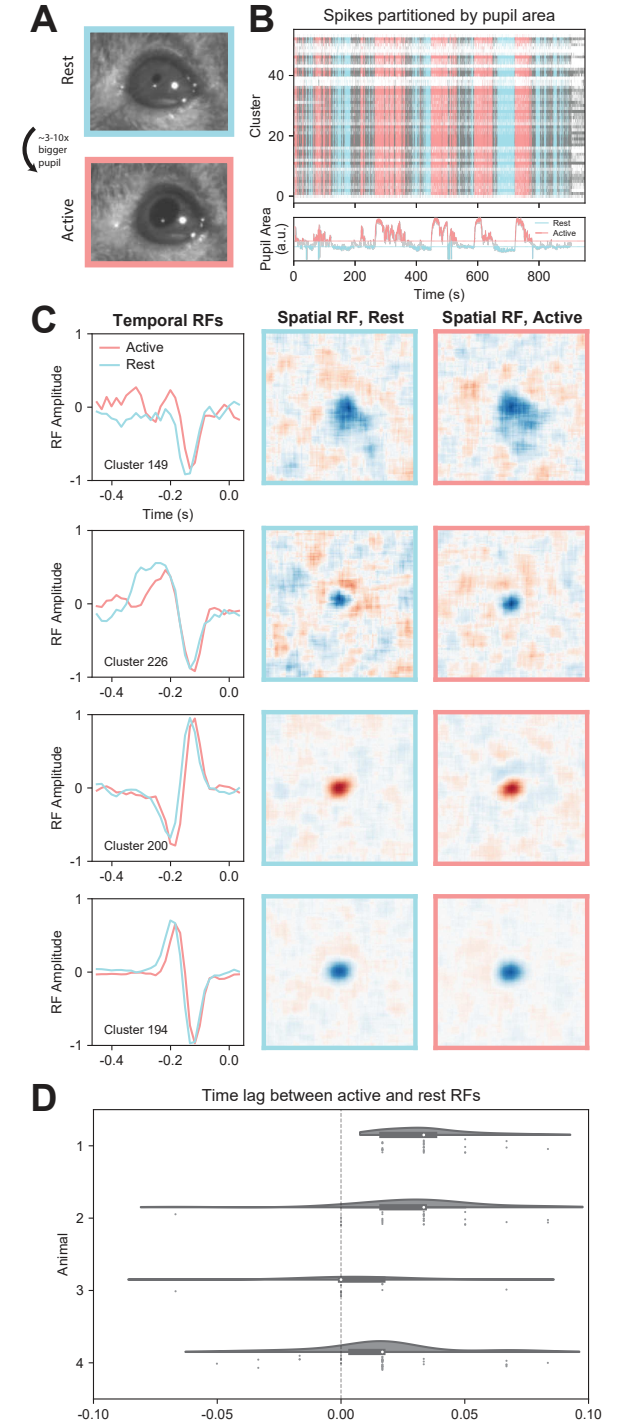


Figure 3.3: Changes in RF dynamics with behavioral state. (A) Example frames from the eye tracking camera showing differences in pupil size. (B) Recording epochs selected for computing rest or active RFs, based on the thresholded pupil area at the time of each spike. (C) Temporal and spatial RFs for the same neurons as in 3.2 (A), but for rest or active states under dim luminance. (D) Differences in the peak timepoint of the temporal RF between the active and rest conditions. One sample Wilcoxon test for pooled data with n = 111 neurons, p = 5.9e-13. Wilcoxon test for animal means, N = 4 animals, p = 0.0625.

threshold was, on average, 81 ± 53 percent larger than the lower threshold. The spikes in these epochs were collected and subsampled to ensure that equal number of spikes were used for the STA computation under both conditions. (Fig. 3.3B). Despite using just 1/3rd of the total spikes (or about 5 minutes of effective recordings), robust RF estimates could be obtained for each behavioral state (Fig. 3.3C). Only stimuli under the 'dim' luminance condition were used for this analysis, since tracking of the smaller pupil was less reliable under the 'bright' condition.

Similar to the effects of background luminance, the spatial RFs were largely unchanged across behavioral states, while the temporal filters showed a small but consistent delay (15-30ms) in the rest state (Fig. 3.3C left). Measuring the difference in time to peak of these temporal filters showed that, similar to (Fig. 3.2B), the response latencies of all neurons in a population shift by the same amount as the behavioral state of the animal changes (Fig. 3.3D).

3.3 Discussion

In this study, we set out to investigate how changes in external or internal context shapes the processing of visual information in the early visual system. We found that both luminance and arousal states cause a concerted change in the response timings of SC populations. Spike timings, and likewise receptive fields, are much faster in mesopic conditions than in the scotopic regime. At the same time, arousal, as measured by pupil dilation, also reduces latency in visual processing. Our results highlight the dynamical interplay between sensory processing and behavioral demands.

Comparison to Efficient Coding

The defining feature of visual adaptation from scotopic to mesopic regime is the activation of the cone pathway. Cone responses are known to be faster than that of rods, with a rod-cone latency of 20-80ms, depending on species,

background illumination and whether latencies are measured physiologically or psychophysically (Barbur, 1982; Baylor & Hodgkin, 1974; Schneeweis & Schnapf, 1995; Zele et al., 2008). Although these rod-cone latencies are consistent with the differences in latencies we have observed in the SC (Fig. 3.3F and 3.2B), rods are also more sluggish, and one would expect downstream temporal filters to also stretch. Retinal ganglion cell RFs have been suggested to utilize this longer integration time to emphasize lower frequency information as a means to combat the lower SNR in the dark (Atick & Redlich, 1990; Srinivasan et al., 1982).

In contrast to RGC RFs (Enroth-Cugell & Shapley, 1973; Ogawa et al., 1966; Ruda et al., 2022), however, we do not see a prominent stretching of temporal RF at low light levels (Fig. 3.2C). Thus, our data suggests that at the level of the SC, the only adaptation necessary in filter properties is a shift in timing, while the frequency components of spatial and temporal processing remain unchanged. For this to happen, the stretched scotopic RGC filters would have to be 'sharpened' again in the SC. The convergence of different types of RGC channels onto individual downstream neurons (O'Shea et al., 2024) has been proposed as one potential mechanism for luminant invariant representations in the visual cortex.

Relative timing code

Although adaptations in RGC filters allow the system to continue to operate under low SNR regimes, it poses a challenge for downstream circuits to interpret this altered encoding to extract similar stimulus features, that is, to maintain an invariant percept across light levels (O'Shea et al., 2024). When RGC temporal filters are stretched at low luminance, the spike timings of individual neurons would become less reliable.

Our observation regarding timing shifts within a population provide an important hint to the properties of the neural code that may be important for invariant representations across

luminance and behavioral states (Wienbar & Schwartz, 2018). Even as responses for individual neurons get delayed at low light levels or low arousal, these latencies are similar for the entire population (Figs. 3.1F, 3.2B) and 3.3D), and thus the relative timing of spikes between neurons must be conserved. Such relative timing codes have been shown to carry more information about the stimulus than firing rates in the barrel cortex (Petersen et al., 2001) and the retina (Gollisch & Meister, 2008). Interestingly, contrast changes also cause a delay in spike timings of individual neurons, but preserve the relative timing between pairs of neurons. This allows a common decoding mechanism, simulating a downstream neuron interpreting a relative timing code, to perform well independent of input contrast (Gollisch & Meister, 2008). Our results in the coordinated temporal shifts of the neural population suggest that a similar mechanism might be at play in the superior colliculus, in order to adjust to an altered code coming from the RGCs at different luminance levels.

Behavioral modulation of visual processing

Even when the external luminance is kept constant, we see a change in RF dynamics with pupil size. One explanation would be that since pupil dilation changes the amount of light reaching the retina, this could be enough to cause some of the luminance adaptation observed above. The absolute magnitude of this latency shift due to behavioral state would be smaller than the shift due to luminance, since the pupil size changes only by about 3to 10-fold as opposed to the 100-fold change imposed in the luminance experiments. If the modulation of temporal latencies is just due to effective light levels, then this would explain why the change in latencies in (Fig. 3.3D) is considerably smaller than those in (Fig. 3.2B).

However, arousal-related neuromodulatory effects cannot be ruled out in dynamically shaping visual computation. Pupil dilation is strongly linked to the release of norepinephrine

from the Locus coeruleus which projects to the intermediate SC (Joshi et al., 2016). The effect of this norepinephrinergic projection on visual processing in the SC, if any, is largely unknown and is the subject on ongoing research in our lab. Pupil dilation has also been found to strongly correlate with inhibitory GABA-ergic inputs from the ventral Lateral Geniculate Nucleus (vLGN) to the SC (Vega-Zuniga et al., 2024). This vLGN to SC projection has been shown to sharpen spatial tuning in the SC by strengthening the inhibitory surround (Z. Li et al., 2023). Although we did not notice any striking changes in spatial surrounds across behavioral states, more diligent quantification can yet reveal subtle differences in surround strengths (Gupta et al., 2023). Lastly, the effect of histamine on the optic tract and LGN shows a strikingly similar shift in RF latencies without significantly altering frequency tuning (Tripodi & Asari, 2024).

One way to disentangle the luminance vs neuromodulatory source of this modulation would be to control the amount of light entering the eye. This can be done pharmacologically by dilating the pupil of one eye with Atropine (O'Shea et al., 2024) and measuring arousal either by tracking the pupil area of the other eye, or by using the animal's running speed as a proxy (Erisken et al., 2014).

As for the need of behavioral modulation of visual processing, one can imagine several scenarios where faster visual processing during aroused states could lead to a survival advantage. For instance, auditory or olfactory cues of a lurking predator could preemptively increase the arousal level of the animal, leading to a faster visual reaction time when needed. This prediction of faster reaction times at bigger pupil sizes may already be testable by reanalyzing publicly available large behavioral datasets (Groblewski et al., 2020).

Limitations of this study

The consistent nature of the observed temporal shifts leads to a potential concern of synchronization artifacts, for example through clock drifts across long recordings. Although this possibility cannot be ruled out completely yet, we have not been able to find any such discrepancies to the best of our ability. It is also worth noting that such artifacts would be much less likely to contaminate results from (Fig. 3.3) since the epochs being compared are closely interspersed, unlike (Figs. 3.1 and 3.2), where the need for light adaptation necessitates long gaps between the spike trains or RFs being compared.

Another important caveat of our data is the somewhat large animal to animal variability in the shifts of population response timings (Figs. 3.2B and 3.3D). One potential cause is that the duration for the initial dark adaptation was not standardized, and thus, the rods may have been at different levels of sensitivity across animals. This is an important factor that will have to be more carefully controlled in future experiments. Currently, statistical comparisons are reported in two ways: after pooling all neurons across animals, and for the means of individual animals. More sophisticated statistical methods, like mixed effects models or generalized linear mixed models, could appropriately account for the hierarchical nature of these data. This structure is often neglected in neuroscience studies and is slowly being addressed in the field (Aarts et al., 2014; Yu et al., 2022). The differences in behavioral modulation of latency are more understandable considering that the relative pupil dilation between rest and active states can be different for different animals.

Additionally, the experiments comparing spike timings (Fig. 3.1) need to be repeated for more animals (currently only N=1 animal is shown). The quality of RF estimates was used as an inclusion criteria to select visually responsive neurons for the cross-correlation analysis. However, there are technical challenges with estimating the Spike Triggered Average from white noise with a repetitive trial structure, and thus only natural movie will be used for future experiments to keep the recordings reasonably short.

3.4 Methods

3.4.1 Animal Management

All electrophysiology experiments were performed on male and female adult wild type C57BL6/J mice. All experimental procedures were approved by the Ethics Review Board at ISTA and the animal husbandry was carried out by the Preclinical Facility at ISTA. The mice were singly or doubly housed, and their home cages contained a running wheel to better habituate the animals to running on a treadmill. The lighting followed a standard 12 hour day-night cycle, and the experiments were carried out during the night phase, when mice tend to be more active.

3.4.2 Surgical Preparation

The mice were first anesthetized with 2-4% isoflurane, and then injected with Ketamine and Xylazine (100 mg/kg, 10 mg/kg, i.p.). This was followed by injection of Meloxicam (20mg/kg Subcutaneous), application of Oleovital over the eyes, and shaving of the scalp. The mice were then placed on a heating pad and mounted to the stereotax equipment (Kopf). Anesthesia was maintained with $\sim 1\%$ isoflurane. The surgery was sometimes split into two phases performed on different days, to allow more time for recovery. The preceding steps were common between the two phases. In the first phase, a custom 3D-printed titanium headplate was cemented onto the skull and the coordinates of the future craniotomy were marked. Local anesthesia was applied over the scalp, and after disinfection with Betadiene, incisions were made to expose the skull. The periosteum was then cleared and the bone surface was dried with compressed air and scored with a needle. The rectangular craniotomy coordinates used for the left SC were 3-4mm posterior and 0-1.5mm lateral from Bregma. However, the exact location varied slightly across animals to try to keep the craniotomy as medial and posterior as possible, while avoiding the sagittal sinus and left trans-

visible when the skull is still wet. Another craniotomy was marked for the reference electrode, roughly 2mm anterior and 2mm right lateral from Bregma. The coordinates were marked on the skull with a micropipette tip dipped in Methylene blue or with a sharp graphite pencil. Finally, the skull around the marked areas was covered first with Optibond, and then Karizma, to prepare it for cementing. The U-shaped headplate was cemented with C&B MetaBond and a small well was created to separate the SC craniotomy from the reference electrode.

The second surgery involved the actual craniotomy and insertion of the reference electrode. The craniotomies were made by careful drilling over the marked coordinates with 0.3-0.5mm drill bit, while avoiding the major blood vessels. For the SC craniotomy, the edges of the rectangle were thinned, till the the bone island moved almost freely. Then a forcep was carefully inserted under the bone and the entire piece was removed whole. Any bleeding was contained with Haemostatic sponges. The brain was kept wet with saline and if unsharpened Neuropixels were being used, the dura was carefully removed. The exposed brain was then covered with KwikSil or DuraGel. The reference craniotomy was drilled similarly and the male side of a thin gold pin was inserted. The gap between the pin and the craniotomy was filled with vaseline, and the exposed female sides of the pin were cemented in the shape of a volcano. The mice were reinjected with 150 μ L metacam after each surgery and returned to a heated home cage.

3.4.3 Behavioral Tracking

the bone surface was dried with compressed air and scored with a needle. The rectangular craniotomy coordinates used for the left SC were 3-4mm posterior and 0-1.5mm lateral from Bregma. However, the exact location varied slightly across animals to try to keep the craniotomy as medial and posterior as possible, while avoiding the sagittal sinus and left transverse sinus. These blood vessels are partially

(Mathis et al., 2018). The first pass tracked the gross position of the eye in the video, and then a high-res crop around the eye was used to track 8 points around the pupil in the second pass. An ellipse was fitted around these 8 points and the area of this ellipse was used as the pupil area.

3.4.4 Stimulus

In the recording setup, the animal was surrounded by a spherical screen (80cm diameter) that covers $\sim 170^{\circ}$ of horizontal and $\sim 90^{\circ}$ of vertical visual field. Visual stimuli were presented via a spherical mirror by a DLP projector (TexasInstruments LightCrafter 4500) modified to emit UV in the blue channel. The relative currents of the green and UV channels were calibrated to approximately match S and M cone activation at twilight (Spitschan et al., 2016) using the respective opsin templates (Govardovskii et al., 2000). The estimated rhodopsin isomerizations per second per rod (R^*) were 10^3 in the 'bright' condition and an OD2 filter (Thorlabs NE520B) was added in the projector path to get approximately 100fold reduction in the 'dim' condition. Stimuli were designed and presented with Psychtoolbox, running on MATLAB 2017a (MathWorks). Stimulus frames were morphed on the GPU using a customized projection map and an OpenGL shader to counteract the distortions resulting from the spherical mirror and dome.

A shifting spatiotemporal white-noise stimulus was presented using a binary pseudorandom sequence, in which the two color channels (Green and UV) varied dependently. All white-noise stimuli were presented at a 20-Hz update for 15 minutes. The checker size was a visual angle of $6 \times 6^{\circ}$ and the entire grid was shifted by random multiples of 0.6° visual angle in both elevation and azimuth axis after every frame (Gupta et al., 2023). In some experiments, the seed (and state) of the random number generator for the white noise was reset to the initial value every 10 seconds for 90 repetitions. The natural movie was an achromatic 'mouse-view' video recorded by one of the au-

thors at 120Hz and presented at 60Hz. To avoid sudden jumps in the scene, the movie was played forwards for 10 seconds and backwards for 10 seconds for 50 repetitions. The white noise and natural movie were first shown under the dim condition, the OD2 filter was then removed, and both the stimuli were repeated after the animal was allowed to adapt to the mean 'bright' luminance for at least 10 minutes.

3.4.5 Electrophysiology

On the day of the recording, the KwikSil, if used, was removed and the brain was irrigated with saline. Unsharpened or sharpened Neuropixel 2.0 probes were slowly lowered vertically down into the craniotomy with a micromanipulator (Luigs and Neumann) while avoiding any visible blood vessels. After reaching the depth of about $800\mu m$, the speed of the probe was automated to $1\mu m/\text{sec}$ till the retrosplenial cortex was passed and the dorsal SC surface was found. Dim flashes of white noise were used as a probing stimulus to identify the visually responsive sSC along the probe length. The probe was lowered by a further 700 μ m after the start of the SC to a final depth of around 1800-2100 μ m from the brain surface.

Full bandwidth signals were recorded from 96 channels at the tip of each of the 4 shanks at 20kHz using the SpikeGLX software. The data was preprocessed by high-pass filtering above 400Hz and common median referencing (Rolston et al., 2009) using the SpikeInterface python package (Buccino et al., 2020). Sessions from all stimulus periods (excluding the dark/light adaptation) were concatenated and drift correction and spike sorting was then performed with KiloSort 3 (Pachitariu et al., 2023) on an Nvidia RTX 3060 GPU.

3.4.6 Receptive Field Analysis

Spatiotemporal receptive fields were computed and analysed as described previously (Gupta et al., 2023). In brief, the spike triggered average was computed with latencies at 60Hz upto

450ms before and 50ms after each spike (Rieke et al., 1999). For behaviorally conditioned RFs, lower and upper thresholds of pupil area were defined at the 33rd and 66th percentiles of the distribution. Only spikes at times when the pupil was below (/above) the lower (/upper) threshold were used for the rest (/active) RF. The minimum of the spike counts in both sets was found and the same number of spikes were randomly subsampled from the other set.

Each RF was normalized between -1 and 1 by subtracting the mean value of the pixels at the edges of the screen (outside of any RFs) and dividing by the maximum absolute value of the entire RF. The SNR of an RF was computed as the peak-to-noise ratio where the power of noise was again estimated in regions at the edges of the screen. A threshold SNR of 19dB was used to select visually responsive units. Only units that crossed this threshold in both brightness conditions were used for RF comparisons. RFs were computed for both green and UV channels but most UV RFs were of inadequate SNR and hence could not be used for reliable comparisons.

The location of the center of an RF was estimated by finding the pixel that varied the most across time. Each neuron's RF was cropped within a square window of edge 29° of visual angle centered on this pixel. The temporal RF was estimated as the mean of a 2x2 pixel window around the center pixel across time. The spatial RF was defined as the mean of 3 frames around the time when the variance across the spatial dimensions was the highest. To ensure comparable amplitudes, the center pixel and the snapshot time for the 'dim' vs 'bright' or 'rest' vs 'active' was allowed to be vary slightly but the cropping was always done around the same center pixel for each neuron.

3.4.7 **RF** Parametrization

A biphasic polynomial with an exponential decay was used to parameterize temporal RFs. The functional form was adapted from (Adel- All analysis and visualization code will be made son & Bergen, 1985) to allow a temporal shift. public on GitHub upon journal publication.

$$RF(t) = s \left(c_1 \frac{t'^5}{5!} - c_2 \frac{t'^7}{7!} \right) e^{-t'}$$
$$t' = \alpha(t - t_0)$$

where,

denotes OFF or ON $s \in \{-1, 1\}$ $c_1 > 0$ represents the 1st phase $c_2 > 0$ represents the 2nd phase $\alpha > 0$ stretches time $t_0 > 0$ shifts time

scipy.optimize.curve fit was used to perform the fitting to the bright RF. For the dim RF, all the parameters were then fixed to their bright values, except either α or t_0 that were then refitted to the dim RF.

3.4.8 Spike Rasters

Units were selected for the spike timing analysis if their receptive field SNRs were above threshold in at least one of the brightness conditions. The spike trains were assigned into individual trials and then binned at 5ms bins. The peri-stimulus time histograms were computed by averaging the firing rates across trials. The PSTHs were first normalized by dividing by their L^2 norm (numpy.linalg.norm) and then the cross-correlation between the dim and bright PSTHs was calculated using numpy.correlate. The xarray and pandas python packages were used for organizing and manipulating the data.

3.5 Data Availability

The spike-sorted electrophysiology data, labeled eye tracking data, and stimulus movies will be made available, preferably as Neurodata without border (NWB) files (Rübel et al., 2022), upon journal publication. .

Code Availability 3.6

CHAPTER 4

Discussion

In this thesis I have explored how spatial processing in the retina takes into account the fact that the sky is almost always brighter than the ground (Chapter 2), and how temporal processing in the Superior Colliculus (SC) speeds up when light levels allow it, or when the cognitive state of the animal demands it (Chapter 3). The center-surround receptive field structure of Retinal Ganglion Cell (RGC) somas (Fig. 2.3), and their terminals in the SC (Fig. 2.5), was found to change between the upper and lower visual fields, in order to efficiently account for differences in mean luminance encountered by these regions (Fig. 2.1). When the animal was exposed to different ambient luminance levels, individual neurons in the SC, however, barely changed the shape of their spatiotemporal filters (Fig. 3.2). Under more light or increased arousal (Fig. 3.3), neurons instead seem to code similar features, but faster.

The need for more

One common theme in the two projects is the advance in recording technologies that allow simultaneous measurements from an increasing number of neurons. The number of simultaneously recordable electrode sites in the brain, like Moore's law, has been doubling about every 7 years for more than five decades (Stevenson, 2013; Stevenson & Kording, 2011). For recordings in the SC, we used the Neuropixel arrays (Fig. 3.1), the current generation of devices to push this trend forwards, which are designed and distributed by a large consortium of neuroscience labs (Jun et al., 2017; Steinmetz et al., 2021). The high throughput of this technology allowed us to see subtle effects in population spike timing within single animals (Fig. 3.1). Although physical constraints like energy dissipation, intrinsic noise, and scattering do exist to limit the spatiotemporal resolution and range of different methods to different extents, neural recordings can realistically continue to scale at this pace at least for the coming century (Marblestone et al., 2013; Stevenson & Kording, 2011).

The retina-imaging system we developed continues this trajectory, by leveraging the use of red-shifted Calcium indicators to dramatically increase the recordable surface of the retina compared to previous 2-Photon retinal imaging systems (Fig. 2.2). Red shifted indicators represent the demand for calcium indicators that can be imaged from deeper depths of the brain with less scattering (Dana et al., 2016; Farrants et al., 2024; Shcherbakova, 2021; Shemetov et al., 2021), and somewhat coincidentally have the side-effect of not interfering with mammalian opsins (Euler et al., 2019). One can therefore predict that as more far-red and infrared calcium indicators become sufficiently bright and sensitive, 1-Photon imaging

systems will continue to push the limits of retinal imaging, eventually enabling recording responses from M or even L opsins (Cheong et al., 2018; Fyk-Kolodziej et al., 2014; Gupta et al., 2023). It would not have been possible to observe the localized specializations within individual retinas (Fig. 2.3), without the spatial extent offered by this method. The lower cost of this system with respect to 2-photon approaches can allow labs all over the world to study development of retinal wiring, carry out functional drug screenings, extend comparative studies to non-model organisms, and investigate fundamental topics in population retinal coding and their topographic variations. As a concrete example, macroscopic imaging of retinal waves can be extended from spontaneous stage 1 and 2 waves, to include light-evoked stage 3 waves, by switching from the green GCaMP to the red RCaMP or jRGECO1a indicators (Voufo et al., 2023). Another application is highlighted in Appendix A to show how functional properties of RGCs that project to specific retinorecipient targets can be investigated.

Mechanisms of receptive field adaptations across retinal space

The main finding from our retina work is that the center-surround structure of receptive fields is anisotropic across the retina. RGCs in the ventral retina have smaller RF centers and stronger surrounds, while the dorsal retina has larger RF centers and very little surround suppression (Fig. 2.3). A natural question to ask regarding this anisotropy of the mouse retina, is its mechanistic origin. The striking difference in S opsin expression at the photoreceptor level provides the first hint that the responses of downstream RGCs in the ventral and dorsal retina ought to be different (Nadal-Nicolás et al., 2020; Ortín-Martínez et al., 2014; Szél et al., 1992). RGC properties, like dendritic morphology (El-Danaf & Huberman, 2019), spectral tuning (Nadal-Nicolás et al., 2020; Szatko et al., 2020), contrast tuning (Baden et al., 2013) and temporal dynamics (Warwick et al., 2018) do indeed vary for several RGC types along the dorsoventral axis, and the strongest effect we observed, in the asymmetry of surrounds, was exactly at the opsin transition zone (Fig. 2.3). Tellingly, species of mice that live in forested or hedged areas, where the elevation gradient of luminance is likely obscured by vegetation, do not show a dorsoventral gradient of opsins (Szél et al., 1994).

A recent study shines light specifically on how surround strengths might vary from the dorsal to ventral retina. Spinelli et al. (2024) found that various aspects of horizontal cells, a putative source of surround inhibition to RGCs (Chaya et al., 2017; Mangel, 1991; Ströh et al., 2018), vary in key characteristics like density, morphology and electrical synapses along the dorsoventral axis. The dorsal retina has fewer horizontal cells, with larger arborizations and more expansive electrical coupling. This positions horizontal cells to provide weaker and more diffuse surround inhibition (Joesch & Meister, 2016) to dorsal RGCs as opposed to their ventral counterparts. Although the relative role of horizontal cells and amacrine cells in RGC surround inhibition is often debated (Cook & McReynolds, 1998; Drinnenberg et al., 2018; Franke et al., 2017), our results regarding topographic variation of surround inhibition across RGC types (Fig. 2.4), in light of these retina-wide horizontal cell anisotropies (Spinelli et al., 2024), point towards the role of inhibition from horizontal cells in globally modulating surround strengths across the dorsoventral axis in most, if not all, downstream RGCs.

Theoretical perspectives

The efficient coding theory provides a compelling framework for explaining how metabolic constraints dictate necessary adaptations to visual representations conveyed by the retina. When noise is low enough (i.e. under bright conditions), RGCs remove predictable information from the visual scene (Atick & Redlich, 1990; Barlow, 1961; Srinivasan et al., 1982), for

instance by subtracting 'surround'ing information from the center within their spatial RFs or by biphasic filtering in the temporal domain. When noise is higher (i.e. under darker conditions), surrounds get weaker and temporal filters get stretched and become less biphasic, leading to selectivity for lower spatiotemporal frequencies (Enroth-Cugell & Shapley, 1973; Ogawa et al., 1966; Ruda et al., 2022). Since light levels follow a gradient from the sky to the ground, we theorized and discovered that receptive fields of RGCs in different parts of the retina have different center-surround structures, in line with an efficient representation of panoramic natural scenes (Gupta et al., 2023).

Remarkably, however, just one synapse later in the SC, we found that given enough time for steady-state adaptation to luminance changes, the spatial or temporal features represented by individual SC neurons did not change significantly with light levels (Fig. 3.2). This begs the question of why the adaptations predicted by efficient coding are followed to different extents by these two visual structures?

Firstly, efficient codes do not prescribe how far down the visual hierarchy such adaptations should persist. It is possible that while RGCs have to contend with photoreceptor noise, in the form of a dark current, at low light levels, the adapted retinal code may offer a relatively 'denoised' input to the downstream areas, reducing the need for re-adapting at every visual relay. At the same time, the retina has to compress all visual information into ~50k axons of the optic nerve (Claes & Moons, 2022), whereas the brain has a lot more neuronal resources, with the V1 alone containing 10 times as many neurons (Herculano-Houzel et al., 2013). This suggests that efficient adaptations may hold more importance at the sensory periphery. Research in these downstream visual areas, like the V1, has also shown that representations of spatial and temporal tuning (Bisti et al., 1977; O'Shea et al., 2024) or orientation and direction selectivity (Bisti et al., 1977; Duffy & Hubel, 2007) are largely invariant to background luminance.

Furthermore, it is not clear how downstream areas may continue to interpret such altered codes from the sensory periphery, to infer behaviorally-relevant features under changing contexts (Machens et al., 2005; Młynarski & Hermundstad, 2018, 2021). As RGC temporal filters get stretched at low light levels, the spike timings of individual RGCs would become less reliable compared to the same stimulus under bright conditions. The coordinated shifts of population activity that we observed in the SC (Fig. 3.1) suggests one possible mechanism that downstream areas might employ to interpret the retina's dynamic output. Even when individual neurons alter their spike timings, a code that utilizes relative timing between neurons can continue to function under such changing contexts (Gollisch & Meister, 2008), provided that neurons in the population shift by the same amount, as observed in our SC experiments. In line with this perspective, noise correlations between pairs of RGCs have been found to increase under scotopic conditions (Ruda et al., 2020), possibly to compensate for decreased precision in the spike timing of individual RGCs.

Overall, it seems the adaptations necessary for efficient coding at the sensory periphery, need not be the same throughout the visual pathway, and a different set of resource and behavioral constraints instead prioritize invariant representations across luminance levels via population timing mechanisms. Our work thus provides exciting new directions for experimental validation of efficiency in retinorecipient areas, and a rethinking of the necessary constraints beyond the retina.

Ethological relevance of observed adaptations

Based on the functional differences we found at the level of the retinal output, one can hypothesize that there should be a difference in visual acuity between the upper and lower visual fields. Since RGCs in the upper visual field have smaller centers and stronger surrounds (Fig. 2.3), mice would have higher visual acuity overhead. A large fraction of RGCs in the ventral retina do indeed respond to small stimuli (Zhang et al., 2012). Mice face the threat of predation mainly from birds of prey, and the ability to resolve smaller stimuli in the upper visual field would be highly adaptive for survival (Heukamp et al., 2020; Yilmaz & Meister, 2013). Interestingly, a study of representation of visual space in the primate SC has shown that the upper visual field is afforded higher neural resolution (Hafed & Chen, 2016), presumably because objects in the upper visual field tend to be farther, and thus smaller. RF or spatial tuning maps of the mouse SC, like that of direction selectivity (Y.-t. Li et al., 2020), or direct behavioral assays of acuity would be needed to assess the downstream consequences of the center-surround differences in the upper and lower visual fields.

Our results in the SC show that representations of visual features, do not change significantly with changing luminance levels. Given the SC's role in detection of abrupt and salient changes to guide orienting responses (Basso & May, 2017; Krauzlis et al., 2013; F. Liang et al., 2015; Zhao et al., 2014; Zingg et al., 2017), such invariant encoding might be more important for the SC to reliably execute behavioral responses (Savier et al., 2019). In light of this, it is worthwhile to note that SC visual responses become faster when the animal is aroused (Fig. 3.3). This particular adaptation may be caused either by increased light from a wider pupil or by neuromodulation, and would facilitate faster threat detection by the SC at times of danger.

Concluding Remarks

The phenomenon of adaptation can arise with regards to different features of natural statistics, and can occur at different time scales, from evolutionary to sub-second. A comprehensive understanding of vision, therefore, will require compiling global and local adaptations across different nodes in the visual hierarchy, as they are modulated by diverse environmental and internal factors.

In this thesis, I have investigated visual adaptations from multiple angles. Retinal study utilized *ex-vivo* calcium imaging, while the SC recordings were *in-vivo* electrophysiology. In the retina, we found adaptations that were built into neurons at different anatomical location. In the SC, adaptations were to be found within the properties of individual cells under different contexts. The retina likely took millennia to adapt to the brightness gradient across elevation, while the SC adaptations unfold dynamically in minutes or possibly seconds. The retinal adaptations concern processing of spatial information, and the SC adaptations were only found in the temporal domain. The retina emphasizes metabolically efficient representations, which the SC then uses to form a stable code that can be timed appropriately for behavioral output. These findings thus encompass various facets of visual adaptation to offer a broader understanding of how the visual system as a whole may efficiently represent the environment, while being flexible enough to adjust to different internal and external contexts.

Bibliography

- Aarts, E., Verhage, M., Veenvliet, J. V., Dolan, C. V., & van der Sluis, S. (2014). A solution to dependency: Using multilevel analysis to accommodate nested data [Publisher: Nature Publishing Group]. Nature Neuroscience, 17(4), 491–496. https://doi.org/10.1038/nn. 3648
- Adelson, E. H., & Bergen, J. R. (1985). Spatiotemporal energy models for the perception of motion. *Journal of the Optical Society of America*. *A, Optics and Image Science*, 2(2), 284–299. https://doi.org/10.1364/josaa.2.000284
- Allen, M., Poggiali, D., Whitaker, K., Marshall, T., van Langen, J., & Kievit, R. (2021). Raincloud plots: A multi-platform tool for robust data visualization [version 2; peer review: 2 approved]. *Wellcome Open Research*, 4(63). https://doi.org/10.12688/wellcomeopenres.15191.2
- Atick, J. J. (2011). Could information theory provide an ecological theory of sensory processing? [Publisher: Taylor & Francis _eprint: https://doi.org/10.3109/0954898X.2011.638888]. Network: Computation in Neural Systems, 22(1-4), 4–44. https://doi.org/10.3109/0954898X.2011.638888
- Atick, J. J., & Redlich, A. N. (1990). Towards a theory of early visual processing [MAG ID: 2151351982]. Neural Computation, 2(3), 308-320. https://doi.org/10.1162/neco. 1990.2.3.308
- Atick, J. J., & Redlich, A. N. (1992). What Does the Retina Know about Natural Scenes? Neural Computation, 4(2), 196–210. https://doi.org/10.1162/neco.1992.4.2.196
- Baden, T., Berens, P., Franke, K., Rosón, M. R., Bethge, M., & Euler, T. (2016). The functional diversity of retinal ganglion cells in the mouse. *Nature*, *529*(7586), 345–350. https://doi.org/10.1038/nature16468
- Baden, T., Schubert, T., Chang, L., Wei, T., Zaichuk, M., Wissinger, B., & Euler, T. (2013). A Tale of Two Retinal Domains: Near-Optimal Sampling of Achromatic Contrasts in Natural Scenes through Asymmetric Photoreceptor Distribution. *Neuron*, *80*(5), 1206–1217. https://doi.org/10.1016/j.neuron.2013.09.030
- Balasubramanian, V., & Berry, M. J. (2002). A test of metabolically efficient coding in the retina. *Network*, 13(4), 531–552.
- Barbur, J. L. (1982). Reaction-time determination of the latency between visual signals generated by rods and cones. *Ophthalmic & Physiological Optics: The Journal of the British College of Ophthalmic Opticians (Optometrists)*, 2(3), 179–185.
- Barlow, H. (1961). Possible Principles Underlying the Transformations of Sensory Messages. Sensory Communication, 1. https://doi.org/10.7551/mitpress/9780262518420.003. 0013
- Barlow, H., Fitzhugh, R., & Kuffler, S. W. (1957). Change of organization in the receptive fields of the cat's retina during dark adaptation. *The Journal of Physiology*, 137(3), 338–354. https://doi.org/10.1113/jphysiol.1957.sp005817

- Bashivan, P., Kar, K., & DiCarlo, J. J. (2019). Neural population control via deep image synthesis. *Science*, *364*(6439). https://doi.org/10.1126/science.aav9436
- Basso, M. A., Bickford, M. E., & Cang, J. (2021). Unraveling circuits of visual perception and cognition through the superior colliculus. *Neuron*. https://doi.org/10.1016/j.neuron. 2021.01.013
- Basso, M. A., & May, P. J. (2017). Circuits for Action and Cognition: A View from the Superior Colliculus. *Annual Review of Vision Science*, *3*(1), 197–226. https://doi.org/10.1146/annurev-vision-102016-061234
- Baylor, D. A., & Hodgkin, A. L. (1974). Changes in time scale and sensitivity in turtle photoreceptors. *The Journal of Physiology*, 242(3), 729–758. https://doi.org/10.1113/jphysiol.1974.sp010732
- Berson, D. M. (2008, January). 1.25 Retinal Ganglion Cell Types and Their Central Projections. In R. H. Masland, T. D. Albright, T. D. Albright, R. H. Masland, P. Dallos, D. Oertel, S. Firestein, G. K. Beauchamp, M. Catherine Bushnell, A. I. Basbaum, J. H. Kaas, & E. P. Gardner (Eds.), *The Senses: A Comprehensive Reference* (pp. 491–519). Academic Press. https://doi.org/10.1016/B978-012370880-9.00280-2
- Birman, D., Yang, K. J., West, S. J., Karsh, B., Browning, Y., Laboratory, t. I. B., Siegle, J. H., & Steinmetz, N. A. (2023). Pinpoint: Trajectory planning for multi-probe electrophysiology and injections in an interactive web-based 3D environment [Publisher: eLife Sciences Publications Limited]. *eLife*, *12*. https://doi.org/10.7554/eLife.91662.1
- Bisti, S., Clement, R., Maffei, L., & Mecacci, L. (1977). Spatial frequency and orientation tuning curves of visual neurones in the cat: Effects of mean luminance. *Experimental Brain Research*, 27(3-4), 335–345. https://doi.org/10.1007/BF00235508
- Buccino, A. P., Hurwitz, C. L., Garcia, S., Magland, J., Siegle, J. H., Hurwitz, R., & Hennig, M. H. (2020). SpikeInterface, a unified framework for spike sorting (L. L. Colgin, S. Grün, & F. Kloosterman, Eds.) [Publisher: eLife Sciences Publications, Ltd]. *eLife*, *9*, e61834. https://doi.org/10.7554/eLife.61834
- Chalk, M., Marre, O., & Tkačik, G. (2018). Toward a unified theory of efficient, predictive, and sparse coding. *Proceedings of the National Academy of Sciences*, 115(1), 186–191. https://doi.org/10.1073/pnas.1711114115
- Chapot, C. A., Euler, T., & Schubert, T. (2017). How do horizontal cells 'talk' to cone photoreceptors? Different levels of complexity at the cone-horizontal cell synapse. *The Journal of Physiology*, *595*(16), 5495–5506. https://doi.org/10.1113/JP274177
- Chaya, T., Matsumoto, A., Sugita, Y., Watanabe, S., Kuwahara, R., Tachibana, M., & Furukawa, T. (2017). Versatile functional roles of horizontal cells in the retinal circuit [Publisher: Nature Publishing Group]. *Scientific Reports*, 7(1), 5540. https://doi.org/10.1038/s41598-017-05543-2
- Cheong, S. K., Xiong, W., Strazzeri, J. M., Cepko, C. L., Williams, D. R., & Merigan, W. H. (2018). In Vivo Functional Imaging of Retinal Neurons Using Red and Green Fluorescent Calcium Indicators. In J. D. Ash, R. E. Anderson, M. M. LaVail, C. Bowes Rickman, J. G. Hollyfield, & C. Grimm (Eds.), *Retinal Degenerative Diseases* (pp. 135–144). Springer International Publishing. https://doi.org/10.1007/978-3-319-75402-4_17
- Chichilnisky, E. J. (2001). A simple white noise analysis of neuronal light responses. *Network*, 12(2), 199–213.
- Claes, M., & Moons, L. (2022). Retinal Ganglion Cells: Global Number, Density and Vulnerability to Glaucomatous Injury in Common Laboratory Mice. *Cells*, *11*(17), 2689. https://doi.org/10.3390/cells11172689

- Clemens, J., Ozeri-Engelhard, N., & Murthy, M. (2018). Fast intensity adaptation enhances the encoding of sound in Drosophila [Publisher: Nature Publishing Group]. *Nature Communications*, 9(1), 134. https://doi.org/10.1038/s41467-017-02453-9
- Cook, P. B., & McReynolds, J. S. (1998). Lateral inhibition in the inner retina is important for spatial tuning of ganglion cells [Publisher: Nature Publishing Group]. *Nature Neuroscience*, 1(8), 714–719. https://doi.org/10.1038/3714
- Dana, H., Mohar, B., Sun, Y., Narayan, S., Gordus, A., Hasseman, J. P., Tsegaye, G., Holt, G. T., Hu, A., Walpita, D., Patel, R., Macklin, J. J., Bargmann, C. I., Ahrens, M. B., Schreiter, E. R., Jayaraman, V., Looger, L. L., Svoboda, K., & Kim, D. S. (2016). Sensitive red protein calcium indicators for imaging neural activity (M. Häusser, Ed.) [Publisher: eLife Sciences Publications, Ltd]. eLife, 5, e12727. https://doi.org/10.7554/eLife.12727
- de Ruyter van Steveninck, R., & Bialek, W. (1988). Real-time performance of a movement-sensitive neuron in the blowfly visual system: Coding and information transfer in short spike sequences [Publisher: Royal Society]. *Proceedings of the Royal Society of London. Series B. Biological Sciences*, 234(1277), 379–414. https://doi.org/10.1098/rspb.1988. 0055
- Demb, J. B., & Singer, J. H. (2012). Intrinsic properties and functional circuitry of the AII amacrine cell. *Visual Neuroscience*, 29(1), 51–60. https://doi.org/10.1017/S0952523811000368
- Denk, W., & Detwiler, P. B. (1999). Optical recording of light-evoked calcium signals in the functionally intact retina. *Proceedings of the National Academy of Sciences of the United States of America*, 96(12), 7035–7040. Retrieved September 16, 2024, from https://www.ncbi.nlm.nih.gov/pmc/articles/PMC22046/
- Doi, E., & Lewicki, M. (2006). A Theory of Retinal Population Coding. In B. Schölkopf, J. Platt, & T. Hoffman (Eds.), Advances in Neural Information Processing Systems (Vol. 19). MIT Press. https://proceedings.neurips.cc/paper_files/paper/2006/file/bbb001ba009ed11717eaec9305b2feb6-Paper.pdf
- Doykos, T. K., Gilmer, J. I., Person, A. L., & Felsen, G. (2020). Monosynaptic inputs to specific cell types of the intermediate and deep layers of the superior colliculus. *Journal of Comparative Neurology*, n/a(n/a). https://doi.org/10.1002/cne.24888
- Drinnenberg, A., Franke, F., Morikawa, R. K., Jüttner, J., Hillier, D., Hantz, P., Hierlemann, A., Silveira, R. A. d., & Roska, B. (2018). How Diverse Retinal Functions Arise from Feedback at the First Visual Synapse [Publisher: Elsevier]. *Neuron*, 99(1), 117–134.e11. https://doi.org/10.1016/j.neuron.2018.06.001
- Duffy, K. R., & Hubel, D. H. (2007). Receptive field properties of neurons in the primary visual cortex under photopic and scotopic lighting conditions. *Vision Research*, 47(19), 2569–2574. https://doi.org/10.1016/j.visres.2007.06.009
- El-Danaf, R. N., & Huberman, A. D. (2019). Sub-topographic maps for regionally enhanced analysis of visual space in the mouse retina. *Journal of Comparative Neurology*, *527*(1), 259–269. https://doi.org/10.1002/cne.24457
- Ellis, E. M., Gauvain, G., Sivyer, B., & Murphy, G. J. (2016). Shared and distinct retinal input to the mouse superior colliculus and dorsal lateral geniculate nucleus. *Journal of Neurophysiology*, 116(2), 602–610. https://doi.org/10.1152/jn.00227.2016
- Enroth-Cugell, C., & Shapley, R. M. (1973). Adaptation and dynamics of cat retinal ganglion cells. *The Journal of Physiology*, 233(2), 271–309. Retrieved May 9, 2024, from https://www.ncbi.nlm.nih.gov/pmc/articles/PMC1350567/
- Erisken, S., Vaiceliunaite, A., Jurjut, O., Fiorini, M., Katzner, S., & Busse, L. (2014). Effects of Locomotion Extend throughout the Mouse Early Visual System [Publisher: Elsevier]. *Current Biology*, 24(24), 2899–2907. https://doi.org/10.1016/j.cub.2014.10.045

- Euler, T., Detwiler, P. B., & Denk, W. (2002). Directionally selective calcium signals in dendrites of starburst amacrine cells [Publisher: Nature Publishing Group]. *Nature*, 418(6900), 845–852. https://doi.org/10.1038/nature00931
- Euler, T., Franke, K., & Baden, T. (2019, March). Studying a Light Sensor with Light: Multiphoton Imaging in the Retina (preprint). LIFE SCIENCES. https://doi.org/10.20944/preprints201903.0244.v1
- Famiglietti, E. V., & Kolb, H. (1976). Structural Basis for ON-and OFF-Center Responses in Retinal Ganglion Cells [Publisher: American Association for the Advancement of Science]. *Science*, 194(4261), 193–195. https://doi.org/10.1126/science.959847
- Farrants, H., Shuai, Y., Lemon, W. C., Monroy Hernandez, C., Zhang, D., Yang, S., Patel, R., Qiao, G., Frei, M. S., Plutkis, S. E., Grimm, J. B., Hanson, T. L., Tomaska, F., Turner, G. C., Stringer, C., Keller, P. J., Beyene, A. G., Chen, Y., Liang, Y., ... Schreiter, E. R. (2024). A modular chemigenetic calcium indicator for multiplexed in vivo functional imaging [Publisher: Nature Publishing Group]. *Nature Methods*, *21*(10), 1916–1925. https://doi.org/10.1038/s41592-024-02411-6
- Franke, K., Berens, P., Schubert, T., Bethge, M., Euler, T., & Baden, T. (2017). Inhibition decorrelates visual feature representations in the inner retina [Publisher: Nature Publishing Group]. *Nature*, *542*(7642), 439–444. https://doi.org/10.1038/nature21394
- Franke, K., Willeke, K. F., Ponder, K., Galdamez, M., Zhou, N., Muhammad, T., Patel, S., Froudarakis, E., Reimer, J., Sinz, F. H., & Tolias, A. S. (2022). State-dependent pupil dilation rapidly shifts visual feature selectivity [Number: 7930 Publisher: Nature Publishing Group]. *Nature*, 610(7930), 128–134. https://doi.org/10.1038/s41586-022-05270-3
- Fried, S. I., Münch, T. A., & Werblin, F. S. (2002). Mechanisms and circuitry underlying directional selectivity in the retina [Publisher: Nature Publishing Group]. *Nature*, 420(6914), 411–414. https://doi.org/10.1038/nature01179
- Fu, Y. (n.d.). Phototransduction in Rods and Cones Webvision. Retrieved September 12, 2024, from https://webvision.med.utah.edu/book/part-v-phototransduction-in-rods-and-cones/phototransduction-in-rods-and-cones/
- Fukushima, K. (1980). Neocognitron: A self-organizing neural network model for a mechanism of pattern recognition unaffected by shift in position. *Biological Cybernetics*, *36*(4), 193–202. https://doi.org/10.1007/BF00344251
- Fyk-Kolodziej, B., Hellmer, C. B., & Ichinose, T. (2014). Marking Cells with Infrared Fluorescent Proteins to Preserve Photoresponsiveness in the Retina. *BioTechniques*, *57*(5), 245–253. https://doi.org/10.2144/000114228
- Gale, S. D., & Murphy, G. J. (2014). Distinct Representation and Distribution of Visual Information by Specific Cell Types in Mouse Superficial Superior Colliculus. *Journal of Neuroscience*, *34*(40), 13458–13471. https://doi.org/10.1523/JNEUROSCI.2768-14.2014
- Gjorgjieva, J., Sompolinsky, H., & Meister, M. (2014). Benefits of Pathway Splitting in Sensory Coding [Publisher: Society for Neuroscience Section: Articles]. *Journal of Neuroscience*, 34(36), 12127–12144. https://doi.org/10.1523/JNEUROSCI.1032-14.2014
- Goetz, J., Jessen, Z. F., Jacobi, A., Mani, A., Cooler, S., Greer, D., Kadri, S., Segal, J., Shekhar, K., Sanes, J. R., & Schwartz, G. W. (2022). Unified classification of mouse retinal ganglion cells using function, morphology, and gene expression. *Cell Reports*, 40(2), 111040. https://doi.org/10.1016/j.celrep.2022.111040
- Goldin, M. A., Lefebvre, B., Virgili, S., Pham Van Cang, M. K., Ecker, A., Mora, T., Ferrari, U., & Marre, O. (2022). Context-dependent selectivity to natural images in the retina

- [Number: 1 Publisher: Nature Publishing Group]. *Nature Communications*, 13(1), 5556. https://doi.org/10.1038/s41467-022-33242-8
- Gollisch, T., & Meister, M. (2008). Rapid Neural Coding in the Retina with Relative Spike Latencies. *Science*, 319(5866), 1108–1111. https://doi.org/10.1126/science.1149639
- Govardovskii, V. I., Fyhrquist, N., Reuter, T., Kuzmin, D. G., & Donner, K. (2000). In search of the visual pigment template. *Visual Neuroscience*, *17*(4), 509–528. https://doi.org/10.1017/s0952523800174036
- Groblewski, P. A., Ollerenshaw, D. R., Kiggins, J. T., Garrett, M. E., Mochizuki, C., Casal, L., Cross, S., Mace, K., Swapp, J., Manavi, S., Williams, D., Mihalas, S., & Olsen, S. R. (2020). Characterization of Learning, Motivation, and Visual Perception in Five Transgenic Mouse Lines Expressing GCaMP in Distinct Cell Populations. *Frontiers in Behavioral Neuroscience*, 14, 104. https://doi.org/10.3389/fnbeh.2020.00104
- Gupta, D., Młynarski, W., Sumser, A., Symonova, O., Svatoň, J., & Joesch, M. (2023). Panoramic visual statistics shape retina-wide organization of receptive fields [Number: 4 Publisher: Nature Publishing Group]. *Nature Neuroscience*, *26*(4), 606–614. https://doi.org/10.1038/s41593-023-01280-0
- Hafed, Z. M., & Chen, C.-Y. (2016). Sharper, Stronger, Faster Upper Visual Field Representation in Primate Superior Colliculus. *Current Biology*, 26(13), 1647–1658. https://doi.org/10.1016/j.cub.2016.04.059
- Hafed, Z. M., Hoffmann, K.-P., Chen, C.-Y., & Bogadhi, A. R. (2023). Visual Functions of the Primate Superior Colliculus.
- Hartline, H. K. (1938). The response of single optic nerve fibers of the vertebrate eye to illumination of the retina [Publisher: American Physiological Society]. *American Journal of Physiology*, 121(2), 400–415. https://doi.org/10.1152/ajplegacy.1938.121.2.400
- Herculano-Houzel, S., Watson, C. R., & Paxinos, G. (2013). Distribution of neurons in functional areas of the mouse cerebral cortex reveals quantitatively different cortical zones [Publisher: Frontiers]. *Frontiers in Neuroanatomy*, 7. https://doi.org/10.3389/fnana.2013.00035
- Heukamp, A. S., Warwick, R. A., & Rivlin-Etzion, M. (2020). Topographic Variations in Retinal Encoding of Visual Space. *Annual Review of Vision Science*, 6(1), 237–259. https://doi.org/10.1146/annurev-vision-121219-081831
- Hofbauer, A., & Dräger, U. C. (1985). Depth segregation of retinal ganglion cells projecting to mouse superior colliculus. *Journal of Comparative Neurology*, *234*(4), 465–474. https://doi.org/10.1002/cne.902340405
- Hosoya, T., Baccus, S. A., & Meister, M. (2005). Dynamic predictive coding by the retina [Bandiera_abtest: a Cg_type: Nature Research Journals Number: 7047 Primary_atype: Research Publisher: Nature Publishing Group]. *Nature*, 436(7047), 71–77. https://doi.org/10.1038/nature03689
- Hubel, D. H., & Wiesel, T. N. (1959). Receptive fields of single neurones in the cat's striate cortex. *The Journal of Physiology*, *148*(3), 574–591. Retrieved September 11, 2024, from https://www.ncbi.nlm.nih.gov/pmc/articles/PMC1363130/
- Huberman, A. D., Wei, W., Elstrott, J., Stafford, B. K., Feller, M. B., & Barres, B. A. (2009). Genetic Identification of an On-Off Direction- Selective Retinal Ganglion Cell Subtype Reveals a Layer-Specific Subcortical Map of Posterior Motion. *Neuron*, *62*(3), 327–334. https://doi.org/10.1016/j.neuron.2009.04.014
- Isa, T., Marquez-Legorreta, E., Grillner, S., & Scott, E. K. (2021). The tectum/superior colliculus as the vertebrate solution for spatial sensory integration and action [Publisher: Elsevier]. *Current Biology*, 31(11), R741–R762. https://doi.org/10.1016/j.cub.2021. 04.001

- Ito, S., Feldheim, D. A., & Litke, A. M. (2017). Segregation of Visual Response Properties in the Mouse Superior Colliculus and Their Modulation during Locomotion. *Journal of Neuroscience*, 37(35), 8428–8443. https://doi.org/10.1523/JNEUROSCI.3689-16.2017
- Joesch, M., & Meister, M. (2016). A neuronal circuit for colour vision based on rod–cone opponency [Number: 7598 Publisher: Nature Publishing Group]. *Nature*, *532*(7598), 236–239. https://doi.org/10.1038/nature17158
- Joshi, S., Li, Y., Kalwani, R. M., & Gold, J. I. (2016). Relationships between Pupil Diameter and Neuronal Activity in the Locus Coeruleus, Colliculi, and Cingulate Cortex. *Neuron*, 89(1), 221–234. https://doi.org/10.1016/j.neuron.2015.11.028
- Jun, J., Steinmetz, N. A., Siegle, J. H., Denman, D. J., Bauza, M., Barbarits, B., Lee, A. K., Anastassiou, C. A., Andrei, A., Aydın, Ç., Barbic, M., Blanche, T. J., Bonin, V., Couto, J., Dutta, B., Gratiy, S. L., Gutnisky, D. A., Häusser, M., Karsh, B., ... Harris, T. D. (2017). Fully integrated silicon probes for high-density recording of neural activity [Publisher: Nature Publishing Group]. *Nature*, 551(7679), 232–236. https://doi.org/10.1038/nature24636
- Kay, J., de la Huerta, I., Kim, I.-J., Zhang, Y., Yamagata, M., Chu, M., Meister, M., & Sanes, J. (2011). Retinal ganglion cells with distinct directional preferences differ in molecular identity, structure, and central projections. *Journal of Neuroscience*, 31(21), 7753–7762. https://doi.org/10.1523/JNEUROSCI.0907-11.2011
- Kerschensteiner, D., & Feller, M. B. (2024). Mapping the Retina onto the Brain [Company: Cold Spring Harbor Laboratory Press Distributor: Cold Spring Harbor Laboratory Press Institution: Cold Spring Harbor Laboratory Press Label: Cold Spring Harbor Laboratory Press Publisher: Cold Spring Harbor Lab]. *Cold Spring Harbor Perspectives in Biology*, 16(2), a041512. https://doi.org/10.1101/cshperspect.a041512
- Kim, I.-J., Zhang, Y., Meister, M., & Sanes, J. R. (2010). Laminar Restriction of Retinal Ganglion Cell Dendrites and Axons: Subtype-Specific Developmental Patterns Revealed with Transgenic Markers. *Journal of Neuroscience*, 30(4), 1452–1462. https://doi.org/10.1523/JNEUROSCI.4779-09.2010
- Kim, I.-J., Zhang, Y., Yamagata, M., Meister, M., & Sanes, J. R. (2008). Molecular identification of a retinal cell type that responds to upward motion. *Nature*, 452(7186), 478–482. https://doi.org/10.1038/nature06739
- Krauzlis, R. J., Lovejoy, L. P., & Zénon, A. (2013). Superior Colliculus and Visual Spatial Attention. *Annual Review of Neuroscience*, *36*(1), 165–182. https://doi.org/10.1146/annurev-neuro-062012-170249
- Laughlin, S. (1981). A Simple Coding Procedure Enhances a Neuron's Information Capacity [Publisher: De Gruyter]. *Zeitschrift für Naturforschung C*, 36(9-10), 910–912. https://doi.org/10.1515/znc-1981-9-1040
- Lettvin, J., Maturana, H., McCulloch, W., & Pitts, W. (1959). What the Frog's Eye Tells the Frog's Brain. *Proceedings of the IRE*, 47(11), 1940–1951. https://doi.org/10.1109/JRPROC.1959.287207
- Lewicki, M. S. (2002). Efficient coding of natural sounds. *Nature Neuroscience*, *5*(4), 356–363. https://doi.org/10.1038/nn831
- Li, Y.-t., & Meister, M. (2023). Functional cell types in the mouse superior colliculus (F. Rieke, C. Desplan, & F. Rieke, Eds.) [Publisher: eLife Sciences Publications, Ltd]. *eLife*, 12, e82367. https://doi.org/10.7554/eLife.82367
- Li, Y.-t., Turan, Z., & Meister, M. (2020). Functional Architecture of Motion Direction in the Mouse Superior Colliculus. Current Biology, 30(17), 3304–3315.e4. https://doi.org/10.1016/j.cub.2020.06.023

- Li, Z., Peng, B., Huang, J. J., Zhang, Y., Seo, M. B., Fang, Q., Zhang, G.-W., Zhang, X., Zhang, L. I., & Tao, H. W. (2023). Enhancement and contextual modulation of visuospatial processing by thalamocollicular projections from ventral lateral geniculate nucleus | Nature Communications. *Nature Communications*, 14(1), 7278. https://doi.org/10.1038/s41467-023-43147-9
- Liang, F., Xiong, X. R., Zingg, B., Ji, X.-y., Zhang, L. I., & Tao, H. W. (2015). Sensory Cortical Control of a Visually Induced Arrest Behavior via Corticotectal Projections. *Neuron*, 86(3), 755–767. https://doi.org/10.1016/j.neuron.2015.03.048
- Liang, L., Fratzl, A., Goldey, G., Ramesh, R. N., Sugden, A. U., Morgan, J. L., Chen, C., & Andermann, M. L. (2018). A Fine-Scale Functional Logic to Convergence from Retina to Thalamus. *Cell*, 173(6), 1343–1355.e24. https://doi.org/10.1016/j.cell.2018.04.041
- Machens, C. K., Gollisch, T., Kolesnikova, O., & Herz, A. V. M. (2005). Testing the Efficiency of Sensory Coding with Optimal Stimulus Ensembles. *Neuron*, 47(3), 447–456. https://doi.org/10.1016/j.neuron.2005.06.015
- Malmazet, D. d., Kühn, N. K., Li, C., & Farrow, K. (2024). Retinal origin of orientation but not direction selective maps in the superior colliculus [Publisher: Elsevier]. *Current Biology*, 34(6), 1222–1233.e7. https://doi.org/10.1016/j.cub.2024.02.001
- Mangel, S. C. (1991). Analysis of the horizontal cell contribution to the receptive field surround of ganglion cells in the rabbit retina. *The Journal of Physiology*, 442(1), 211–234. https://doi.org/10.1113/jphysiol.1991.sp018790
- Maravall, M., Petersen, R. S., Fairhall, A. L., Arabzadeh, E., & Diamond, M. E. (2007). Shifts in Coding Properties and Maintenance of Information Transmission during Adaptation in Barrel Cortex [Publisher: Public Library of Science]. *PLOS Biology*, *5*(2), e19. https://doi.org/10.1371/journal.pbio.0050019
- Marblestone, A. H., Zamft, B. M., Maguire, Y. G., Shapiro, M. G., Cybulski, T. R., Glaser, J. I., Amodei, D., Stranges, P. B., Kalhor, R., Dalrymple, D. A., Seo, D., Alon, E., Maharbiz, M. M., Carmena, J. M., Rabaey, J. M., Boyden**, E. S., Church**, G. M., & Kording**, K. P. (2013). Physical principles for scalable neural recording [Publisher: Frontiers]. Frontiers in Computational Neuroscience, 7. https://doi.org/10.3389/fncom.2013.00137
- Martersteck, E. M., Hirokawa, K. E., Evarts, M., Bernard, A., Duan, X., Li, Y., Ng, L., Oh, S. W., Ouellette, B., Royall, J. J., Stoecklin, M., Wang, Q., Zeng, H., Sanes, J. R., & Harris, J. A. (2017). Diverse Central Projection Patterns of Retinal Ganglion Cells. Cell Reports, 18(8), 2058–2072. https://doi.org/10.1016/j.celrep.2017.01.075
- Masland, R. H. (2012). The neuronal organization of the retina. *Neuron*, 76(2), 266-280. https://doi.org/10.1016/j.neuron.2012.10.002
- Mathis, A., Mamidanna, P., Cury, K. M., Abe, T., Murthy, V. N., Mathis, M. W., & Bethge, M. (2018). DeepLabCut: Markerless pose estimation of user-defined body parts with deep learning. *Nature Neuroscience*, *21*(9), 1281–1289. https://doi.org/10.1038/s41593-018-0209-y
- May, P. J. (2006, January). The mammalian superior colliculus: Laminar structure and connections. In J. A. Büttner-Ennever (Ed.), *Progress in Brain Research* (pp. 321–378, Vol. 151). Elsevier. https://doi.org/10.1016/S0079-6123(05)51011-2
- McIntosh, L., Maheswaranathan, N., Nayebi, A., Ganguli, S., & Baccus, S. (2016). Deep Learning Models of the Retinal Response to Natural Scenes. *Advances in Neural Information Processing Systems*, *29.* Retrieved September 11, 2024, from https://proceedings.neurips.cc/paper/2016/hash/a1d33d0dfec820b41b54430b50e96b5c-Abstract.html

- Meister, M., Pine, J., & Baylor, D. A. (1994). Multi-neuronal signals from the retina: Acquisition and analysis. *Journal of Neuroscience Methods*, 51(1), 95–106. https://doi.org/10.1016/0165-0270(94)90030-2
- Młynarski, W., & Hermundstad, A. M. (2018). Adaptive coding for dynamic sensory inference (S. Palmer, Ed.) [Publisher: eLife Sciences Publications, Ltd]. *eLife*, 7, e32055. https://doi.org/10.7554/eLife.32055
- Młynarski, W., & Hermundstad, A. M. (2021). Efficient and adaptive sensory codes | Nature Neuroscience. *Nature Neuroscience*, 24(7), 998–1009. https://doi.org/10.1038/s41593-021-00846-0
- Młynarski, W., Hledík, M., Sokolowski, T. R., & Tkačik, G. (2021). Statistical analysis and optimality of neural systems. *Neuron*. https://doi.org/10.1016/j.neuron.2021.01.020
- Mumford, D. (1992). On the computational architecture of the neocortex. *Biological Cybernetics*, 66(3), 241–251. https://doi.org/10.1007/BF00198477
- Nadal-Nicolás, F. M., Kunze, V. P., Ball, J. M., Peng, B. T., Krishnan, A., Zhou, G., Dong, L., & Li, W. (2020). True S-cones are concentrated in the ventral mouse retina and wired for color detection in the upper visual field (F. Rieke, B. G. Shinn-Cunningham, F. Rieke, T. Baden, & R. Sinha, Eds.) [Publisher: eLife Sciences Publications, Ltd]. eLife, 9, e56840. https://doi.org/10.7554/eLife.56840
- Niell, C. M., & Stryker, M. P. (2010). Modulation of visual responses by behavioral state in mouse visual cortex. *Neuron*, 65(4), 472-479. https://doi.org/10.1016/j.neuron.2010.01.033
- Ogawa, T., Bishop, P. O., & Levick, W. R. (1966). Temporal characteristics of responses to photic stimulation by single ganglion cells in the unopened eye of the cat. [Publisher: American Physiological Society]. *Journal of Neurophysiology*, 29(1), 1–30. https://doi.org/10.1152/jn.1966.29.1.1
- Olshausen, B. A., & Field, D. J. (1996). Emergence of simple-cell receptive field properties by learning a sparse code for natural images [Publisher: Nature Publishing Group]. *Nature*, 381(6583), 607–609. https://doi.org/10.1038/381607a0
- Ortín-Martínez, A., Nadal-Nicolás, F. M., Jiménez-López, M., Alburquerque-Béjar, J. J., Nieto-López, L., García-Ayuso, D., Villegas-Pérez, M. P., Vidal-Sanz, M., & Agudo-Barriuso, M. (2014). Number and Distribution of Mouse Retinal Cone Photoreceptors: Differences between an Albino (Swiss) and a Pigmented (C57/BL6) Strain [Publisher: Public Library of Science]. *PLOS ONE*, *9*(7), e102392. https://doi.org/10.1371/journal.pone.0102392
- O'Shea, R., Nauhaus, I., Wei, X.-X., & Priebe, N. J. (2024, April). Luminance invariant encoding in primary visual cortex. https://doi.org/10.1101/2024.04.18.590073
- Pachitariu, M., Sridhar, S., & Stringer, C. (2023, January). *Solving the spike sorting problem with Kilosort* (preprint). Neuroscience. https://doi.org/10.1101/2023.01.07.523036
- Pachitariu, M., Stringer, C., Dipoppa, M., Schröder, S., Rossi, L. F., Dalgleish, H., Carandini, M., & Harris, K. D. (2017). Suite2p: Beyond 10,000 neurons with standard two-photon microscopy. *bioRxiv*, 061507. https://doi.org/10.1101/061507
- Petersen, R. S., Panzeri, S., & Diamond, M. E. (2001). Population Coding of Stimulus Location in Rat Somatosensory Cortex. *Neuron*, 32(3), 503-514. https://doi.org/10.1016/S0896-6273(01)00481-0
- Pitkow, X., & Meister, M. (2012). Decorrelation and efficient coding by retinal ganglion cells. *Nature Neuroscience*, 15(4), 628–635. https://doi.org/10.1038/nn.3064
- Rajan, K., Marre, O., & Tkačik, G. (2013). Learning Quadratic Receptive Fields from Neural Responses to Natural Stimuli. *Neural Computation*, *25*(7), 1661–1692. https://doi.org/10.1162/NECO_a_00463

- Ramoa, A. S., Freeman, R. D., & Macy, A. (1985). Comparison of response properties of cells in the cat's visual cortex at high and low luminance levels [Publisher: American Physiological Society]. *Journal of Neurophysiology*, *54*(1), 61–72. https://doi.org/10. 1152/jn.1985.54.1.61
- Rao, R. P. N., & Ballard, D. H. (1999). Predictive coding in the visual cortex: A functional interpretation of some extra-classical receptive-field effects. *Nature Neuroscience*, 2(1), 79–87. https://doi.org/10.1038/4580
- Reimer, J., Froudarakis, E., Cadwell, C. R., Yatsenko, D., Denfield, G. H., & Tolias, A. S. (2014). Pupil Fluctuations Track Fast Switching of Cortical States during Quiet Wakefulness. *Neuron*, *84*(2), 355–362. https://doi.org/10.1016/j.neuron.2014.09.033
- Reinhard, K., Li, C., Do, Q., Burke, E. G., Heynderickx, S., & Farrow, K. (2019). A projection specific logic to sampling visual inputs in mouse superior colliculus. *eLife*, 8, e50697. https://doi.org/10.7554/eLife.50697
- Rieke, F., Warland, D., Steveninck, R. D. R. V., & Bialek, W. (1999, June). *Spikes: Exploring the Neural Code* (Reprint edition). Bradford Books.
- Rolfe, D. F., & Brown, G. C. (1997). Cellular energy utilization and molecular origin of standard metabolic rate in mammals. *Physiological Reviews*, 77(3), 731–758. https://doi.org/10.1152/physrev.1997.77.3.731
- Rolston, J. D., Gross, R. E., & Potter, S. M. (2009). Common median referencing for improved action potential detection with multielectrode arrays [ISSN: 1558-4615]. 2009 Annual International Conference of the IEEE Engineering in Medicine and Biology Society, 1604–1607. https://doi.org/10.1109/IEMBS.2009.5333230
- Rübel, O., Tritt, A., Ly, R., Dichter, B. K., Ghosh, S., Niu, L., Baker, P., Soltesz, I., Ng, L., Svoboda, K., Frank, L., & Bouchard, K. E. (2022). The Neurodata Without Borders ecosystem for neurophysiological data science (L. L. Colgin & S. P. Jadhav, Eds.) [Publisher: eLife Sciences Publications, Ltd]. *eLife*, *11*, e78362. https://doi.org/10.7554/eLife.78362
- Ruda, K., Rudzite, A. M., & Field, G. D. (2022, September). The functional organization of retinal ganglion cell receptive fields across light levels [Pages: 2022.09.15.508164 Section: New Results]. https://doi.org/10.1101/2022.09.15.508164
- Ruda, K., Zylberberg, J., & Field, G. D. (2020). Ignoring correlated activity causes a failure of retinal population codes | Nature Communications. *Nature Communications*, 11(1), 4605. https://doi.org/10.1038/s41467-020-18436-2
- Saleem, A. B., & Busse, L. (2023). Interactions between rodent visual and spatial systems during navigation [Publisher: Nature Publishing Group]. *Nature Reviews Neuroscience*, 24(8), 487–501. https://doi.org/10.1038/s41583-023-00716-7
- Sanes, J. R., & Masland, R. H. (2015). The Types of Retinal Ganglion Cells: Current Status and Implications for Neuronal Classification. *Annual Review of Neuroscience*, 38(1), 221–246. https://doi.org/10.1146/annurev-neuro-071714-034120
- Savier, E. L., Chen, H., & Cang, J. (2019). Effects of Locomotion on Visual Responses in the Mouse Superior Colliculus. *The Journal of Neuroscience*, *39*(47), 9360–9368. https://doi.org/10.1523/JNEUROSCI.1854-19.2019
- Schneeweis, D. M., & Schnapf, J. L. (1995). Photovoltage of Rods and Cones in the Macaque Retina. *Science, New Series*, 268(5213), 1053–1056. http://www.jstor.org/stable/2888883
- Schröder, S., Steinmetz, N. A., Krumin, M., Pachitariu, M., Rizzi, M., Lagnado, L., Harris, K. D., & Carandini, M. (2020). Arousal Modulates Retinal Output. *Neuron*, 107(3), 487–495.e9. https://doi.org/10.1016/j.neuron.2020.04.026

- Seabrook, T. A., Burbridge, T. J., Crair, M. C., & Huberman, A. D. (2017). Architecture, Function, and Assembly of the Mouse Visual System. *Annual Review of Neuroscience*, 40, 499–538. https://doi.org/10.1146/annurev-neuro-071714-033842
- Shannon, C. E. (1948). A mathematical theory of communication [Conference Name: The Bell System Technical Journal]. *The Bell System Technical Journal*, 27(3), 379–423. https://doi.org/10.1002/j.1538-7305.1948.tb01338.x
- Sharpee, T. O. (2013). Computational Identification of Receptive Fields. *Annual Review of Neuroscience*, 36(1), 103–120. https://doi.org/10.1146/annurev-neuro-062012-170253
- Sharpee, T. O., Sugihara, H., Kurgansky, A. V., Rebrik, S. P., Stryker, M. P., & Miller, K. D. (2006). Adaptive filtering enhances information transmission in visual cortex [Number: 7079 Publisher: Nature Publishing Group]. *Nature*, 439(7079), 936–942. https://doi.org/10.1038/nature04519
- Shcherbakova, D. M. (2021). Near-infrared and far-red genetically encoded indicators of neuronal activity. *Journal of Neuroscience Methods*, *362*, 109314. https://doi.org/10.1016/j.jneumeth.2021.109314
- Shekhar, K., Lapan, S. W., Whitney, I. E., Tran, N. M., Macosko, E. Z., Kowalczyk, M., Adiconis, X., Levin, J. Z., Nemesh, J., Goldman, M., McCarroll, S. A., Cepko, C. L., Regev, A., & Sanes, J. R. (2016). Comprehensive Classification of Retinal Bipolar Neurons by Single-Cell Transcriptomics [Publisher: Elsevier]. *Cell*, *166*(5), 1308–1323.e30. https://doi.org/10.1016/j.cell.2016.07.054
- Shelley, J., Dedek, K., Schubert, T., Feigenspan, A., Schultz, K., Hombach, S., Willecke, K., & Weiler, R. (2006). Horizontal cell receptive fields are reduced in connexin57-deficient mice. *European Journal of Neuroscience*, 23(12), 3176–3186. https://doi.org/10.1111/j.1460-9568.2006.04848.x
- Shemetov, A. A., Monakhov, M. V., Zhang, Q., Canton-Josh, J. E., Kumar, M., Chen, M., Matlashov, M. E., Li, X., Yang, W., Nie, L., Shcherbakova, D. M., Kozorovitskiy, Y., Yao, J., Ji, N., & Verkhusha, V. V. (2021). A near-infrared genetically encoded calcium indicator for in vivo imaging [Publisher: Nature Publishing Group]. *Nature Biotechnology*, 39(3), 368–377. https://doi.org/10.1038/s41587-020-0710-1
- Shi, X., Barchini, J., Ledesma, H. A., Koren, D., Jin, Y., Liu, X., Wei, W., & Cang, J. (2017). Retinal origin of direction selectivity in the superior colliculus. *Nature Neuroscience*, 20(4), 550–558. https://doi.org/10.1038/nn.4498
- Sibille, J., Gehr, C., Benichov, J. I., Balasubramanian, H., Teh, K. L., Lupashina, T., Vallentin, D., & Kremkow, J. (2022). High-density electrode recordings reveal strong and specific connections between retinal ganglion cells and midbrain neurons [Publisher: Nature Publishing Group]. *Nature Communications*, 13(1), 5218. https://doi.org/10.1038/s41467-022-32775-2
- Spinelli, M., H, A. A., Block, C. T., Lindenthal, L., Schuhmann, F., Greschner, M., Janssen-Bienhold, U., Dedek, K., & Puller, C. (2024, June). The first interneuron of the mouse visual system is tailored to the natural environment through morphology and electrical coupling [Pages: 2024.06.12.598640 Section: New Results]. https://doi.org/10.1101/2024.06.12.598640
- Spitschan, M., Aguirre, G. K., Brainard, D. H., & Sweeney, A. M. (2016). Variation of outdoor illumination as a function of solar elevation and light pollution [Publisher: Nature Publishing Group]. *Scientific Reports*, 6(1), 26756. https://doi.org/10.1038/srep26756
- Srinivasan, M. V., Laughlin, S. B., Dubs, A., & Horridge, G. A. (1982). Predictive coding: A fresh view of inhibition in the retina [Publisher: Royal Society]. *Proceedings of the Royal Society of London. Series B. Biological Sciences*, 216(1205), 427–459. https://doi.org/10.1098/rspb.1982.0085

- Steinmetz, N. A., Aydin, C., Lebedeva, A., Okun, M., Pachitariu, M., Bauza, M., Beau, M., Bhagat, J., Böhm, C., Broux, M., Chen, S., Colonell, J., Gardner, R. J., Karsh, B., Kloosterman, F., Kostadinov, D., Mora-Lopez, C., O'Callaghan, J., Park, J., . . . Harris, T. D. (2021). Neuropixels 2.0: A miniaturized high-density probe for stable, long-term brain recordings [Publisher: American Association for the Advancement of Science]. *Science*, 372(6539), eabf4588. https://doi.org/10.1126/science.abf4588
- Stevenson, I. (2013, October). Tracking Advances in Neural Recording | Statistical Neuroscience Lab. Retrieved October 14, 2024, from https://stevenson.lab.uconn.edu/scaling/
- Stevenson, I., & Kording, K. (2011). How advances in neural recording affect data analysis [Publisher: Nature Publishing Group]. *Nature Neuroscience*, *14*(2), 139–142. https://doi.org/10.1038/nn.2731
- Ströh, S., Puller, C., Swirski, S., Hölzel, M.-B., Linde, L. I. S. v. d., Segelken, J., Schultz, K., Block, C., Monyer, H., Willecke, K., Weiler, R., Greschner, M., Janssen-Bienhold, U., & Dedek, K. (2018). Eliminating Glutamatergic Input onto Horizontal Cells Changes the Dynamic Range and Receptive Field Organization of Mouse Retinal Ganglion Cells [Publisher: Society for Neuroscience Section: Research Articles]. *Journal of Neuroscience*, 38(8), 2015–2028. https://doi.org/10.1523/JNEUROSCI.0141-17.2018
- Sumser, A., Joesch, M., Jonas, P., & Ben-Simon, Y. (2022). Fast, high-throughput production of improved rabies viral vectors for specific, efficient and versatile transsynaptic retrograde labeling (R. Seal, L. L. Colgin, & I. Wickersham, Eds.) [Publisher: eLife Sciences Publications, Ltd]. *eLife*, 11, e79848. https://doi.org/10.7554/eLife.79848
- Szatko, K. P., Korympidou, M. M., Ran, Y., Berens, P., Dalkara, D., Schubert, T., Euler, T., & Franke, K. (2020). Neural circuits in the mouse retina support color vision in the upper visual field [Number: 1 Publisher: Nature Publishing Group]. *Nature Communications*, 11(1), 3481. https://doi.org/10.1038/s41467-020-17113-8
- Szél, Á., Csorba, G., Caffé, A. R., Szél, G., Röhlich, P., & van Veen, T. (1994). Different patterns of retinal cone topography in two genera of rodents, Mus and Apodemus. *Cell and Tissue Research*, *276*(1), 143–150. https://doi.org/10.1007/BF00354793
- Szél, Á., Röhlich, P., Gaffé, A. R., Juliusson, B., Aguirre, G., & Van Veen, T. (1992). Unique topographic separation of two spectral classes of cones in the mouse retina. *Journal of Comparative Neurology*, 325(3), 327–342. https://doi.org/10.1002/cne.903250302
- Tikidji-Hamburyan, A., Reinhard, K., Seitter, H., Hovhannisyan, A., Procyk, C. A., Allen, A. E., Schenk, M., Lucas, R. J., & Münch, T. A. (2015). Retinal output changes qualitatively with every change in ambient illuminance. *Nature Neuroscience*, *18*(1), 66–74. https://doi.org/10.1038/nn.3891
- Tripodi, M., & Asari, H. (2024, September). Histamine interferes with the early visual processing in mice [Pages: 2024.09.02.610848 Section: New Results]. https://doi.org/10.1101/2024.09.02.610848
- Vaney, D. I., Sivyer, B., & Taylor, W. R. (2012). Direction selectivity in the retina: Symmetry and asymmetry in structure and function [Number: 3 Publisher: Nature Publishing Group]. *Nature Reviews Neuroscience*, 13(3), 194–208. https://doi.org/10.1038/nrn3165
- VanLeeuwen, M., Fahrenfort, I., Sjoerdsma, T., Numan, R., & Kamermans, M. (2009). Lateral Gain Control in the Outer Retina Leads to Potentiation of Center Responses of Retinal Neurons. *The Journal of Neuroscience*, 29(19), 6358. https://doi.org/10.1523/JNEUROSCI.5834-08.2009
- Vega-Zuniga, T., Sumser, A., Symonova, O., Koppensteiner, P., Schmidt, F. H., & Joesch, M. (2024, July). A thalamic hub-and-spoke circuit enables visual perception during action by coordinating visuomotor dynamics [Pages: 2023.12.23.573221 Section: New Results]. https://doi.org/10.1101/2023.12.23.573221

- Vinck, M., Batista-Brito, R., Knoblich, U., & Cardin, J. A. (2015). Arousal and Locomotion Make Distinct Contributions to Cortical Activity Patterns and Visual Encoding. *Neuron*, 86(3), 740–754. https://doi.org/10.1016/j.neuron.2015.03.028
- Voufo, C., Chen, A. Q., Smith, B. E., Yan, R., Feller, M. B., & Tiriac, A. (2023). Circuit mechanisms underlying embryonic retinal waves (F. Rieke, M. E. Bronner, F. Rieke, & G. López-Bendito, Eds.) [Publisher: eLife Sciences Publications, Ltd]. eLife, 12, e81983. https://doi.org/10.7554/eLife.81983
- Walker, E. Y., Sinz, F. H., Cobos, E., Muhammad, T., Froudarakis, E., Fahey, P. G., Ecker, A. S., Reimer, J., Pitkow, X., & Tolias, A. S. (2019). Inception loops discover what excites neurons most using deep predictive models. *Nature Neuroscience*, *22*(12), 2060–2065. https://doi.org/10.1038/s41593-019-0517-x
- Warwick, R. A., Kaushansky, N., Sarid, N., Golan, A., & Rivlin-Etzion, M. (2018). Inhomogeneous Encoding of the Visual Field in the Mouse Retina. *Current Biology*, 28(5), 655–665.e3. https://doi.org/10.1016/j.cub.2018.01.016
- Wässle, H., Peichl, L., & Boycott, B. B. (1981). Dendritic territories of cat retinal ganglion cells [Publisher: Nature Publishing Group]. *Nature*, *292*(5821), 344–345. https://doi.org/10.1038/292344a0
- Wässle, H. (2004). Parallel processing in the mammalian retina [Publisher: Nature Publishing Group]. *Nature Reviews Neuroscience*, 5(10), 747–757. https://doi.org/10.1038/nrn1497
- Weber, A. I., Krishnamurthy, K., & Fairhall, A. L. (2019). Coding Principles in Adaptation. Annual Review of Vision Science, 5(1), 427–449. https://doi.org/10.1146/annurevvision-091718-014818
- Wienbar, S., & Schwartz, G. W. (2018). The dynamic receptive fields of retinal ganglion cells. *Progress in Retinal and Eye Research*, *67*, 102–117. https://doi.org/10.1016/j. preteyeres.2018.06.003
- Williamson, R. S., Sahani, M., & Pillow, J. W. (2015). The Equivalence of Information—Theoretic and Likelihood-Based Methods for Neural Dimensionality Reduction. *PLOS Computational Biology*, 11(4), e1004141. https://doi.org/10.1371/journal.pcbi. 1004141
- Yan, W., Laboulaye, M. A., Tran, N. M., Whitney, I. E., Benhar, I., & Sanes, J. R. (2020). Mouse Retinal Cell Atlas: Molecular Identification of over Sixty Amacrine Cell Types. *The Journal of Neuroscience*, 40(27), 5177–5195. https://doi.org/10.1523/JNEUROSCI. 0471-20.2020
- Yilmaz, M., & Meister, M. (2013). Rapid Innate Defensive Responses of Mice to Looming Visual Stimuli. *Current Biology*, 23(20), 2011–2015. https://doi.org/10.1016/j.cub. 2013.08.015
- Yu, Z., Guindani, M., Grieco, S. F., Chen, L., Holmes, T. C., & Xu, X. (2022). Beyond t test and ANOVA: Applications of mixed-effects models for more rigorous statistical analysis in neuroscience research. *Neuron*, *110*(1), 21–35. https://doi.org/10.1016/j.neuron. 2021.10.030
- Zele, A. J., Cao, D., & Pokorny, J. (2008). Rod-cone interactions and the temporal impulse response of the cone pathway. *Vision research*, 48(26), 2593–2598. https://doi.org/10.1016/j.visres.2008.04.003
- Zhang, Y., Kim, I.-J., Sanes, J. R., & Meister, M. (2012). The most numerous ganglion cell type of the mouse retina is a selective feature detector. *Proceedings of the National Academy of Sciences*, 109(36), E2391–E2398. https://doi.org/10.1073/pnas.1211547109

- Zhao, X., Liu, M., & Cang, J. (2014). Visual Cortex Modulates the Magnitude but Not the Selectivity of Looming-Evoked Responses in the Superior Colliculus of Awake Mice. *Neuron*, 84(1), 202–213. https://doi.org/10.1016/j.neuron.2014.08.037
- Zingg, B., Chou, X.-I., Zhang, Z.-g., Mesik, L., Liang, F., Tao, H. W., & Zhang, L. I. (2017). AAV-Mediated Anterograde Transsynaptic Tagging: Mapping Corticocollicular Input-Defined Neural Pathways for Defense Behaviors. *Neuron*, *93*(1), 33–47. https://doi.org/10.1016/j.neuron.2016.11.045

Functional imaging of RGCs projecting to genetically defined targets

The retina projects to ~40 different retiorecipient regions in the brain and each region can receive inputs from different combinations of RGC types (Berson, 2008; Kay et al., 2011; Kerschensteiner & Feller, 2024; L. Liang et al., 2018; Martersteck et al., 2017; Reinhard et al., 2019). One common approach to study the functional properties of the projecting RGCs, is with patch electrophysiology. A retrograde virus carrying a fluorescent protein is injected in the retinorecipient region, and only the fluorescently labelled RGCs are patched (Reinhard et al., 2019). Although this method can be combined with morphological analysis of these RGCs, the functional properties of only a handful of projecting RGCs can be studied per retina.

Our retinal imaging system (Gupta et al., 2023), in combination with a rabies labelling approach (Sumser et al., 2022) can vastly increase the throughput of investigating functional properties of RGC projections, while allowing precise genetically defined targeting of retinorecipient areas. In this approach, an AAV starter virus carrying TVA (AAV-DIO-EF1a-TVA-P2A-N2cG) is first injected in the brain region of interest of a cre reporter mouse line. For example, widefield neurons of the SC can be targeted with NTSR1-cre mouse line (Gale & Murphy, 2014), or the inhibitory neuron of vLGN can be targeted with the Gad2-cre line (Vega-Zuniga et al., 2024). Because of the DIO formulation, TVA will only be expressed in the cre+ cells. Next, a rabies virus, carrying a red calcium indicator (RVdG_{envA}-N2c-jRGECO1a) is injected in the same region. The rabies then jumps pre-synaptically from the TVA+ neurons, carrying the calcium indicator to the RGCs.

Once the rabies has expressed, the retina can be harvested and imaged, as described in chapter 2. Fig A.1 shows results from two such proof-of-concept recordings from RGCs that project to the vLGN or the SC. In these early experiments, 20-40 RGCs could be easily detected with suite2p (Pachitariu et al., 2017) in each recording (Fig. A.1A,C), and likely many more could be detected with imaging and analysis optimizations. Looking at responses to the chirp stimulus (Baden et al., 2016) of a few neurons, it can be seen that vLGN projecting RGCs tend have relatively similar responses (Fig. A.1B), while widefield neurons in the SC receive inputs from a wide variety of RGC subtypes (Fig. A.1D).

The cre dependence of the starter virus allows genetic targeting of specific sub-populations within a larger region, for example widefield neurons within the SC, or precise targeting of smaller brain nuclei, for example, the vLGN. These pilot experiments show that this technique can

greatly simplify the functional study of RGC projections to specific retino-recipient populations, allowing high throughput investigation of how different retinal output channels influence visual processing by different nodes in the visual system.

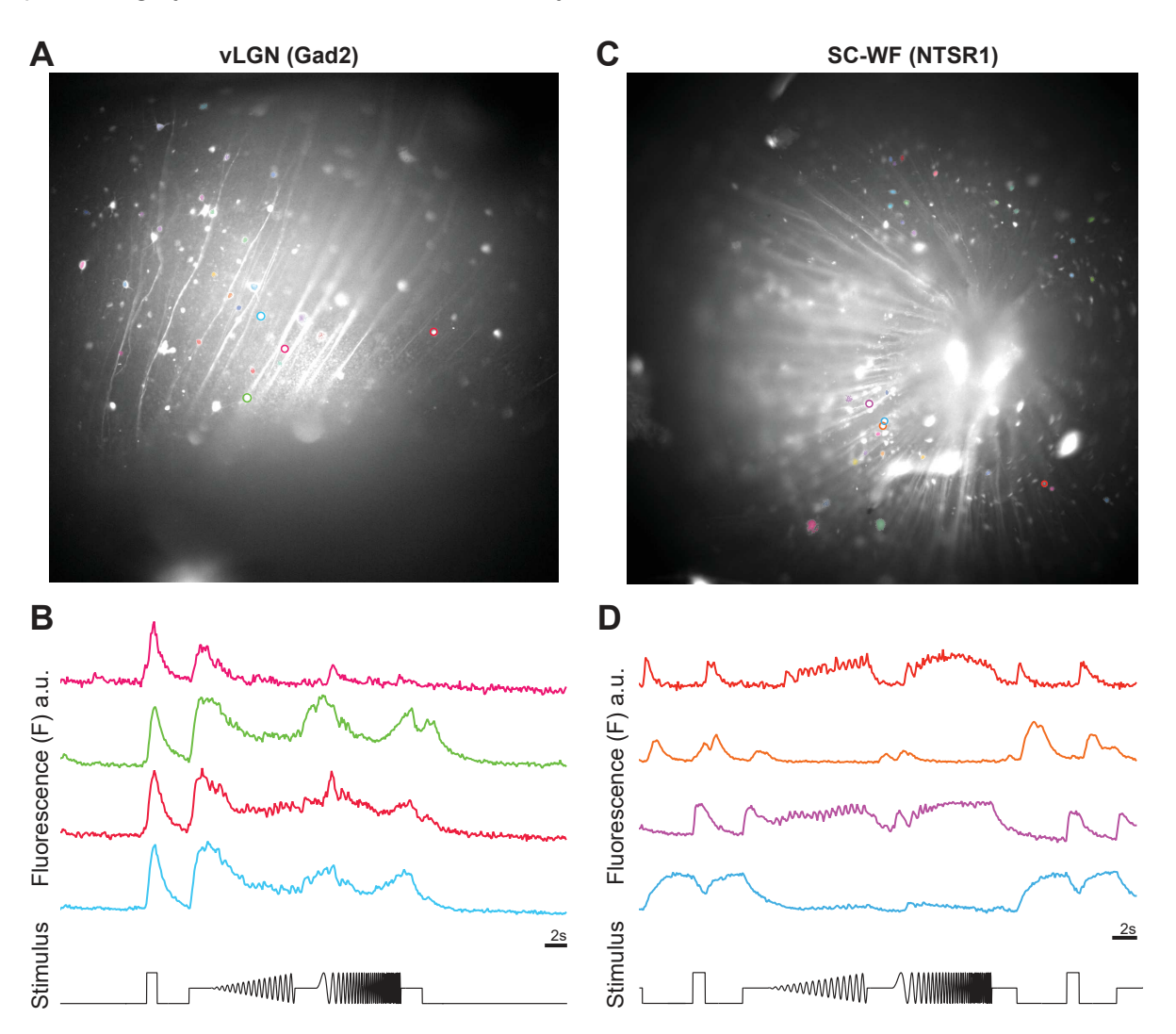


Figure A.1: RGCs projecting to vLGN and widefield nuerons in SC. (A) Maximum projection across time of jRGECO1a-positive RGCs that project to Gad2-positive neurons in the vLGN. All detected ROIs have colored masks and cells presented in B are marked with open circles. (B) Fluorescence traces of four example RGCs from (A). Bottom: Intensity of the chirp stimulus across time. (C) Same as (A), but for jRGECO1a-positive RGCs that project to NTSR1-positive widefield (WF) neurons in the SC. (D) Same as (B), but for example RGCs in (C)

Acknowledgements

We thank Yoav Ben-Simon for developing and providing the rabies viruses used in these experiments, and Tomas Vega-Zuniga for stereotactic injections in the vLGN.